UNIVERSIDADE ESTADUAL DE CAMPINAS
Faculdade de Engenharia Elétrica e de Computação

Johann Eduardo Baader

A Novel Technique for Detecting Radiation Damage in Variable-Gap Permanent-Magnet Undulators Based on *In-Situ* Magnetic Measurements

Uma Nova Técnica para Detecção de Danos por Radiação em Onduladores de Magnetos Permanentes de Abertura Variável Baseada em Medições Magnéticas Locais

Campinas
2019

Johann Eduardo Baader

A Novel Technique for Detecting Radiation Damage in Variable-Gap Permanent-Magnet Undulators Based on *In-Situ* Magnetic Measurements

Uma Nova Técnica para Detecção de Danos por Radiação em Onduladores de Magnetos Permanentes de Abertura Variável Baseada em Medições Magnéticas Locais

Thesis presented to the School of Electrical and Computer Engineering of the University of Campinas in partial fulfillment of the requirements for the degree of Doctor in Electrical Engineering, in the area of Electrical Energy.

Tese apresentada à Faculdade de Engenharia Elétrica e de Computação da Universidade Estadual de Campinas como parte dos requisitos exigidos para a obtenção do título de Doutor em Engenharia Elétrica, na Área de Energia Elétrica.

Orientador (Tutor): Prof. José Antenor Pomilio

Este exemplar corresponde à versão final da tese defendida pelo aluno Johann Eduardo Baader, e orientada pelo Prof. José Antenor Pomilio.

Campinas
2019

Ficha catalográfica
Universidade Estadual de Campinas
Biblioteca da Área de Engenharia e Arquitetura
Luciana Pietrosanto Milla - CRB 8/8129

Baader, Johann Eduardo, 1988-
B11n A novel technique for detecting radiation damage in variable-gap permanent-magnet undulators based on *in-situ* magnetic measurements / Johann Eduardo Baader. – Campinas, SP : [s.n.], 2019.

Orientador: José Antenor Pomilio.
Tese (doutorado) – Universidade Estadual de Campinas, Faculdade de Engenharia Elétrica e de Computação.

1. Campos magnéticos. 2. Medições magnéticas. 3. Imãs permanentes. 4. Efeitos de radiação. 5. Processamento digital de sinais. I. Pomilio, José Antenor, 1960-. II. Universidade Estadual de Campinas. Faculdade de Engenharia Elétrica e de Computação. III. Título.

Informações para Biblioteca Digital

Título em outro idioma: Uma nova técnica para detecção de danos por radiação em onduladores de magnetos permanentes de abertura variável baseada em medições magnéticas locais
Palavras-chave em inglês:
Magnetic fields
Magnetic measurements
Permanent magnets
Radiation effects
Digital signal processing
Área de concentração: Energia Elétrica
Titulação: Doutor em Engenharia Elétrica
Banca examinadora:
José Antenor Pomilio [Orientador]
Lucas Heitzmann Gabrielli
Fabiano Fruett
Giancarlo Tosin
Frederik Wolff-Fabris
Data de defesa: 16-12-2019
Programa de Pós-Graduação: Engenharia Elétrica

Identificação e informações acadêmicas do(a) aluno(a)
- ORCID do autor: https://orcid.org/0000-0001-5952-3920
- Currículo Lattes do autor: http://lattes.cnpq.br/8443835128690799

COMISSÃO JULGADORA - TESE DE DOUTORADO

Candidato: Johann Eduardo Baader RA: 144557

Data de defensa: 16 de dezembro de 2019

Título da Tese: "A Novel Technique for Detecting Radiation Damage in Variable-Gap Permanent-Magnet Undulators Based on *In-Situ* Magnetic Measurements"
(Uma Nova Técnica para Detecção de Danos por Radiação em Onduladores de Magnetos Permanentes de Abertura Variável Baseada em Medições Magnéticas Locais)

Prof. Dr. Prof. José Antenor Pomilio (Presidente, FEEC/UNICAMP)

Prof. Dr. Lucas Heitzmann Gabrielli (FEEC/UNICAMP)

Prof. Dr. Fabiano Fruett (FEEC/UNICAMP)

Dr. Giancarlo Tosin (Laboratório de Magnetismo Aplicado - LMA)

Dr. Frederik Wolff-Fabris (European XFEL GmbH)

A Ata de Defesa, com as respectivas assinaturas dos membros da Comissão Julgadora, encontra-se no SIGA (Sistema de Fluxo de Dissertação/Tese) e na Secretaria de Pós-Graduação da Faculdade de Engenharia Elétrica e de Computação.

To my parents Eliete Baader and Adilson Baader, and to Maury V. T. Navia.

Acknowledgement

First and foremost, I would like to show my highest appreciation to my advisor abroad, Zachary Wolf (Zack). I feel incredibly privileged to have had the chance to be his Ph.D. student. Besides being one of the most distinguished minds in our field, Zack has always been supportive, kind, and caring.

The members of the SLAC Magnetic Measurements Group contributed immensely to my personal and professional time. The group became a source of friendships, as well as useful guidance and collaboration. Special thanks to Scott Anderson, for all the knowledgeable discussions, the technical support, and the regular invitations to watch volleyball games at Stanford. Yurii Levachov gave insightful comments and suggestions on the flip coil system, and I am enormously thankful to him too. I would like to express my gratitude to Robert Pushor (Bob), who gave me generous support on coding in C language, and, after a while, became a strong opponent in our daily battles "wins who leaves the lab later". I owe a significant debt to the Metrology Department head, Georg Gassner. He always did everything that he could to assist me and to make myself "at home" during my visiting program, including interviews at SLAC and financial support. I want to thank Luiz Juarez, for patiently teaching me how to solder boards and tiny cables under high-quality standards and for all the technical assistance with the flip coil system. Enthusiastic in so many ways, he never had problems to convince myself to play some sports at SLAC even when I did not feel like it.

I express my gratitude to my advisor at Unicamp, Prof. José Antenor Pomilio. Since we started working together, he has been extraordinarily supportive, tolerant, and insightful. Antenor was the person who primarily encouraged me to embrace the challenge of studying abroad. Also, many thanks to his former student, Fernando Rafael, who made the first contact

with SLAC's people. I owe a very substantial debt to Giancarlo Tosin, who introduced me to the magnetic measurements world in 2012. Gian inspired me in so many ways, and I would not have reached this stage in my career without him.

I appreciate the feedback offered by Tonee Smith, João Nilton Henrique da Rosa, and Egidio Schroeder, who patiently provided remarkable suggestions regarding the development of the verification circuit. Thanks to Scott Jansson, Ralph Colon, and Ed Reese for all the technical support. I also want to thank Heinz-Dieter Nuhn for all the constructive comments regarding my work.

My time in the USA was made enjoyable in large part due to the many friends that became a part of my life. Special thanks to my great friend Krishna Agrawal for being so present in my life since we started having English classes back in 2015. At that time, I had never imagined that the future would make me his guest in Las Vegas for over a week. I also wish to thank my roommates and friends, Ryota Kiuchi and Dilip Bhogadi, for the "whiskey with talk and music" nights, the exceptional hikes, and the trips in California. I have immensely appreciated the camaraderie of Edward Loizeaux, Marcio Donadio, Maria Claudia Peroto, Esther Wehr, Cynthia Wehr, and Raphael Fernando Moral.

I have been extremely lucky to be surrounded by many great friends. I want to thank (in no particular order), Raul Palacios-Trujillo, Susana Fargas, Jorge Fernandez, Sheila Katherine Venero Ferro, Maria Teresa Cardenas Galvis, Marleny Charagua Javier, Edelson Constantino, Felipe Pires, Felipe Dias, Luiz Carlos Pinheiro Junior, Santiago Villa, and Lorena León, for all the enjoyable and funny moments.

Thanks to the committee members of this thesis' defense, Dr. Frederik Wolff-Fabris, Prof. Lucas Heitzmann Gabrielli, Prof. Fabiano Fruett, and Dr. Giancarlo Tosin, who kindly accepted our invitation to read, review, and appraise this work.

I would like to express my gratefulness to my family, in special to my parents Eliete Baader, Adilson Baader, for all their love and encouragement. Lastly, I owe my gratitude to my lovely Maury V. T. Navia, for everything she has done for me since we met. Words will never express my thankfulness to you.

This study was financed in part by the Coordenação de Aperfeiçoamento de Pessoal de Nível Superior - Brasil (CAPES) - Finance Code 001, by the U.S. Department of Energy

under contract number DE-AC02-76SF00515 in support of the LCLS-II project at SLAC National Accelerator Laboratory, by FAEPEX/UNICAMP grant numbers 519.292/94550-19, and by National Council for Scientific and Technological Development (CNPq) grant numbers 140989/2015-3.

Equipped with his five senses man explores the universe around him and calls the adventure Science.

—Edwin Powell Hubble

Our confused wish finds expression in the confused question as to the nature of force and electricity. But the answer which we want is not really an answer to this question. It is not by finding out more and fresh relations and connections that it can be answered; but by removing the contradictions existing between those already known, and thus perhaps by reducing their number. When these painful contradictions are removed, the question as to the nature of force will not have been answered; but our minds, no longer vexed, will cease to ask illegitimate questions.

—Heinrich Rudolf Hertz

We are always and everywhere in the presence of reality. Indeed, the human mind is the most complex and subtle expression of reality we have thus far encountered. This should grant profundity to the humble project of noticing what it is like to be you in the present. However numerous your faults, something in you at this moment is pristine —and only you can recognize it. Open your eyes and see.

—Sam Harris

Abstract

Since the 1970s, storage rings (SR) and free-electron lasers (FEL) facilities use complex magnetic structures named *undulators* as a source of intense electromagnetic radiation. Such devices produce high brightness beams of photons by bending high-energy electrons back and forth through alternating polarity magnetic fields. Most of the undulator systems currently installed in SR and FEL facilities worldwide are permanent magnet-based. The demagnetization of permanent magnet materials due to radiation exposure causes loss of field strength, which disturbs the undulator's performance. In some cases, it is necessary to remove the undulator from the facility for inspection and repair it in a magnetic measurement laboratory, which is costly and time-consuming. Also, the dense pack of components near the undulator makes it challenging to set stages to move probes around for magnetic measurements as a specialized laboratory does. Techniques based upon measuring the photon beam characteristics have been used to evaluate undulators' magnetic field quality without removing them from the undulator hall. Although promising, the precision of these techniques is limited to the uncertainties of electron beam energy and observation angle. Besides, full access to the control and data acquisition systems is required. This thesis presents the proposal, the development, and the first tests of a new technique for diagnosing radiation damage based on *in situ* magnetic measurements. The proposed system measures the magnetic flux change in a flexible printed-circuit coil attached to the lower undulator magnet array by periodically opening and closing of the undulator gap and by measuring the induced voltage. The magnetic flux change

will decrease proportionally to the magnet block damage, assuming that the gap always changes by the same amount. The tests were performed on variable-gap permanent-magnet hybrid undulators for the new Linear Coherent Light Source (LCLS-II). The system proved to be capable of detecting local pole field changes on the order of 3 mT. Long-term uninterrupted measurements performed during eight days showed an error of approximately 70 ppm relative to a signal of a few tenths of Volt-second. To test the voltmeter, we developed a high-precision verification circuit capable of generating a reference voltage pulse with voltage-time integral stability better than 50 ppm relative to the reference integrated signal strength of the flexible coil. The circuit's design combines a fast and precise switch with a low-noise voltage reference. Reproducibility tests confirmed that the circuit's output is invariable under small power supply instabilities and equipment shutdown. Although preliminary, the results are encouraging: The novel radiation damage detection system lays the groundwork for future development into magnetic measurements-based sensors dedicated to monitoring undulators' field quality without removing the segments from the tunnel. Additionally, instruments and applications designed to quantify the magnetic field by integrating induced voltage signals may use the same proposed verification system for testing purposes.

Keywords: Demagnetization, electrical measurements, free electron lasers, magnetic field measurements, permanent magnets, pulse generation, pulse measurements, radiation damage, digital signal processing, storage rings, undulators.

Resumo

Desde os anos 70, aceleradores de partículas do tipo “anel de armazenamento” e “laser de elétrons livres” utilizam complexos arranjos magnéticos denominados *onduladores* como fonte de intensa radiação eletromagnética. Tais dispositivos criam um campo magnético com polaridades alternadas, forçando feixes de elétrons relativísticos a ondular e produzir fótons de alto brilho. Os sistemas de onduladores atualmente em operação são, em sua maioria, feitos com magnetos permanentes. A desmagnetização de magnetos permanentes devido à exposição à radiação causa redução do campo magnético, o que afeta o desempenho do ondulador. Em alguns casos, é necessário remover o ondulador da instalação para inspeção e reparos em um laboratório de medições magnéticas, o que é caro e consome tempo. Além disso, a alta densidade de equipamentos nas proximidades dos onduladores em operação torna difícil a instalação de estágios para movimentar sensores de medição de campo magnético da mesma forma que um laboratório dedicado o faz. Técnicas baseadas na medição das características do feixe de fótons têm sido aplicadas para avaliar a qualidade do campo magnético de onduladores sem removê-los das instalações. Apesar de promissora, a precisão dessas técnicas é limitada às incertezas de energia dos elétrons e ângulo de observação. Ademais, é necessário o acesso irrestrito aos sistemas de controle e aquisição de dados. Esta tese apresenta a proposta, o desenvolvimento e os primeiros testes de uma nova técnica de detecção de danos por radiação baseada em medições locais de campo magnético. Através da variação da abertura do ondulador, o sistema proposto mede a variação de fluxo magnético através da tensão induzida

em uma bobina flexível de circuito impresso posicionada sobre o conjunto inferior de magnetos. A redução do fluxo magnético será proporcional aos danos provocados nos magnetos, assumindo que a abertura do ondulador sempre varia de forma constante. Os testes foram realizados em um ondulador de magnetos permanentes híbrido de abertura variável que será utilizado no novo *Linear Coherent Light Source* (LCLS-II). O sistema detecta mudanças no campo de polos individuais na ordem de 3 mT. Medições ininterruptas realizadas durante oito dias demonstraram um erro relativo de aproximadamente 70 ppm para um sinal de alguns décimos de Volt-segundos. Para testar os voltímetros utilizados para medir variação de fluxo magnético, foi desenvolvido um circuito de verificação de alta precisão que gera pulsos com estabilidade melhor do que 50 ppm relativos à amplitude do sinal integrado de referência medido com a bobina. O circuito combina elementos de comutação rápida e precisa com tensões de referência de baixo ruído. Testes de reprodutibilidade confirmaram que o sinal de saída é invariante sob pequenas variações da fonte de alimentação e desligamento. Apesar de preliminares, os resultados são encorajadores: O novo sistema de detecção de danos por radiação estabelece as bases para desenvolvimentos futuros relacionados a sensores magnéticos para monitorar a qualidade de campo dos onduladores sem removê-los da instalação. Além disso, instrumentos e aplicações destinadas a medir campo magnético através de sinais integrados podem utilizar o mesmo sistema de verificação proposto para propósitos de teste.

Palavras-chave: Anéis de armazenamento, danos por radiação, desmagnetização, geração de pulsos, laser de elétrons livres, magnetos permanentes, medições de campo magnético, medição de pulsos, medições elétricas, onduladores, processamento de sinais.

List of Figures

List of Tables

List of Acronyms

CMRR	Common-mode rejection ratio
DS	Downstream end
EM	Electromagnet
FEL	Free electron laser
HP	Hewlett-Packard
HXR	Hard X-ray (undulator)
LCLS	Linac Coherent Light Source
MMF	SLAC Magnetic Measurement Facility
NI	National Instruments
PM	Permanent magnet
RDDS	Radiation damage detection system
RMS	Root mean square
RMSE	Root mean square error
SASE	Self-amplified spontaneous emission
SLAC	Stanford Linear Acceleration Center
SR	Storage ring
SXR	Soft X-ray (undulator)
TLD	Thermoluminescent dosimeter
TTL	Transistor-transistor logic
US	Upstream end

List of Symbols

$\vec{B}$	Magnetic field vector
$\hat{B}$	On-axis peak field
B_{eff}	Effective magnetic field
B_{LA}	Maximum field on a pole of the lower array
B_0	Gap independent parameter
$\overline{B_0}$	Average over all B_0 associated with the poles covered by the coil
B_x	Horizontal magnetic field component
B_y	Vertical magnetic field component
B_z	Longitudinal magnetic field component
c	Speed of light
e	Electron charge
E	Electron energy
f_s	Sampling rate
g	Undulator gap
g_1	Initial gap
g_2	Final gap
I_{1x}	Horizontal first field integral
I_{1y}	Vertical first field integral
I_{2x}	Horizontal second field integral
I_{2y}	Vertical second field integral
K	K-parameter or undulator parameter
K_{eff}	Effective K-parameter
k_c	Effective area of the whole coil
k_s	Effective area of a coil segment
k_u	Longitudinal undulator wave number
k_x	Undulator wave number in x-axis
k_y	Undulator wave number in y-axis
L	Inner thickness of a coil segment
m_e	Electron rest mass
n_L	Number of flexble coil's layers
N_p	Number of undulator poles
N_s	Number of coil segments

N_w	Number of windings per coil segments
p	Undulator pole number
p_0	Fist pole in the undulator covered by the flexible coil
R_{on}	On-resistance of the switch (SPDT)
S	Slippage
S_p	Slippage between a whole number of undulator periods
t_H	Pulse high time
t_L	Pulse low time
t_T	Pulse total time
t_0	Pulse delay time
U	Undulators' length plus a margin
$\vec{v}$	Electron velocity vector
v_x	Horizontal electron velocity component
v_y	Vertical electron velocity component
v_z	Longitudinal electron velocity component
V_i	i-th corrected voltage sample
V_g	AC voltage between the undulator strongback and building ground
V_p	Pulse amplitude
V_{ref}	Voltage reference
W	Coil's width
x	Electron's horizontal position
xyz	Right-handed coordinate system
$\dot{x}$	Electron's horizontal slope
x_{exit}	Electron's horizontal exit position
$\dot{x}_{\text{exit}}$	Electron's horizontal exit angle
$\dot{x}_{\text{kick}}$	Electron's horizontal kick
y	Electron's vertical position
$\dot{y}$	Electron's vertical slope
y_{exit}	Electron's vertical exit position of the electron
$\dot{y}_{\text{exit}}$	Electron's vertical exit angle
z	Electron's longitudinal position
Z_{in}	Verification circuit input impedance
Z_{out}	Verification circuit output impedance
α_{max}	Electron's maximum deflection angle
γ	Lorentz factor
δ	Relative variation of the measurements with the verification system
δ_{lim}	Maximum relative variation δ
$\Delta B_0(p)$	B_0 parameter change for pole p
$\Delta\overline{B_0}$	$\overline{B_0}$ parameter change
Δg	Gap change
Δg_i	Gap change read during the i-th gap movement
Δg_R	Reference gap change
ΔK	K-parameter change
ΔK_{eff}	Effective K-parameter change
ΔL	Distance between adjacent coil's windings

Δz_p	Distance given by a whole number of undulator periods in z-axis
$\Delta\phi$	Flux change
$\Delta\psi$	Integrated voltage change
$(\Delta\psi/\psi)_{\text{det}}$	Minimum detectable ψ
ϵ_k	Relative deviation of the k-th flux change measurement with the RDDS
ε	Induced voltage
ε_{out}	Output voltage of the verification system
η	Gap-dependent constant
θ	Angle of observation
θ_{SR}	Radiation's natural opening angle
λ	Radiation wavelength
λ_u	Undulator period
μ	Average over all the samples taken from the verification system
μ_Ψ	Average over the samples of a set of pulses from the verification system
σ	Standard deviation over all the samples taken from the verification system
σ_n	Standard deviation over the samples of a set of pulses
σ_Ψ	Standard deviation of the mean μ_Ψ
ϕ	Total magnetic flux through the coil
ϕ_p	Magnetic flux through the region above the pole
ϕ_s	Magnetic flux through a coil segment
ϕ_w	Magnetic flux through the region above the coil's windings
ψ	Flux change (also referred as integrated voltage)
ψ_{samp}	Flux change sample
ψ_k	k-th flux change measurement
ψ'_{samp}	Flux change sample after gap correction
$\langle\psi\rangle$	Average over all flux change measurements
Ψ	Integrated voltage of a single pulse from the verification system
Ψ_{est}	Estimation of the integrated voltage of a single pulse
Ψ_i	Ideal integrated voltage sample of a single pulse
Ψ_m	Integrated voltage measurement ($\mu_\Psi \pm \sigma_\Psi$)
Ψ_{ref}	Reference integrated voltage sample of the verification system
Ψ_s	Integrated voltage sample of a single pulse from the verification system

Contents

Preface

Back in 2014, just after concluding my master's course in Electrical Engineering at the University of Campinas, I began pursuing a doctorate in the same area. Having acquired some experience on magnetic measurements for quadrupoles, the first proposal for the Ph.D. course was established: to develop a measurement system to characterize undulator magnet blocks inhomogeneities. By measuring inhomogeneities for single blocks, a sorting algorithm would allow minimizing the electron beam trajectory errors by picking the best arrangement of magnets. The project was initially planned for the undulators of the new Brazilian Synchrotron Light Source, Sirius. Although promising, time constraints became an issue for the continuity of such a project in Brazil.

Fortunately, the proposal was welcomed by the SLAC National Accelerator Laboratory, located in Menlo Park, California, USA. On that occasion, the head of the Magnetic Measurements Group (MMG), Dr. Zachary Wolf, not only demonstrated an interest in my academic profile but also assisted me throughout my application to attend an exchange program financed by CAPES[1]. Together, we slightly changed the original subject of my thesis proposal into a more attractive plan —successfully accepted and funded. Since the developments presented in this thesis come from a collaboration between the University of Campinas (Brazil) and SLAC, this preface aims to clarify the author's and SLAC fellows' contributions.

Radiation Damage Detection System (RDDS)

The MMG has been advancing in a novel approach for measuring field changes in un-

[1]Brazilian funding agency (Coordination for the Improvement of Higher Education Personnel).

dulator magnet blocks due to radiation exposure, more specifically in the context of the undulators of the new Linear Coherent Light Source (LCLS-II). Michael Rowen (Research Technical Manager at SLAC), provided the first suggestion of developing a system that detects magnetic flux changes in a flexible coil sensor. Scott Anderson (Staff Engineer at SLAC) sketched, quoted with local companies, and acquired coils' samples. He also wrote all the modules in C programming language to control the SXR undulator motion and to perform voltage acquisition. Initial checking tests with the undulator were performed by Scott as well. The company San Francisco Circuits™ produced and sold the flexible printed-circuit board (see figures 3.12 and 3.13). I wrote the codes in CVI/LabWindows (C programming language) to operate the NI PXIe-4464 as a voltmeter and to acquire voltage samples from the coil. Robert Pushor (Software Developer at SLAC) assisted me in programming the modules. I also designed the thermistor encapsulation and holder (see Fig. 3.16), improved the existing codes to perform offset corrections, took care of all the short- and long-term tests, and wrote codes in Matlab to analyze data and produce the figures to show the results. Ralph Colon (Accelerator Technologist III at SLAC) built the thermistor encapsulation and holder in a machine shop, and Luiz Juarez (Accelerator Technologist III at SLAC) helped with inserting and gluing the thermistor inside the holders by using epoxy resins. Yurii Levashov (Staff Engineer at SLAC) provided the on-axis peak field *versus* undulator gap. The data, illustrated in Fig. 3.26, is used in Section 3.7.

Chapter 3 of this thesis was written based on the manuscript titled "A novel in-situ radiation damage diagnostic system for undulators", authored by me, Scott Anderson, and Zachary Wolf. The paper was submitted and accepted on IEEE Transactions on Instrumentation and Measurements.

Verification System

Zachary Wolf proposed the idea of using an electrical signal generator in which its integrated voltage would be comparable with the typical signal measured with the RDDS. Then, we defined that the most straightforward and effective waveform would be a pulse, precisely set in amplitude and duration, and generated by combining a voltage reference integrated circuit with a high-precision timer module. The idea behind this project was to use this pulse

as a signal reference. If a change is detected with RDDS, then the pulse generator attests that the signal decreased due to radiation damage on the undulator, and not because of voltmeter drifts. From the initial idea, I designed the whole system, quoted the components and the board, and wrote the code in CVI/LabWindows (C programming language) to operate the NI PXI 6608 module. Tonee Smith (Staff Engineer at SLAC) meticulously reviewed the layout and proposed enhancements. Luiz Juarez soldered all the electronic components on the board (see Fig. 4.4). With the system ready to be tested, I performed all the tests and executed several improvements.

The manuscript titled "High-precision reference pulse generator for testing radiation damage in undulators", authored by me, Scott Anderson, and Zachary Wolf, has been recently submitted to IEEE Transactions on Instrumentation and Measurements. At the time this preface was written, the article was under review. Chapter 4 uses many sections of this paper.

Flip Coil System

As part of the activities planned for my visiting program at SLAC, the complete development of a flip coil system for field integrals measurements had been proposed by Zachary Wolf. Mostly under the supervision of Yurii Levachov, I designed all the parts of the system, quoted and purchased motorized and manual stages (linear and rotary), stage controllers, wires, etc. Ralph Colon built all the designed parts in a machine shop. Luiz Juarez proposed and implemented compelling ideas with the electrical connection between the rotary and fixed parts of the system, and assisted with setting the moving wire around the spool holders. Figures B.4 and B.5 show the final design.

The manuscript titled "Development and commissioning of a flip coil system for measuring field integrals", authored by me, has been recently presented at the 39th International Free Electron Laser Conference (FEL 2019), which took place in August of 2019 in Hamburg, Germany. I decided to include the contents of this conference paper in this thesis as Appendix B. Due to the limited number of pages allowed for conference papers, Appendix B is an extended version of the original manuscript.

Chapter 1

Introduction

LIGHT sources based on charged particle accelerators aim to produce high brilliance coherent radiation from infrared to X-rays range, leveraging investigation of the matter in several multidisciplinary themes [1–3]. Relativistic electrons produce radiation when a magnetic field deflects their trajectory, either with bending magnets or undulators. The latter is composed of an alternating series of magnetic poles, which raises the number of curvatures and reinforces the radiation. Independently of the type of magnet, this process is named *synchrotron radiation emission*. Two common types of light source facilities are the *storage rings* (SR) and the *free-electron lasers* (FEL). In an SR, the electron beam keeps circulating in a ring-type machine, while radiofrequency fields compensate for the energy loss due to synchrotron light emission. In a FEL, the electron beam is sent into successive undulator segments. The interaction between the electron bunch and radiation wave boosts the radiation's longitudinal coherence.

Planar undulators with periodic magnetic field create synchrotron radiation from relativistic charged particles at the resonance wavelength $\lambda = \lambda_u(1 + K^2/2 + \theta^2\gamma^2)/(2n\gamma^2)$, where λ_u is the magnetic field's period, θ is the observation angle, γ is the relativistic factor of the electrons, and n is the wavelength's harmonics. The variable K corresponds to the *undulator parameter*, being proportional to the undulator on-axis peak magnetic field [4]. In high gain FELs, dozens of undulator segments are aligned to produce X-rays by the Self-Amplified Spontaneous Emission (SASE) regime. The parameter K over all the segments must match in less than a few hundred parts per million, so all undulators are resonant at the same wavelength. As a result, the undulator's magnetic field has to be accurately tuned

prior to the installation in the tunnel.

As an attractive alternative for electromagnet (EM) undulators, permanent magnet (PM) undulators have been extensively used in FEL and SR facilities lately. As a matter of fact, new materials produced with samarium-cobalt ($SmCo_5$ and Sm_2Co_{17}) and neodymium-iron-boron ($Nd_2Fe_{14}B$) have reached higher remanent and coercive fields over the last few decades [2,4,5]. Along with technological progress, the exposure of permanent magnets in a radiation environment turned out to be an issue. As will be seen in Chapter 2, many FEL and SR facilities worldwide have experience radiation-induced changes in the magnetic properties of PM-based undulators [6–11]. Indeed, extensive research has shown how different types and energy of radiation induce PM demagnetization [12–20], and how the magnet's characteristics (i.e., coercive force, shape, material, magnetized direction, manufacturers, etc.) influence permanent magnets' behavior under radiation exposure [21–23]. Loss of magnetic field strength changes the undulator parameter K, which alters the emitted radiation spectral characteristics and, therefore, undulator's performance.

After tunnel installation in FELs, local magnetic field inspection becomes challenging; due to the dense packing of accelerator components and the number of segments (usually a few dozens), conventional techniques (e.g., Hall probes and induction sensors) can no longer be easily set up to characterize the magnetic field. Generally, thermoluminescent dosimeter (TLDs) and online readable RADFETs measure radiation doses near of each segment, serving as an indicator of magnetic field degradation levels. A more direct way to evaluate magnetic field quality after the installation of the undulator is based on measuring the light beam properties [24–27]. Even though promising, the precision of these techniques is primarily limited to the uncertainties of electron beam energy and observation angle. Furthermore, they require full access to the facility control and data acquisition systems.

Whenever an undulator loses (or is suspected to have lost) magnetic field strength above the limits (that is, the parameter K is out of the tolerance range), it must be removed from the tunnel for inspection and repair in a magnetic measurement laboratory, where the most common and appropriate techniques for characterizing undulator's field would be available [28]. The undulator transportation is, however, costly and time-consuming, due to undulator size and weight. Besides, the beam pipe has to be removed in some cases, leading

to long recovery times to reestablish the required vacuum level. The motivation behind this work is to be able to identify damage to an undulator without removing it from the tunnel.

This thesis presents the proposal and the first developments of a new technique for diagnosing radiation damage based on *in situ* magnetic measurements. The radiation damage detection system (RDDS) measures the flux change in a flexible printed-circuit coil attached to the undulator magnet array. The coil acts as a magnetic field probe: By varying the undulator gap (i.e., by either opening or closing the undulator jaws), the field in its aperture changes as an exponential function of the gap distance and, therefore, a voltage is induced in the coil's terminals. The larger the gap size, the smaller the magnetic field strength. For a well-defined and arbitrary gap distance change (for example, from g_1 to g_2), the difference of the magnetic flux linked with the coil between g_1 and g_2 is equivalent (in absolute values) to the time-integral of the induced voltage, as dictated by Faraday's law.

The integrated voltage defines a value related to the undulator magnet quality, given that the magnetic flux depends upon the magnetic field strength, For instance, if the magnets lose magnetic field strength as a consequence of absorbed doses, the integrated voltage will decrease proportionally, independently (in theory) of its strength. In practical terms, a short gap movement would generate weak signals and lead to low signal-to-noise ratio, whereas a long gap movement would not increase signal strength considerably due to the decreasing exponential profile of the field with respect to the gap. To establish the optimal undulator gap movement parameters g_1 and g_2, a compromise between low sampling time and high signal levels needs to be found. The time-integral of the induced voltage associated with the optimal gap change from g_1 to g_2 is defined as *reference integrated voltage*.

The RDDS was designed for and tested with the soft X-rays undulators of the new Linac Coherent Light Source (LCLS-II), which have been checked and tuned at the SLAC National Accelerator Laboratory. Regarding these undulators, tolerance studies of the FEL process led to a tolerance budget for the undulator parameter of individual segments of $\pm 3 \times 10^{-4}$ (± 300 ppm). In other words, for a given operational gap, its correspondent undulator parameter K must be set within a limit error of $\pm 0.03\%$. As will be described in more detail in Chapter 2, K depends almost linearly on the on-axis peak magnetic field. Based upon the K tolerance aforementioned and the relationship between magnetic field, magnetic flux,

magnetic flux change, and integrated voltage, we establish that the RDDS must detect integrated voltage changes with relative resolution better than 0.01% (100 ppm) in relation to the reference integrated voltage, so the system has enough sensitivity to detect field changes in the same order.

The overall structure of this manuscript takes the form of five chapters. Chapter 2 overviews the basis of undulators and state of the art on beam-based undulator parameter measurements. Loss of magnetic field strength experienced by different light sources around the globe and the challenges of the new LCLS-II will also be the subject of Chapter 2. The principle, development, results, and analysis of the proposed system for *in situ* radiation damage detection are explained in Chapter 3. A verification circuit designed for testability of the RDDS will be the subject of Chapter 4. Finally, Chapter 5 discusses the key findings, strengths and limitations of the proposed approaches, and future directions.

Before moving to the next chapter, let us provide clarification on some of the common terms used throughout this thesis. The acronym "LCLS-I" (or simply "LCLS") will refer to the current Linac Coherent Light Source, which has been in operation since 2009. The upgrade project of the LCLS-I will be indicated with the acronym "LCLS-II" (the main construction activities will be completed in 2021 [29]). In some facilities, the undulator system is composed of many aligned segments of undulators. We will use the words "undulator(s)" and "segment(s)" to mean the device that produces the periodic magnetic field. The whole flexible coil is composed of many "winding segments". Thus, the word "segment" will also denote the windings that cover one pole. The different meanings of "segment" will be clear according to the context. Quite often, terms related to relative changes will appear, which may be expressed in ppm (parts per million), percentage, or scientific notation. For instance, 100 ppm is equivalent of 0.01%, or simply 10^{-4}. The "undulator parameter" K is also known in the literature as "K-parameter", "K-value" and "deflection parameter", and will be used interchangeably here. Formally, B represents the magnetic flux density (sometimes known as magnetic induction). All the chapters will denote B and all its related variables (e.g., $\vec{B}$, $\hat{B}$, B_{eff}, etc.) as "magnetic field strength", or simply "magnetic field". The Greek letter "psi" will be used to represent integrated voltage. The integrated voltage of the signal induced in the flexible printed-circuit coil of the RDDS will be represented with the lower-case psi (ψ),

whereas the time-integral of the signal generated from the verification circuit will be written as the upper-case psi (Ψ). For both, subscripts will express their associated variables, usually given in Vs. Regarding the RDDS coil, it should be pointed out that time-integral of the induced voltage represents the magnetic flux change (Wb or Tm^2 in the SI system) linked in the coil. Therefore, the variable ψ will also mean the magnetic flux difference between two given instants (notice that Wb and Tm^2 are dimensionally equivalent to Vs).

Chapter 2

Fundamentals of Undulators and Literature Review

UNDULATOR is a device that creates a periodic magnetic field and forces relativistic charged particles that go through the device to wiggle and emit electromagnetic radiation, as briefly mentioned in Chapter 1. The present chapter aims to go deeper into the fundamental concepts related to undulators, including, but not limited to: equations of electron beam motion through magnetic fields, the formal definition of undulator parameter and undulator equation, and the available hardware technology. Moreover, this chapter compiles the magnetic field degradation observed in many facilities worldwide due to radiation exposure, the beam-based undulator parameter measurement techniques developed in LCLS-I and European XFEL, and the challenges for the new LCLS-II.

2.1 Equation of Motion

The motion of an electron in a magnetic field is governed by Lorentz equation,

$$\vec{F} = e\,\vec{v} \times \vec{B}, \tag{2.1}$$

where $\vec{F}$ is the force, e is the electron charge, $\vec{v}$ is the electron velocity, and $\vec{B}$ is the magnetic field strength. Using the definition of momentum for a relativistic electron,

$$\vec{F} = \frac{\mathrm{d}\,\vec{p}}{\mathrm{d}t} = \frac{\mathrm{d}}{\mathrm{d}t}(\gamma m_e\,\vec{v}), \tag{2.2}$$

where $\vec{p}$ is the momentum of the electron, m_e is the electron rest mass, and γ is the Lorentz factor, given by

$$\gamma = \frac{1}{\sqrt{1 - \left(\frac{|\vec{v}|}{c}\right)^2}} = \frac{E}{m_e c^2}, \tag{2.3}$$

with c being the speed of light. As expressed in (2.3), γ is also represent as the ratio of the electron's energy, E, to its rest mass energy, $m_e c^2$. Neglecting energy losses due to the radiation emitted by the electron, γ and m_e do not change because of $\vec{B}$. Thus, both variables can be moved out of $\mathrm{d}/\mathrm{d}t$ in (2.2). Combining (2.1) and (2.2),

$$\frac{\mathrm{d}}{\mathrm{d}t}\vec{v} = \frac{e}{\gamma m_e}\vec{v} \times \vec{B}. \tag{2.4}$$

Figure 2.1 illustrates the coordinate system used for the explanations that follow, in which z is taken as the direction towards the electron moves along the undulator, y is upward direction, and x defines xyz as a right-handed coordinate system.

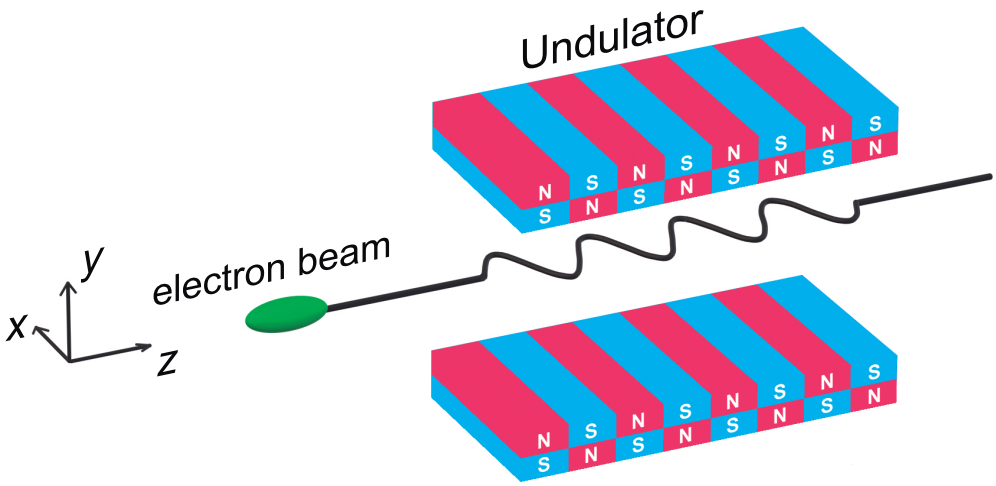

Figure 2.1: Right-handed coordinate system used to represent magnetic field and the electron trajectory within the undulator [30].

On the undulator axis ($x = 0$ and $y = 0$), $B_z = 0$. Even considering a non-zero field component, B_z points towards the main motion direction of the electron, so it has no first-order effects and can be neglected. The main velocity component is v_z, which produces v_x

and v_y along the undulator length. For a relativistic electron, we may assume $v_z \gg v_x$, $v_z \gg v_y$, and v_z constant. With those assumptions, (2.4) becomes

$$\frac{\mathrm{d}}{\mathrm{d}t}v_x = \frac{\mathrm{d}}{\mathrm{d}t}\frac{\mathrm{d}x}{\mathrm{d}t} = \frac{\mathrm{d}^2x}{\mathrm{d}t^2} = -\frac{e}{\gamma m_e}B_y v_z \tag{2.5}$$

$$\frac{\mathrm{d}}{\mathrm{d}t}v_y = \frac{\mathrm{d}}{\mathrm{d}t}\frac{\mathrm{d}y}{\mathrm{d}t} = \frac{\mathrm{d}^2y}{\mathrm{d}t^2} = \frac{e}{\gamma m_e}B_x v_z. \tag{2.6}$$

It is useful to change variables from time to electron's position in (2.5) and (2.6). Let us represent $\mathrm{d}x/\mathrm{d}t$ in terms of the chain rule (x is a function of t and z). Given the relationship $\mathrm{d}z/\mathrm{d}t = v_z$ with v_z constant,

$$\frac{\mathrm{d}x}{\mathrm{d}t} = \frac{\mathrm{d}x}{\mathrm{d}z}\frac{\mathrm{d}z}{\mathrm{d}t} = \frac{\mathrm{d}x}{\mathrm{d}z}v_z. \tag{2.7}$$

Applying $\mathrm{d}/\mathrm{d}t$ in (2.7) to obtain $\mathrm{d}^2x/\mathrm{d}t^2$ and manipulating its denominator,

$$\frac{\mathrm{d}^2x}{\mathrm{d}t^2} = \frac{\mathrm{d}}{\mathrm{d}t}\left(\frac{\mathrm{d}x}{\mathrm{d}t}\right) = \frac{\mathrm{d}}{\mathrm{d}t}\left(\frac{\mathrm{d}x}{\mathrm{d}z}v_z\right) = \frac{\mathrm{d}}{\mathrm{d}z}\left(\frac{\mathrm{d}x}{\mathrm{d}t}v_z\right) \tag{2.8}$$

Replacing (2.7) in the rightmost side of (2.8) to eliminate the $\mathrm{d}t$ term,

$$\frac{\mathrm{d}^2x}{\mathrm{d}t^2} = \frac{\mathrm{d}}{\mathrm{d}z}\left(\frac{\mathrm{d}x}{\mathrm{d}z}v_z^2\right) \tag{2.9}$$

Therefore,

$$\frac{\mathrm{d}^2x}{\mathrm{d}t^2} = \frac{\mathrm{d}^2x}{\mathrm{d}z^2}v_z^2. \tag{2.10}$$

Similarly for y, the same procedure gives

$$\frac{\mathrm{d}^2y}{\mathrm{d}t^2} = \frac{\mathrm{d}^2y}{\mathrm{d}z^2}v_z^2. \tag{2.11}$$

Replacing (2.10) in (2.5) and (2.11) in (2.6), and using Newton's notation, we reach to the following set of equations of motion that are commonly seen in the literature [31–34]:

$$\frac{\mathrm{d}^2x}{\mathrm{d}z^2} = \ddot{x} = -\frac{e}{\gamma m_e v_z}B_y \tag{2.12}$$

$$\frac{\mathrm{d}^2 y}{\mathrm{d}z^2} = \ddot{y} = \frac{e}{\gamma m_e v_z} B_x. \tag{2.13}$$

By integrating (2.12) and (2.13) along z, we find the horizontal and vertical slopes of the electron trajectory $\dot{x}(z)$ and $\dot{y}(z)$, respectively, as

$$\dot{x}(z) = \int_{z_0}^{z} \ddot{x}(z_1)\,\mathrm{d}z_1 = \int_{z_0}^{z} -\frac{e}{\gamma m_e v_z} B_y(z_1)\,\mathrm{d}z_1 = -\frac{e}{\gamma m_e v_z}\int_{z_0}^{z} B_y(z_1)\,\mathrm{d}z_1 \tag{2.14}$$

and

$$\dot{y}(z) = \int_{z_0}^{z} \ddot{y}(z_1)\,\mathrm{d}z_1 = \int_{z_0}^{z} \frac{e}{\gamma m_e v_z} B_x(z_1)\,\mathrm{d}z_1 = \frac{e}{\gamma m_e v_z}\int_{z_0}^{z} B_x(z_1)\,\mathrm{d}z_1, \tag{2.15}$$

where $\ddot{x}(z_0) = \ddot{y}(z_0) = 0$. Integrating again to find the trajectories $x(z)$ and $y(z)$,

$$\begin{aligned} x(z) &= \int_{z_0}^{z} \dot{x}(z_2)\,\mathrm{d}z_2 = \int_{z_0}^{z} \left[-\frac{e}{\gamma m_e v_z}\int_{z_0}^{z_2} B_y(z_1)\,\mathrm{d}z_1\right]\mathrm{d}z_2 \\ &= -\frac{e}{\gamma m_e v_z}\int_{z_0}^{z}\int_{z_0}^{z_2} B_y(z_1)\,\mathrm{d}z_1\,\mathrm{d}z_2 \end{aligned} \tag{2.16}$$

and

$$\begin{aligned} y(z) &= \int_{z_0}^{z} \dot{y}(z_2)\,\mathrm{d}z_2 = \int_{z_0}^{z} \left[\frac{e}{\gamma m_e v_z}\int_{z_0}^{z_2} B_x(z_1)\,\mathrm{d}z_1\right] dz_2 \\ &= \frac{e}{\gamma m_e v_z}\int_{z_0}^{z}\int_{z_0}^{z_2} B_x(z_1)\,\mathrm{d}z_1\,\mathrm{d}z_2, \end{aligned} \tag{2.17}$$

where $\dot{x}(z_0) = \dot{y}(z_0) = 0$. Once $B_x(z)$ and $B_y(z)$ are precisely and accurately measured along the whole extension of the undulator, the electron trajectory and the slope can be calculated by numerical integration. An important set of parameters that come out from (2.14)–(2.17) is called *field integrals*.

2.2 First and Second Field Integrals

It is common to refer to an undulator as an "insertion device". The name was coined in the context of early SR facilities, in which the "device" that makes the electron beam to wiggle could be "inserted" in free straight sections, almost independently of the ring itself. From an ideal perspective, the electron beam enters and leaves the undulator at the same

position and angle. The same feature is desirable in a FEL; the segments must have the least possible effect on the electron beam exit angle and position.

Let U be the length in z that covers an undulators' length plus a margin to guarantee that the end effects are taken into account. From (2.14) and (2.15), the vertical and horizontal exit angles are

$$\dot{x}_{\text{exit}} = -\frac{e}{\gamma m_e v_z} \int_{z_0}^{z_0+U} B_y(z_1)\, \mathrm{d}z_1 \tag{2.18}$$

and

$$\dot{y}_{\text{exit}} = \frac{e}{\gamma m_e v_z} \int_{z_0}^{z_0+U} B_x(z_1)\, \mathrm{d}z_1, \tag{2.19}$$

respectively. Similarly, (2.16) and (2.17) allow us provide the vertical and horizontal exit positions, respectively given by

$$x_{\text{exit}} = -\frac{e}{\gamma m_e v_z} \int_{z_0}^{z_0+U} \int_{z_0}^{z_2} B_y(z_1)\, \mathrm{d}z_1\, \mathrm{d}z_2 \tag{2.20}$$

and

$$y_{\text{exit}} = \frac{e}{\gamma m_e v_z} \int_{z_0}^{z_0+U} \int_{z_0}^{z_2} B_x(z_1)\, \mathrm{d}z_1\, dz_2. \tag{2.21}$$

The first and second field integrals for x and y components are explicitly defined as

$$I_{1x} = \int_{z_0}^{z_0+U} B_x(z_1)\, \mathrm{d}z_1 \tag{2.22}$$

$$I_{1y} = \int_{z_0}^{z_0+U} B_y(z_1)\, \mathrm{d}z_1 \tag{2.23}$$

$$I_{2x} = \int_{z_0}^{z_0+U} \int_{z_0}^{z_2} B_x(z_1)\, \mathrm{d}z_1\, \mathrm{d}z_2 \tag{2.24}$$

$$I_{2y} = \int_{z_0}^{z_0+U} \int_{z_0}^{z_2} B_y(z_1)\, \mathrm{d}z_1\, \mathrm{d}z_2. \tag{2.25}$$

Therefore,

$$\dot{x}_{\text{exit}} = -\frac{e}{\gamma m_e v_z} I_{1y} \tag{2.26}$$

$$\dot{y}_{\text{exit}} = \frac{e}{\gamma m_e v_z} I_{1x} \tag{2.27}$$

$$x_{\text{exit}} = -\frac{e}{\gamma m_e v_z} I_{2y} \tag{2.28}$$

$$y_{\text{exit}} = \frac{e}{\gamma m_e v_z} I_{2x}. \tag{2.29}$$

Equations (2.26)–(2.29) justifies the desire of having the first and second field integrals equal to zero; the lower the value of the field integrals, the less the undulator disturbs the electron beam. Nevertheless, these integrals are never truly zero because of the existence of tolerances in block positioning and sizes, and the quality of materials. The resultant errors in the magnetic field [4] needs to be properly characterized. Appendix B describes in detail a system we developed to measure field integrals at SLAC.

2.3 Undulator Parameter

Consider that the undulator only deflects the electron in the horizontal plane xz ($y = 0$) due to the existence of a perfect sinusoidal vertical magnetic field on the midplane independent of x given by

$$B_y(z) = \hat{B} \cos\left(\frac{2\pi z}{\lambda_u}\right), \tag{2.30}$$

where $\hat{B}$ is the on-axis peak field and λ_u is the undulator's period. Since $B_x = 0$, $y(z)$, $\dot{y}(z)$ and $\ddot{y}(z)$ are zero as well. Substituting (2.30) in (2.12), (2.14) and (2.16),

$$\ddot{x}(z) = -\frac{e}{\gamma m_e v_z} \hat{B} \cos\left(\frac{2\pi z}{\lambda_u}\right) \tag{2.31}$$

$$\dot{x}(z) = -\frac{e}{\gamma m_e v_z} \left(\frac{\lambda_u}{2\pi}\right) \hat{B} \sin\left(\frac{2\pi z}{\lambda_u}\right) \tag{2.32}$$

$$x(z) = \frac{e}{\gamma m_e v_z}\left(\frac{\lambda_u}{2\pi}\right)^2 \hat{B}\cos\left(\frac{2\pi z}{\lambda_u}\right). \tag{2.33}$$

The angular distribution of the radiation emitted by an accelerating relativistic electron is confined to a very narrow cone in the direction of the electron motion. More specifically, the natural opening angle θ_{SR} for the emitted synchrotron radiation is approximately $1/\gamma$ [35]. Let θ_{SR} be equal $1/\gamma$. From (2.32), the maximum deflection angle is

$$\alpha_{\max} = -\frac{1}{\gamma}\frac{e\lambda_u\hat{B}}{2\pi m_e v_z} = -\theta_{SR}\frac{e\lambda_u\hat{B}}{2\pi m_e v_z}. \tag{2.34}$$

The so-called *K-parameter* is defined as

$$K = \frac{\alpha_{\max}}{\theta_{SR}} = -\frac{e\lambda_u\hat{B}}{2\pi m_e v_z}. \tag{2.35}$$

Given that the electron charge e, the electron rest mass m_e and the electron velocity v_z are constant (we may consider $v_z = c$ here), a practical equation expresses the undulator parameter as

$$K = 93.36\hat{B}\lambda_u, \tag{2.36}$$

where K is dimensionless, $\hat{B}$ is given in T and λ_u in m.

If $K \simeq 1$, then the electron trajectory overlaps the emitted radiation, and the interference effects occur, leading to narrow energy bands. This is the case for an *undulator*. If $K \gg 1$, little overlap occurs, and a wide energy spectrum of radiation is observed. This is the case for a *wiggler*. Although both undulators and wigglers are widely used for FEL and SR, for the sake of simplicity, the remaining text of this chapter refers only to undulators.

Equation (2.36) comes from a pure sinusoidal field undulator, which is different than an actual undulator. It is worth to define the concept of effective K-parameter, K_{eff}.

2.4 Slippage and Effective Paramenters

The electron beam travels towards z with velocity v_z smaller than the speed of the electromagnetic radiation emitted by the electron, the speed of light c. The *slippage* $S(z)$ is

defined as the distance between the radiation wavefront and electron. It is possible to prove that [34]

$$S(z) = \int_{z_0}^{z} \left(\frac{1}{2\gamma^2} + \frac{\dot{x}^2}{2} \right) \mathrm{d}z, \tag{2.37}$$

where $\dot{x}(z_0) = 0$. Let z be a whole number of undulator periods apart from z_0 and let us define $\Delta z_p = z - z_0$ (thereby, $\Delta z_p = n\lambda_u$). Consider the electron trajectory for a pure sinusoidal field with undulator parameter K. Replacing (2.32) in (2.37) and solving the integral,

$$S_p = \frac{1}{2\gamma^2} \left(1 + \frac{K^2}{2} \right) \Delta z_p, \tag{2.38}$$

where S_p is the slippage between two points in the z-axis that are a whole number of λ_u apart from each other. Equations (2.37) and (2.38) are demonstrated in Appendix C. By measuring $B_y(z)$ point by point within the undulator, $\dot{x}^2$ can be calculated by applying (2.14), which will correspond to the measured slippage as a function of z. Let Ω_{fit} be the slope of the straight line

$$S(z) = \Omega_{fit} \Delta z \tag{2.39}$$

that best fits $S(z)$ *versus* Δz with $\Delta z = z - z_0$, as illustrated in Fig. 2.2. By contrasting (2.38) and (2.39), the slippages of an actual and a sinusoidal magnetic field undulators with $K = K_{\text{eff}}$ along the z-axis would have a very similar profile when

$$\Omega_{fit} = \frac{1}{2\gamma^2} \left(1 + \frac{K^2}{2} \right), \tag{2.40}$$

resulting in

$$K_{\text{eff}} = \sqrt{4\gamma^2 \Omega_{fit} - 2}. \tag{2.41}$$

From (2.35) and (2.41), we may define the effective on-axis peak field as

$$B_{\text{eff}} = -\frac{2\pi m_e v_z K_{\text{eff}}}{e\lambda_u}. \tag{2.42}$$

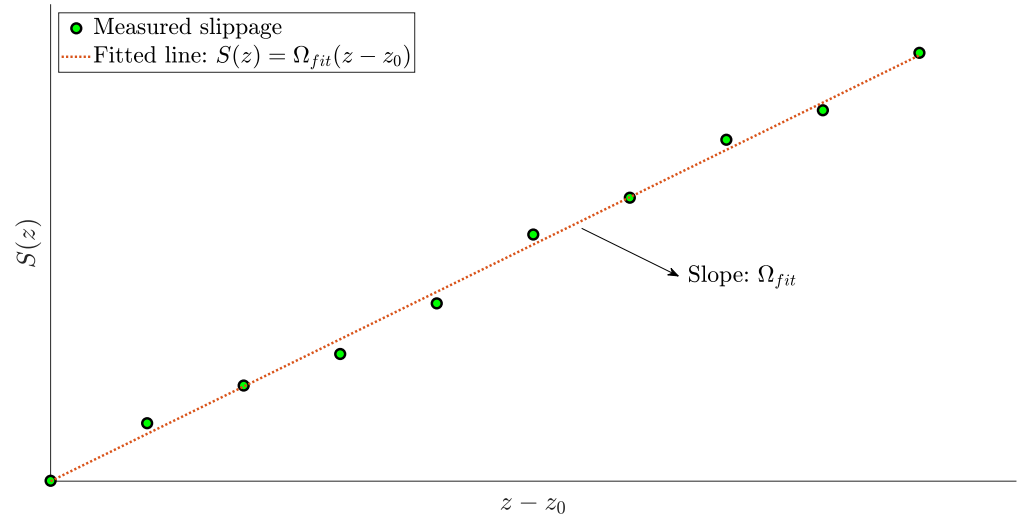

Figure 2.2: Representation of the slippage measurement as a function of the z in an actual undulator. The slope Ω_{fit} is used to calculate the effective undulator parameter K_{eff}.

The definition of K_{eff} explained in this section is based on comparing the K-value of an actual undulator and an ideal undulator (pure sinusoidal field) with $K = K_{\text{eff}}$. This interpretation guarantees that the spectral harmonics expected from an ideal magnetic field with K-parameter equal K_{eff} overlap with spectral harmonics numerically deduced by magnetic measurement means [34, 36].

Let us now turn to the equation that provides the relationship between the radiation wavelength and the undulator's features.

2.5 Undulator Equation

Consider that the electron beam emits, at the position $z = Z_1$, electromagnetic radiation with angle θ in relation to z-axis and with wavelength λ, as shown in Fig. 2.3a. Equation (2.38) demonstrates that when the electron travels one undulators' period λ_u, the wavefront emitted at $z = Z_1$ will have traveled

$$\frac{1}{2\gamma^2}\left(1 + \frac{K^2}{2}\right)\lambda_u + \lambda_u.$$

If the separation between the two wavefronts is a whole number of wavelength as illustrated in Fig. 2.3b, then constructive interference takes place. Mathematically,

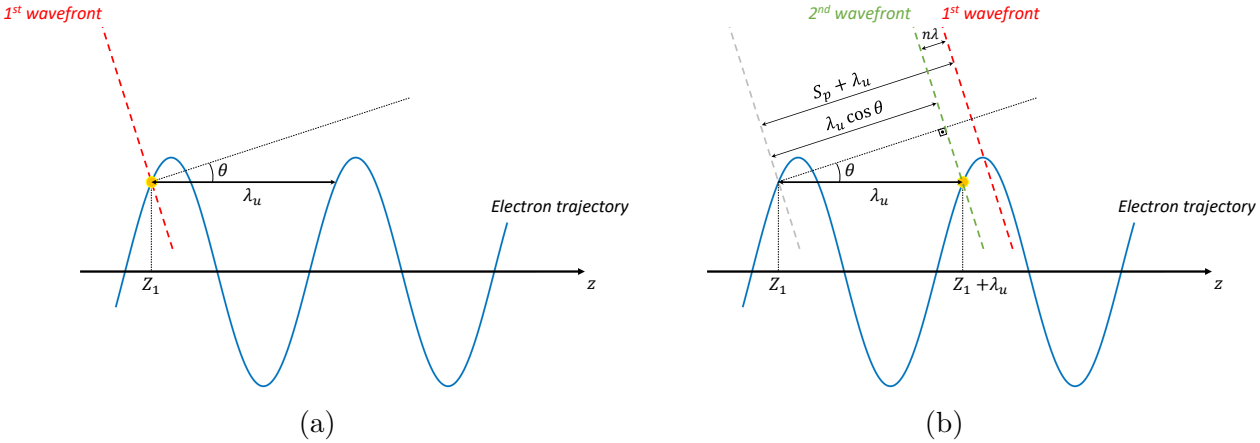

Figure 2.3: Electron trajectory through an undulator emitting radiation at the point (a) $z = Z_1$ and (b) $z = Z_1 + \lambda_u$, in such a way that constructive interference happens.

$$n\lambda = \frac{1}{2\gamma^2}\left(1 + \frac{K^2}{2}\right)\lambda_u + \lambda_u - \lambda_u \cos\theta. \tag{2.43}$$

It is possible to simplify (2.43) by using the trigonometric identity $1 - \cos\theta = \sin^2(\theta/2)$ and the approximation $sin\theta \approx \theta$, given that θ is small. By doing so,

$$\begin{aligned} n\lambda &= \frac{1}{2\gamma^2}\left(1 + \frac{K^2}{2}\right)\lambda_u + \lambda_u(1 - \cos\theta) \\ &= \frac{1}{2\gamma^2}\left(1 + \frac{K^2}{2}\right)\lambda_u + \lambda_u \sin^2\left(\frac{\theta}{2}\right) \\ &= \frac{1}{2\gamma^2}\left(1 + \frac{K^2}{2}\right)\lambda_u + \lambda_u \frac{\theta^2}{4} \\ &= \frac{\lambda_u}{2\gamma^2}\left(1 + \frac{K^2}{2} + \theta^2\gamma^2\right). \end{aligned} \tag{2.44}$$

Therefore,

$$\lambda = \frac{\lambda_u}{2n\gamma^2}\left(1 + \frac{K^2}{2} + \theta^2\gamma^2\right). \tag{2.45}$$

This expression is known as *undulator equation*.

It is interesting to remark some of the main implications of the undulator equation. Since the electron beam energy is usually on the order of GeV, γ is typically a few thousand. Undulators with a period of a few dozens of millimeters will produce light with a wavelength on the order of nanometers. Besides, the undulator equation reveals the interest for a high

peak field; for a fixed K-parameter, the higher the on-axis peak field, the smaller the undulator period [see (2.36)] and, consequently, the smaller the photon beam wavelength. It should also be noted that K-value defines the photon beam properties for given parameters λ_u, γ, and θ. For FEL facilities based on SASE — where dozens of undulators are aligned withing very tight mechanical and field quality specifications — K-parameters must match in less than a few hundred parts per million among all the segments[1]. The tolerance for K-parameter is commonly represented as its maximum allowable variation ΔK_{eff} with respect to its operational value K_{eff} (i.e., $\Delta K_{\text{eff}}/K_{\text{eff}}$).

So far, this thesis has focused on the basis of the undulator theory. The following section will discuss the hardware technology available to build such devices.

2.6 Electromagnet and Permanent Magnet Undulators

Typically, an undulator segment length lies between 0.5 m and 5 m [5]. Two common designs are employed to create the periodic profile of the field: electromagnet-based (EM-based) and permanent magnet-based (PM-based). The EM undulator excites the magnetic field from a current in its conductors. Apart from the much higher currents and current densities, superconducting undulators fall into the EM-based type. Although more complex and pricey, superconducting devices allow reaching higher fields with short periods, being both desirable features for an undulator, as explained in the previous section.

Figure 2.4 illustrates the basic layout of an EM-based undulator. This type of device is capable of generating magnetic fields that quickly change over time, which is impractical to achieve with motor driven PM-based undulators. The rapidly time-varying magnetic field has been explored for helical undulators, enabling fast switching between different polarization states of the radiation [4]. Such ability is essential for many applications in the study of structural, electronic and magnetic properties of materials. For instance, several experiments require specific circularly polarized radiation to probe electronic spin in materials.

[1]There are additional tuning considerations that must be satisfied in SASE-based FELs to guarantee optimal operation. For instance, it is important to ensure that the phase error between the electron beam and the radiation is minimum across each segment. Furthermore, the first and second field integrals (see Section 2.2) must be smaller than specific tolerances.

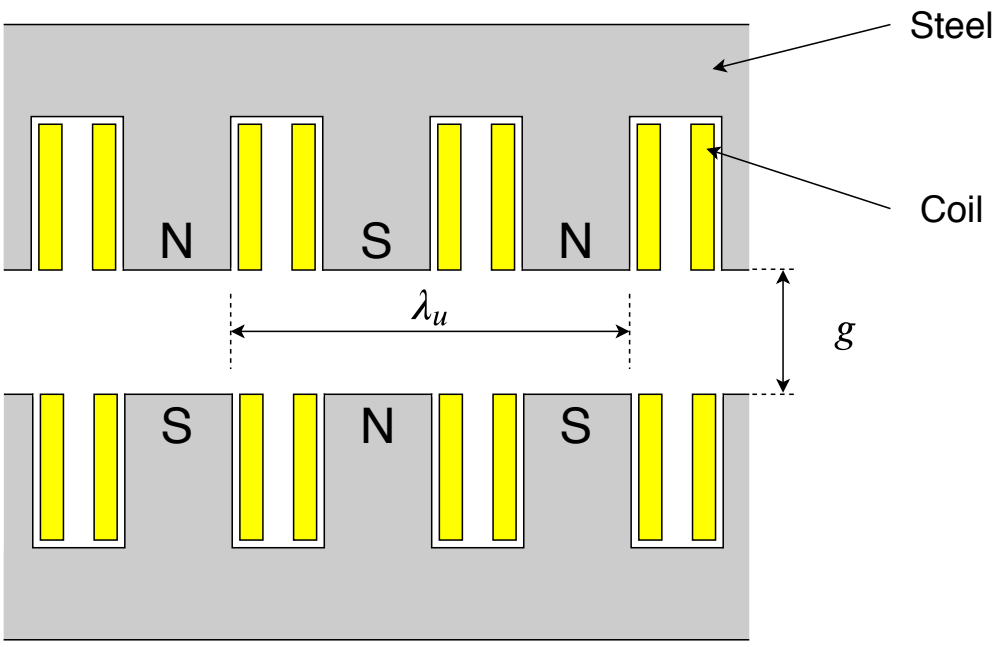

Figure 2.4: Two-dimensional sketch showing a fraction of an electromagnet-based undulator.

PM-based undulators are devices composed of rare-earth PM material, mostly NdFeB and SmCo. As the name suggests, a Pure Permanent Magnet (PPM) undulator is a device that combines only permanent magnets to produce the magnetic field. The magnetic field is generated from arrays of PMs. The easy axis — the direction of alignment of the magnet moments in the material's lattice — of each magnet block rotates by 360° per undulator period along the electron beam axis, as shown in the right side of Fig. 2.5.

An alternative for PPMs is the hybrid undulator type, which combines iron poles (or some other high permeability material) with PM materials (see the left side of Fig. 2.5). In comparison with PPM systems, the hybrid holds two advantages. First, the field depends more on the geometry of the pole than the PM material quality (such a feature is not valid for PPMs). Second, hybrid-type devices reach stronger magnetic fields by compressing the poles, since the high permeability material concentrates the flux. As a result of the non-linear behavior of such materials, analytical equations for the magnetic field within the undulator are no longer available. Even so, numerical codes can be used for this task. Commonly applied for both PPMs and hybrids undulators, the accepted expression fits [37–42]

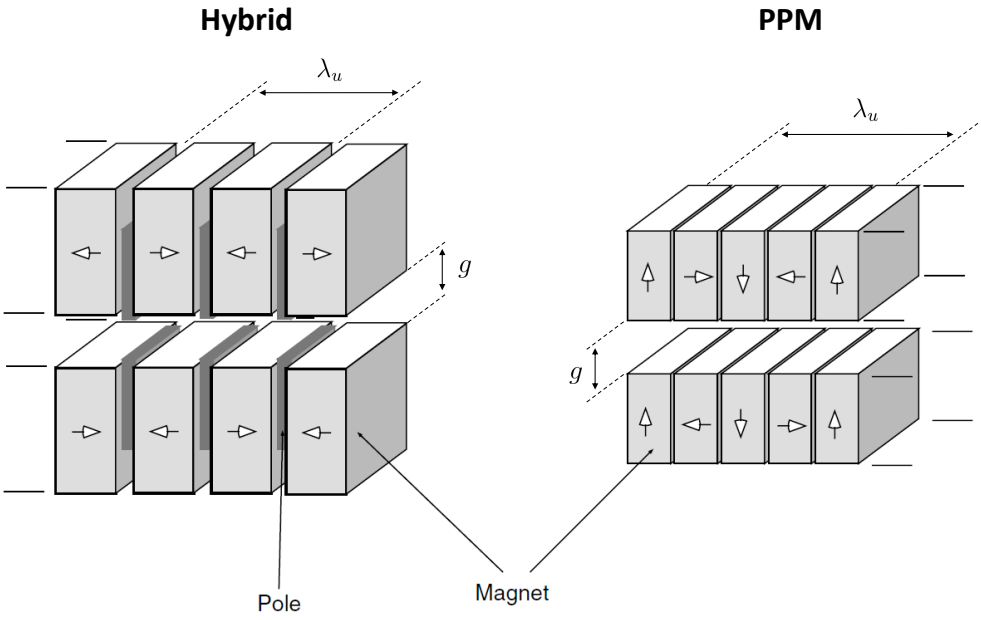

Figure 2.5: Schematic showing a fraction of a hybrid and pure permanent magnet undulator [2].

$$\hat{B} = B_0 \exp\left[a\left(\frac{g}{\lambda_u}\right) + b\left(\frac{g}{\lambda_u}\right)^2\right], \tag{2.46}$$

where B_0 is a gap-independent parameter given in T that depends on magnet strength, and a and b are dimensionless. The empirical parameters B_0, a, and b depend upon details of the magnets' and poles' design, such as dimensions and material properties. Equation (2.46) also reveals an outstanding feature of variable-gap undulators compared to fixed-gap devices: By mechanically changing the gap, it is possible to change the photon beam wavelength, due to the gap-dependence of the on-axis peak field and its relationship with K-parameter. Such an aspect makes experiments highly robust, which justifies the interest of variable-gap devices for lasing technology on the latest FEL facilities.

In the context of FEL and SR facilities, PM technology is well established; it is estimated that more than 90% of all undulators and wigglers are developed with PM materials [5]. In comparison with EM undulators, PM-based devices have a distinct advantage: They provide magnetic flux without the need for electrical currents. Therefore, there are no operation expenses in terms of electric power. In contrast, the electrical consumption of EM undulators may reach hundreds of kW [4].

Nonetheless, PM-based undulators may experience loss of the magnetic field strength as a consequence of many factors, which affects performance and is usually an undesirable event. For instance, temperature changes and radiation-induced demagnetization may change the peak field and, consequently, K_{eff}. Regarding the latter, many facilities have reported radiation damage in undulators in the last few decades, which will be the subject of the next section. The temperature effect in undulators will be mention in Subsection 3.5.2.

2.7 Radiation Damage Observed in FEL and SR Facilities

A considerable amount of literature has been published on the hazards of radiation exposure in PM materials. This section aims to present the results reported by some of the FEL and SR facilities regarding the loss of magnetic field strength in undulators. Figure 2.6 compiles original plots obtained directly from the literature. The references are shown in the figure's caption. Each of these results will be examined in the subsections that follow.

2.7.1 APS

The **A**dvanced **P**hoton **S**ource (APS, Argonne, Illinois, USA) is a 7 GeV storage ring synchrotron light source that accelerates positrons. The storage ring has 1104 m in circumference and uses 34 sectors to emit light from undulators and wigglers. The APS Sector 3 beamline offers High-Resolution X-ray Scattering for users. It operates an undulator with a period of 27 mm (named U27). In 2001 this device was removed from the tunnel for inspection. Figure 2.6a shows the peak field measurements taken in 1997 and 2001 [6]. The leftmost and rightmost side of the figure corresponds to the downstream (DS) and upstream (US) ends, respectively. Radiation dosimeters recorded uncommon high doses on this device after retuning the undulator, which prompted its removal for checkups. As shown in Fig. 2.6b, further damage was observed.

2.7.2 PETRA III

The **P**ositron **E**lectron **T**andem **R**ing **A**nlage (PETRA III, Hamburg, Germany) is a 3$^{\text{rd}}$ generation storage ring that operates with electrons at a beam energy of 6 GeV. Several

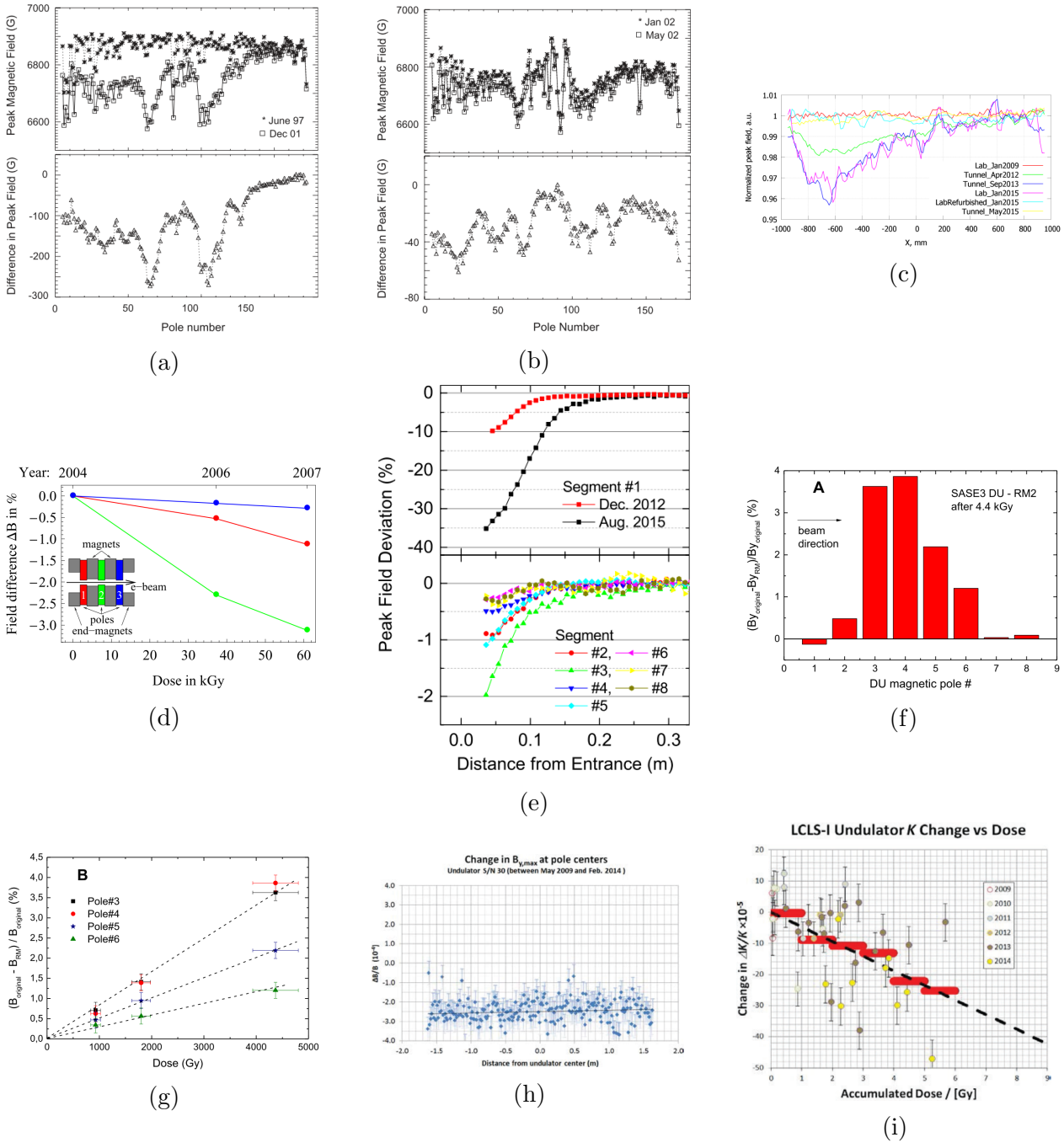

Figure 2.6: Magnetic field degradation observed in different facilities worldwide. (a) Undulator U27 at APS between 1997 and 2001 [6]. (b) Undulator U27 at APS after uncommon high doses in 2002 [6]. (c) Undulator U29 at PETRA III between 2009 and 2015 [7]. (d) Test undulator at FLASH between 2004 and 2007 [8]. (e) Eight first undulator segments at SACLA between 2012 and 2015 [9]. (f) Diagnostic undulator at Eu.XFEL after exposure of 4.4 kGy [10]. (g) Diagnostic undulator field change accumulated dose at Eu.XFEL [10]. (h) Segment S/N 30 at LCLS between 2009 and 2014 [11]. (i) K-parameter change *versus* accumulated dose at LCLS betwwen 2009 and 2015 [11].
Note: All the figures were reprinted from the original manuscripts cited in this caption.

hybrid undulators experienced demagnetization effects, which has been observed by spectral degradation and direct magnetic field measurements [7].

Figure 2.6c shows the reduction levels of peak field of the undulator U29 over more than 6 years of operation, reaching a loss of up to 4%. Operating since the beginning of 2009, the U29 is a 2m-long device with a nominal peak field of 0.81 T and 29 mm period length ($K = 2.2$). On the US end (leftmost side of Fig. 2.6c), the pattern of demagnetization increases after the first poles. Towards the DS end (rightmost side of the figure), the field reduction level decreases slowly. Between the measurements taken in 2009 and 2015, two additional tests reveal that the demagnetization has occurred over time.

2.7.3 FLASH

The **F**ree-electron-**Las**er in **H**amburg (FLASH, Hamburg, Germany) is a high-gain free-electron laser that generates ultra-short femtosecond laser pulses in the extreme ultraviolet (EUV) and soft X-ray wavelength range. It has two undulator lines: FLASH1 and FLASH2, being the latter the most recent one.

The FLASH1 undulator system consists of 6 fixed gap hybrid type undulators with 4.5 m. The segments are PM-based (NdFeB), in which the gap is 12 mm, the period is 27.3 mm, and the on-axis peak magnetic field is 0.48 T ($K = 1.23$). A test undulator was produced with the same structure of the segments, but only with 3 poles. It is placed on the US side of the undulator hall to track radiation exposure and demagnetization effects. TLDs sensors are read every week to check radiation exposure, and the test undulator is regularly removed for magnetic field inspection. Figure 2.6d shows the field degradation level in each pole *versus* the accumulated doses between 2004 and 2007. A degradation level of -5×10^{-4} /kGy was found for the worst case (middle pole) [8].

2.7.4 SACLA

The **S**Pring-8 **A**ngstrom **C**ompact Free Electron **La**ser (SACLA, Hyogo, Japan) started operating in 2011. Being the second hard X-ray FEL in the world (only behind LCLS) and the first in Japan, its beamline accommodates 18 hybrid undulators made of NdFeB. Every undulator has 18 mm of magnetic period and on-axis peak field of 1.3 T ($K = 2.2$).

In 2016, SACLA reported a substantial flux loss observed in permanent magnets in the first segment [9]. Figure 2.6e shows the peak field deviation for the first 8 segments between measurements performed in 2012 and 2015. Since the most aggressive loss of field strength occurred in the US end of the first segment (over 35%), the scale of the top and bottom figures are different.

2.7.5 Eu.XFEL

The **Eu**ropean **XFEL** (Eu.XFEL, Hamburg, Germany) is composed of three SASE undulator systems (named SASE1, SASE2, and SASE3), each one with a few dozens of 5-m long NdFeB hybrid undulators. A diagnostic undulator (DU) is placed at the entrance of each SASE system. The DU has the same magnetic structure of the SASE1 5-m long undulator. It has 8 poles, period length of 40 mm, and peak field of 0.916 T ($K = 3.28$). Figure 2.6f presents the relative field reduction for each pole of the SASE3 DU after radiation doses of 4.4 kGy. For Pole 3 to Pole 6, Fig. 2.6g shows the field degradation level *versus* exposure for SASE1 and SASE3 DUs. In addition, after an absorbed dose of 230 Gy, the Segment 3 of SASE 1 showed a change of the magnetic field by 0.05% for the first 4 poles and degradation of the first field integral up to 37 µTm [10].

2.7.6 LCLS

The **L**inac **C**oherent **L**ight **S**ource (LCLS, Menlo Park, California, USA) is the world's first hard X-ray Free Electron Laser. Located at the SLAC National Accelerator Laboratory, it started operating in 2009. The LCLS generates ultra-short X-ray beams with fixed gap hybrid NdFeB undulators [43].

Figure 2.6h shows the relative change of the peak field measured in 2009 and 2014 for the Segment 30, which resulted in $(-2.5 \pm 0.5) \times 10^{-4}$ [11]. TLDs have recorded radiation doses, and a reduction of $\Delta K/K$ has been observed. Figure 2.6i presents the relative change of K-parameter *versus* the accumulated doses between 2009 and 2014. The data points correspond to the average of $\Delta K/K$ for all the measured segments.

2.8 Techniques for Measuring K-parameter After Tunnel Installation

FELs using the SASE principle require long undulator systems, commonly varying from 30 m (e.g., FLASH) to 220 m (e.g., Eu.XFEL). Thus, the undulator system is usually composed of dozens of segments. Over all undulators, the individual K-parameter must match withing tight tolerances, so every undulator correctly adds to the radiation wave at the same wavelength. Because of that, the undulators' magnetic field is tuned before tunnel installation in a dedicated magnetic measurement laboratory. As briefly mentioned in Chapter 1, measuring the field's quality after installation becomes quite challenging. In most cases, setting up conventional techniques (e.g., Hall probes, flip coils, and stretched wire systems) in the tunnel is difficult due to the dense packing of accelerator components and the number of segments.

Studies have proposed techniques to measure K-parameter changes after the installation of the undulator in the tunnel based on spectral features of radiation. Hence, K is calculated from the relationship among the parameters shown in (2.45), by accurately measuring the radiation wavelength λ, the angle of observation θ, and the electron energy (related to γ). In November of 2005, the LCLS Beam-Based Undulator K Measurement Workshop took place at SLAC [44]. One of the main ideas had been presented in the 2005 Particle Accelerator Conference [24]. B. Yang explored the radiation features emitted from undulators based on numerical simulations. It was shown that:

(i) the slope in the photon flux obtained from angle-integrated undulator radiation *versus* photon energy is sensitive to K-parameter on the high-energy edge, which has a great potential to be used to measure K for single undulators; and

(ii) by setting up a standard and test undulator in such a way that the intensity of the radiation by each one reaches the same monochromator separately, the signal difference will be directly related to the difference of magnetic field of the two undulators and, therefore, to the K-value difference between them.

J. Welch *et al.* presented in 2006 shows how the slope in the photon flux could be used

to check two adjacent undulators, given that different values of K between them would also reduce the slope of photon flux *versus* photon energy on the high-energy spectrum edge, depending on the relative difference [25]. The same author presented in 2009 the first *in situ* measurements of relative undulator segment K-parameters using a monochromator [26]. The technique was based on single-undulators measurement, slightly different from the method proposed and described in [25] and [24].

First, the photon flux is measured from a reference undulator placed in its standard position for different electron beam energies, while all the other segments are remotely moved off from the beamline. Then, the reference undulator is removed, and the test undulator starts lasing. The sweeping in energy is measured again, but also for different horizontal positions. The energy at which the slope is maximum is plotted as a function of horizontal position and a second-order polynomial is fitted to the data. The horizontal position in which the fitted curve crosses the maximum slope energy of the reference undulator defines its horizontal position. A reproducibility of 4×10^{-4} for $\Delta K/K$ was achieved. The dependence of K-value with the horizontal position relies on a conceptual design called *canted undulators* [45].

Recently, the testing results with a K-monochromator in the Eu.XFEL undulator were reported [27]. In simple terms, the off-axis spectrum is characterized for a specific undulator. The angle of observation θ depends on the distance from the undulator to the detector and the measured ring diameter. Taking into account the electron beam energy and the undulator's period, the undulator equation [see (2.45)] permits to calculate the K-parameter. The authors measured K-value below the limit 3×10^{-4} — the specified tolerance for K-value variation from segment to segment for the Eu.XFEL.

Even though encouraging results have been reported regarding beam-based K measurements, the precision of these techniques is limited to the uncertainties of electron beam energy and observation angle. Besides, full access to the control and data acquisition systems is required. An obvious way to keep checking undulators' field quality is to remove and replace segments from the tunnel for inspection periodically. However, as briefly mentioned in Chapter 1, taking segments out of the tunnel brings several inconveniences as a consequence of sizes, weight, and vacuum venting considerations.

As highlighted in Subsection 2.7.6, small levels of field changes have been observed in

the LCLS-I. Nevertheless, its low repetition rate (120 bunches per second with up to 0.25 nC bunch charge [46]) and the ability to straightforwardly remove, remeasure, and retune (when required) the segments have made radiation damage a low-risk issue. High-repetition rate facilities, such as the Eu.XFEL (up to 27 000 bunches per second with nominal bunch charge of 1 nC [47]) and the upcoming LCLS-II (1 million bunches per second with up to 0.1 nC bunch charge [29]), makes periodic removal much more complicated because of the higher radiation exposure.

2.9 The New LCLS-II

After the first lasing in 2009, LCLS-I proved to be a powerful tool to perform advanced research in chemistry, materials, biology, and energy [1]. SLAC has been planning an upgrade of the LCLS-I [49, 50]. One of the major improvements in terms of the capability of the new LCLS-II will be photon beam repetition rate — moving from the current 120 Hz to 1 MHz. A superconducting radiofrequency accelerator will provide beams up to 4 GeV. Two variable-gap undulator systems will produce soft X-rays (SXR) from 200 eV to 5 keV and hard X-rays

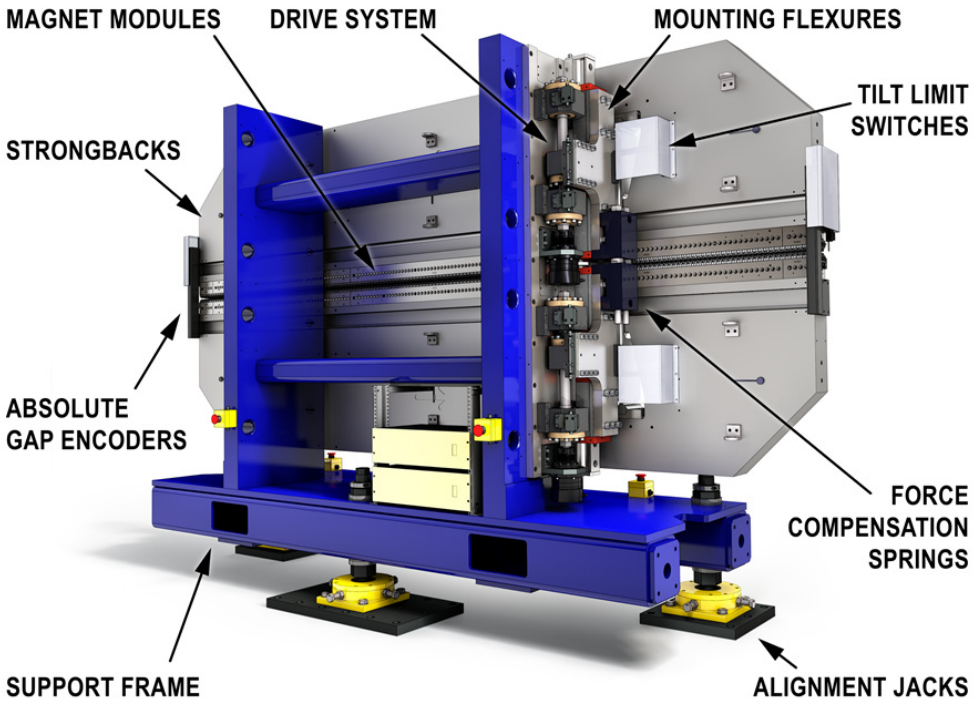

Figure 2.7: LCLS-II soft X-ray (SXR) segment [48].

(HXR) 200 eV to 25 keV [29]. The SXR undulator line will be composed of 21 segments with period of 39 mm, while the HXR undulator line will have 32 segments with period of 26 mm. Figures 2.7 and 2.8 show the segment of the SXR and HXR lines, respectively. All the undulators are 3.4-m long PM-based (NdFeB) hybrid undulators [51]. Figure 2.9 illustrates the LCLS-II beamlines. The main parameters of both SXR and HXR undulator halls are shown in Table 2.1.

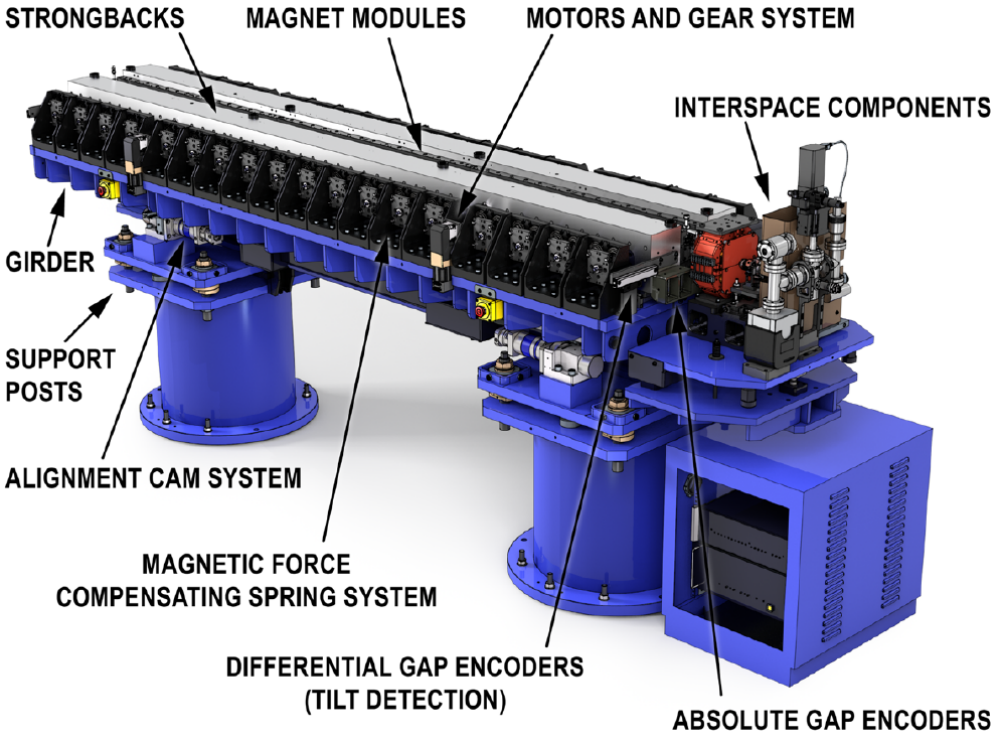

Figure 2.8: LCLS-II hard X-ray (HXR) segment [48].

In the LCLS-I, TLDs have detected radiation levels about 100 mGy/week at 120 Hz beam operation with 0.25 nC bunch charge. Because of the high repetition rate designed for the LCLS-II, we may expect up to 1000 times more electrons per second. To mitigate the radiation damage effects, protective monitoring systems that have been used in LCLS-I will be set in LCLS-II, including a complete collimator system upstream of the final bends in the linac-to-undulator section and a machine protection system that prevents beam operation with trajectory outside a ± 1 mm limit or at high radiation doses [52].

The tolerance budget $\Delta K_{\text{eff}}/K_{\text{eff}}$ and field integrals shown in Table 2.1 are obtained from simulations of the FEL process, being required for individual segments. It is worth evaluating

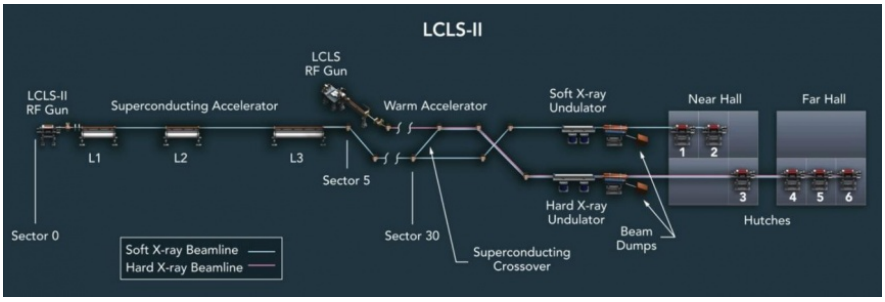

Figure 2.9: Schematic of the LCLS-II beamlines [29].

Table 2.1: LCLS-II undulator parameters.

Parameter	SXR	HXR
Max. electron beam energy (GeV)	4	4
Number of segments	21	32
Individual segment length (m)	3.4	3.4
Number of poles per segment	174	260
Period length (mm)	39	26
Min. operational magnetic gap (mm)	7.2	7.2
Max. operational magnetic gap (mm)	22	20
B_{eff} at min. operational gap (T)	1.49	1.01
K_{eff} at min. operational gap	5.43	2.44
$\Delta K_{\text{eff}}/K_{\text{eff}}$	$\pm 3.0 \times 10^{-4}$	$\pm 2.3 \times 10^{-4}$
First field integral of B_y and B_x (µTm)	< 40	< 40
Second field integral of B_y and B_x (µTm^2)	< 150	< 150
Undulator type	Planar	Planar
Undulator magnet type	PM Hybrid	PM Hybrid
Gap type	Variable	Variable
Magnet material	$Nd_2Fe_{14}B$	$Nd_2Fe_{14}B$
Pole material	Vanadium Permendur	Vanadium Permendur

the field integral equations numerically to provide an idea on how tight those specifications are. From the electron energy of 4 GeV, $\gamma = 7828$ [see (2.3)]. Approximating v_z and c, $e/(\gamma m_e v_z) = 0.075\,(\text{Tm})^{-1}$. Given the tolerance for $I_{1x,1y}$ and $I_{2x,2y}$ shown in Table 2.1, the maximum kick and the end position of the electron beam for each undulator are 3 µrad $[0.075\,(\text{Tm})^{-1} \times 40\,\mu\text{Tm}]$ and 11 µm $[0.075\,(\text{Tm})^{-1} \times 150\,\mu\text{Tm}^2]$, respectively.

Based on the limit of $\Delta K_{\text{eff}}/K_{\text{eff}}$ for the SXR and HXR undulators, the resolution of 0.01% (10^{-4}) specified in Chapter 1 represents an appropriate starting point for an *in situ* diagnostic system, as will be presented in details in the next chapter.

Chapter 3

In-Situ Radiation Damage Detection System for Undulators

HAVING explored the basis of permanent magnet undulators, the issues regarding demagnetization due to absorbed doses and the challenges for the undulator system of the new LCLS-II, we will now proceed in presenting a novel approach for monitoring magnetic field quality of segments without taking them out of the tunnel. This chapter begins by presenting the system's principles and theoretical performance. Then, software and hardware developments, results of short-term tests, long-term tests, and analysis are presented. This work was conducted for the undulators of the LCLS-II. At the time this project began, only the SXR undulators control system was fully commissioned at SLAC. Thus, the sensor layout and other details of the proposed approach were developed for SXR segments[1].

3.1 System Principles

The principle of the proposed RDDS is to measure the flux change in a flexible printed-circuit coil with many segments installed in an undulator. By changing the undulator's gap, a voltage is induced in the coil. The electrical connection between adjacent segments must guarantee that the opposite polarity of the field does not cancel the signal. Figure 3.1 presents the schematic of the measurement system with the coil placed on the surface of the lower array.

[1]This chapter is an amended version of the following manuscript: J. E. Baader, S. D. Anderson, and Z. R. Wolf, "A novel in-situ radiation damage diagnostic system for undulators," *IEEE Transactions on Instrumentation and Measurement*, in press, doi: 10.1109/TIM.2019.2936715.

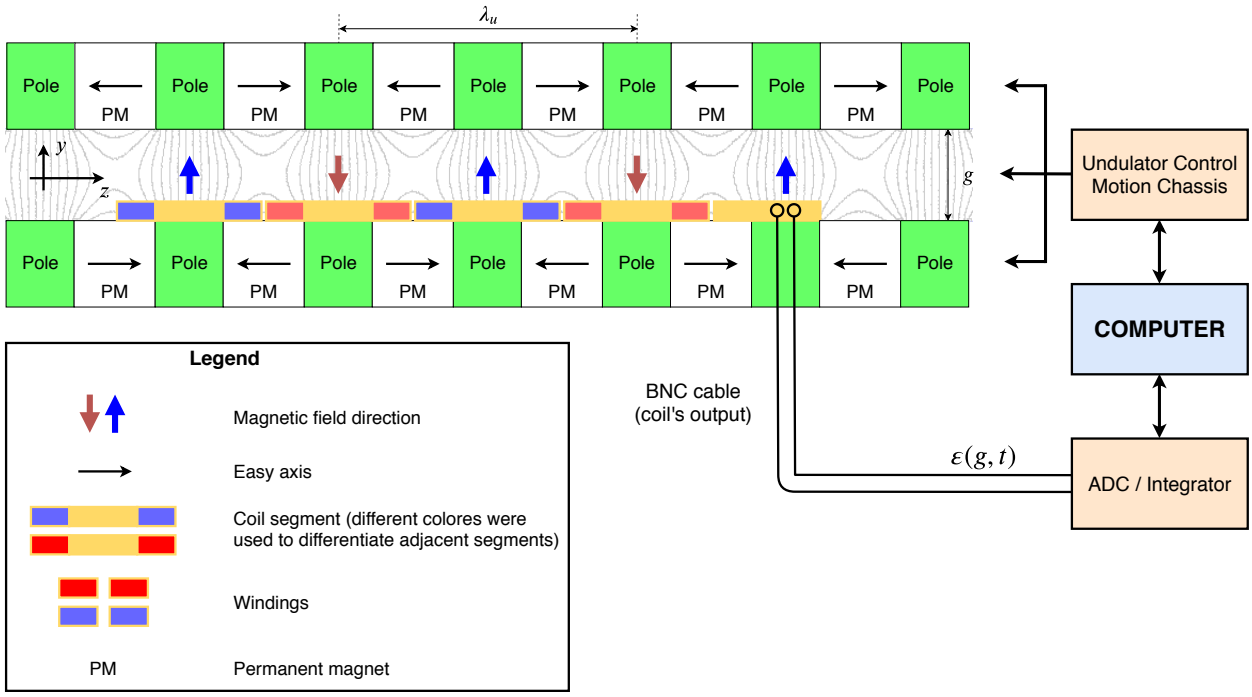

Figure 3.1: Schematic of the system for measuring flux change in hybrid undulators during operation. ©2019 IEEE [53].

The magnetic field $\vec{B}$ within the free space of the undulator must satisfy Maxwell's equations in the static regime (e.g., $\nabla \cdot \vec{B} = 0$ and $\nabla \times \vec{B} = 0$). Since both the divergence and curl are zero, the magnetic field can be expressed as $\vec{B} = -\nabla\Phi$, where Φ is a scalar potential that satisfies Laplace's equation $\nabla^2\Phi = 0$. The solution

$$\Phi = -\frac{\hat{B}}{k_y}\cosh(k_x x)\sinh(k_y y)\cos(k_u z) \tag{3.1}$$

satisfies the Laplace's equation and the boundary conditions, as explained in details in Appendix D. In (3.1), k_x, k_y and k_u are wave numbers (given in rad/m), and $k_u = 2\pi/\lambda_u$. From $\vec{B} = -\nabla\Phi$,

$$B_x = \frac{k_x\hat{B}}{k_y}\sinh(k_x x)\sinh(k_y y)\cos(k_u z) \tag{3.2}$$

$$B_y = \hat{B}\cosh(k_x x)\cosh(k_y y)\cos(k_u z) \tag{3.3}$$

$$B_z = -\frac{k_u \hat{B}}{k_y} \cosh(k_x x) \sinh(k_y y) \sin(k_u z), \tag{3.4}$$

where

$$k_u^2 = k_x^2 + k_y^2. \tag{3.5}$$

Equation (3.1) shows that for any arbitrarily chosen z position, the magnetic field equipotential curvature (where the field is perpendicular) obeys $\cosh(k_x x)\sinh(k_y y) = \text{constant}$. For instance, $k_x = 0$ makes the field independent of x because $\cosh(k_x x) = 1$ for any x. In this case and given k_y, the equipotential line corresponds to y constant along the x-axis. Due to the high permeability of the poles, the field is practically perpendicular to them. Therefore, the equipotential surface can be used to define the pole face profile, which for $k_x = 0$ would be a plane, infinite in x and limited in z according to k_u (i.e., the undulator period). It should be noticed that k_x, k_y and k_u define the undulator poles geometry, while $\hat{B}$ is primarily dependent on the magnetic features of the materials (that is, iron properties, PM remanent field, material quality, etc.).

Let B_{LA} be the maximum field on the pole p of the lower array. By combining (3.3) and (2.46) for $\cos(k_u z) = 1$ and $y = -g/2$ (where the surface of the lower array is located),

$$B_{LA}(g,p) = B_0(p) \exp\left[a\left(\frac{g}{\lambda_u}\right) + b\left(\frac{g}{\lambda_u}\right)^2\right] \cosh(k_x x) \cosh\left(-k_y \frac{g}{2}\right). \tag{3.6}$$

Our analyzes is limited to the region of the poles, where the field is approximately constant along x axis. If the field does not depend on x, then we can set $k_x = 0$, as aforementioned. From (3.5), $k_y = k_z = 2\pi/\lambda_u$. With those assumptions,

$$B_{LA}(g,p) = B_0(p) \exp\left[a\left(\frac{g}{\lambda_u}\right) + b\left(\frac{g}{\lambda_u}\right)^2\right] \cosh\left(\frac{\pi g}{\lambda_u}\right). \tag{3.7}$$

To simplify the notation,

$$B_{LA}(g,p) = B_0(p)\eta(g), \tag{3.8}$$

where

$$\eta(g) = \exp\left[a\left(\frac{g}{\lambda_u}\right) + b\left(\frac{g}{\lambda_u}\right)^2\right]\cosh\left(\frac{\pi g}{\lambda_u}\right). \tag{3.9}$$

The magnetic flux in the p-th segment, given by

$$\phi_s(g,p) = \iint_S B_y(y=-g/2)\,\mathrm{d}x\,\mathrm{d}z, \tag{3.10}$$

may be express in terms of the field calculated by (3.7) passing through the effective area of one coil segment, k_s, or

$$\phi_s(g,p) = k_s B_{LA} = k_s B_0(p)\eta(g). \tag{3.11}$$

The term k_s (given in area units) is a constant associated with the coil's features, such as dimensions, number of turns per coil segment, and position in the undulator[2]. An equation to estimate the value of k_s is presented in Section 3.2. If the coil has N_s segments and the windings direction guarantees that the signal sums up, then the total flux is

$$\phi(g,p_0) = \sum_{p=p_0}^{N_s+p_0-1}\phi_s(p) = k_s\eta(g)\sum_{p=p_0}^{N_s+p_0-1}B_0(p), \tag{3.12}$$

where p_0 is the number of the first pole covered by the coil.

According to Faraday's law, the voltage ε induced in the coil when the undulator gap changes is

$$\varepsilon(t) = -\frac{\mathrm{d}\phi}{\mathrm{d}t}. \tag{3.13}$$

Integrating (3.13) from t_1 to t_2,

$$\psi = \int_{t_1}^{t_2}\varepsilon\,\mathrm{d}t = -\phi(t_2) + \phi(t_1) = \phi_1 - \phi_2, \tag{3.14}$$

where t_1 and t_2 are the times when the gap is g_1 and g_2, respectively, and the corresponding magnetic fluxes are ϕ_1 and ϕ_2. Combining (3.14) and (3.11), the integrated voltage induced in the coil when the undulator gap changes from g_1 to g_2 is given by

[2]Reference [28] uses a parameter named *coil sensitivity* (κ) to link magnetic flux and magnetic field, being equivalent to our definition of "effective area". The term "sensitivity" will be used in this thesis to refer to the "local sensitivity" of the RDDS (see Section 3.9). Thus, we will designate k_s and related variables as "effective area".

$$\psi(g_1, g_2) = k_s[\eta(g_1) - \eta(g_2)] \sum_{p=p_0}^{N_s+p_0-1} B_0(p). \tag{3.15}$$

Multiplying and dividing by N_s,

$$\psi(g_1, g_2) = N_s k_s[\eta(g_1) - \eta(g_2)] \frac{1}{N_s} \sum_{p=p_0}^{N_s+p_0-1} B_0(p), \tag{3.16}$$

or simply

$$\psi(g_1, \Delta g) = k_c \overline{B_0}[\eta(g_1) - \eta(g_1 + \Delta g)], \tag{3.17}$$

where

$$k_c = N_s k_s \tag{3.18}$$

is the total effective area of the coil, $\Delta g = g_2 - g_1$ is the gap change, and $\overline{B_0}$ is the average of $B_0(p)$ for all the poles covered by the coil.

Equation (3.17) shows that if the magnet strength changes due to radiation damage (i.e., if $\overline{B_0}$ drops), then ψ decreases proportionally. This fact demonstrates that field variation can be measured by the change of the integrated voltage. The main advantage of integrating the induced signal is that ψ depends on the magnetic flux when the undulator gap is g_1 and g_2, being independent of the gap movement profile. Besides, integrating the signal reduces the influence of electrical noise.

The higher the effective area of the coil, the higher the induced voltage [see (3.12) and (3.13)]. Therefore, increasing the first improves the signal-to-noise ratio. The section that follows aims to define a model of the effective area of the coil as a function of its features and the magnet array's geometry.

3.2 Mathematical Model of the Effective Area

Figure 3.2 illustrates the top view of a few segments of the coil. Each coil segment has N_w windings per layer. When the coil is placed on the undulator magnet array, the windings of each segment are wrapped around the pole.

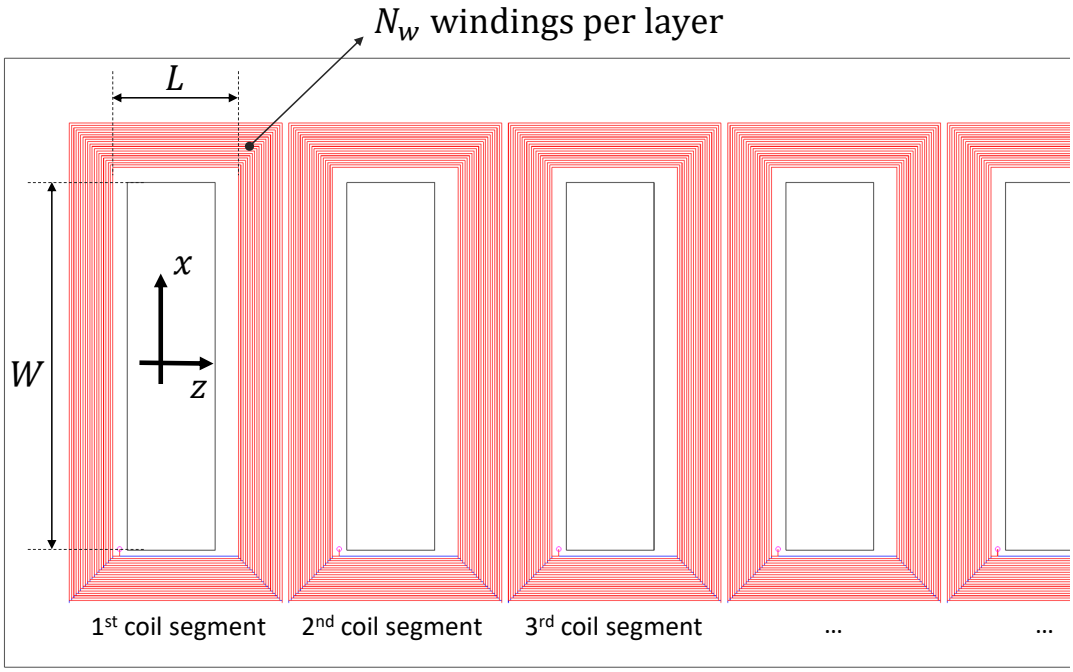

Figure 3.2: Sketch of the top view of the coil and main dimensions.

Adjacent poles have opposite field polarity. Above the permanent magnets, the field is, in theory, null, as illustrated in Fig. 3.3. Assuming a sinusoidal variation of the field along the surface of the array in z direction, the magnetic flux concatenated with a coil segment placed on the lower array of the undulator (see Fig. 3.3) is

$$\phi_s = \phi_p + \phi_w, \tag{3.19}$$

where ϕ_p is the flux linked in the region above the pole ($-L/2 \leq z \leq +L/2$) and ϕ_w is the flux through the windings region. If the coil segment has n_L layers of windings (total of $n_L N_w$ windings per segment), then

$$\phi_p = n_L N_w \int_{-W/2}^{W/2} \int_{-L/2}^{L/2} B_{LA} \cos\left(\frac{2\pi z}{\lambda_u}\right) \mathrm{d}x \, \mathrm{d}z, \tag{3.20}$$

where L is the inner length of the segment (not necessarily equal to the pole length), W is the width of the pole that is covered by the inner winding (we assumed that the field does not depend upon x-axis), x is the horizontal axis, and z is the longitudinal axis. Solving (3.20), we find

$$\phi_p = \frac{n_L N_w \lambda_u W B_{LA}}{\pi} \sin\left(\frac{\pi L}{\lambda_u}\right). \tag{3.21}$$

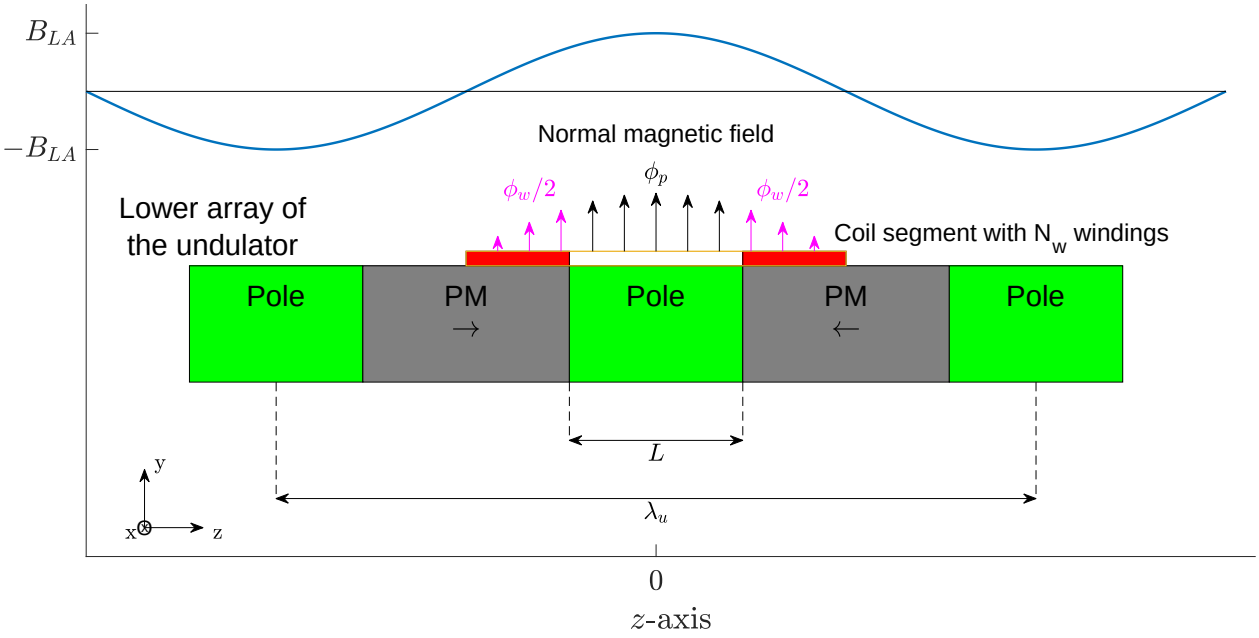

Figure 3.3: Position of the coil on the lower array of a hybrid undulator and field profile. ©2019 IEEE [53].

Let ΔL be the distance between adjacent windings. The 1st winding (or group of stacked wires if there is more than one layer) is located at $z = L/2$, the 2nd at $z = L/2 \pm \Delta L$, the 3rd at $z = L/2 \pm 2\Delta L$, the 4th at $z = L/2 \pm 3\Delta L$, and so on. We may consider that the field between two adjacent windings is constant and equivalent to the field in the middle of them. Then, the magnetic flux linked between the 1st and 2nd windings is

$$\varphi_1 = 2n_L(N_w - 1)B_{LA}W\Delta L \cos\left[\frac{2\pi(L/2 + 1\Delta L - \Delta L/2)}{\lambda_u}\right]. \tag{3.22}$$

Between the 2nd and 3rd winding,

$$\varphi_2 = 2n_L(N_w - 2)B_{LA}W\Delta L \cos\left[\frac{2\pi(L/2 + 2\Delta L - \Delta L/2)}{\lambda_u}\right]. \tag{3.23}$$

Between the the 3rd and 4th,

$$\varphi_3 = 2n_L(N_w - 3)B_{LA}W\Delta L \cos\left[\frac{2\pi(L/2 + 3\Delta L - \Delta L/2)}{\lambda_u}\right]. \tag{3.24}$$

Following the same rule, the magnetic flux linked between the (N_w-1)-th and N_w-th winding (the last two) is

$$\varphi_{N_w-1} = 2n_L(1)B_{LA}W\Delta L\cos\left[\frac{2\pi(L/2+(N_w-1)\Delta L-\Delta L/2)}{\lambda_u}\right]. \tag{3.25}$$

The total flux through the windings is

$$\phi_w = \sum_{i=1}^{N_w-1}\varphi_i = 2n_L B_{LA}W\Delta L\sum_{i=1}^{N_w-1}(N_w-i)\cos\left[\frac{2\pi(L/2+i\Delta L-\Delta L/2)}{\lambda_u}\right]. \tag{3.26}$$

Adding (3.21) and (3.26), the total magnetic flux linked with the coil segment is

$$\begin{aligned}\phi_s =&\phi_p+\phi_w = \frac{n_L N_w\lambda_u B_{LA}W}{\pi}\sin\left(\frac{\pi L}{\lambda_u}\right)\\ &+2n_L B_{LA}W\Delta L\sum_{i=1}^{N_w-1}(N_w-i)\cos\left[\frac{2\pi(L/2+i\Delta L-\Delta L/2)}{\lambda_u}\right].\end{aligned} \tag{3.27}$$

From (3.11), $k_s = \phi_s/B_{LA}$. If N_s coil segments are connected in series and the windings direction alternates from pole to pole, then, according to (3.18),

$$\begin{aligned}k_c =&N_s k_s = n_L N_s W\left[\frac{N_w\lambda_u}{\pi}\sin\left(\frac{\pi L}{\lambda_u}\right)\right.\\ &\left.+2\Delta L\sum_{i=1}^{N_w-1}(N_w-i)\cos\left(\frac{i2\pi\Delta L+\pi L-\pi\Delta L}{\lambda_u}\right)\right].\end{aligned} \tag{3.28}$$

Consider that the coil is designed to optimize the concatenated flux — i.e., the coil's geometry matches with the pole's dimensions, the region of the windings covers half of the surface of each adjacent permanent magnet [see the red area of the coil in Fig. 3.3], and the center of the coil coincides with the center of the pole. Equation (3.17) gives the signal's strength as a function of the coil's and undulator's features. By knowing the magnet array's geometry (W, L, and λ_u) and the parameters that define the on-axis peak field as a function of the gap (a, b, and $\overline{B_0}$), one may define the number of layers, segments, and windings of the coil according to: 1) the available manufacturing technology; 2) the undulator constraints (e.g., minimum gap, gap velocity, gap positioning repeatability, etc.); and 3) the readable strength for ψ based on the available voltmeters and integrators. Section 3.7 presents the

model validation based on numerical evaluation of (3.28) and measurements with the coil and Hall probe.

3.3 Detectable Changes in Pole Strength

For a moment, let us assume that $B_0(p)$ is constant over the whole length of the undulator, which makes K proportional to $\overline{B_0}$ ($\Delta K/K = \Delta\overline{B_0}/\overline{B_0}$). From the tolerance of ΔK_{eff} (see Table 2.1), a system capable of detecting relative ψ changes better than 10^{-4} designates a reasonable aim. It means that the system would be capable of detecting relative changes on $\overline{B_0}$ better than 10^{-4}. Because of the gap-dependence of ψ expressed in (3.17), such resolution requires gap positioning repeatability in less than a micrometer.

Let $\Delta\psi$ be the change on the integrated voltage (flux change) as the consequence of field strength variation in the poles, represented as $\Delta B_0(p)$. From (3.16),

$$\Delta\psi = N_s k_s[\eta(g_1) - \eta(g_2)]\frac{1}{N_s}\sum_{p=p_0}^{N_s+p_0-1}\Delta B_0(p). \tag{3.29}$$

Dividing both sides of (3.29) by (3.17),

$$\frac{\Delta\psi}{\psi} = \frac{1}{N_s}\sum_{p=p_0}^{N_s+p_0-1}\frac{\Delta B_0(p)}{\overline{B_0}}. \tag{3.30}$$

Therefore, given the minimum detectable signal $(\Delta\psi/\psi)_{\text{det}}$ and the number of coil segments N_s, the relative changes in the pole strength covered by the coil must satisfy

$$\left|\sum_{p=p_0}^{N_s+p_0-1}\frac{\Delta B_0(p)}{\overline{B_0}}\right| \geq N_s\left|\left(\frac{\Delta\psi}{\psi}\right)_{\text{det}}\right|. \tag{3.31}$$

Most of the results presented in Section 2.7 show that field degradation occur in a fraction of the whole undulator length, which justifies the design of a flexible coil that covers only a few dozens of poles. Given that the SXR undulator has 174 poles, the flexible coil was developed with 30 winding segments. Its layout will be presented in Section 3.5. For $N_s = 30$ and $(\Delta\psi/\psi)_{\text{det}} = 10^{-4}$,

$$\left|\sum_{p=p_0}^{N_s+p_0-1}\frac{\Delta B_0(p)}{\overline{B_0}}\right| \geq 3\times 10^{-3}. \tag{3.32}$$

Section 2.4 explained how to calculate K_{eff} for an actual undulator considering that its poles may have different field amplitudes. The next section will analyze how a field change at some particular places in the undulator would affect K_{eff} considering the minimum detectable field changes expressed in (3.32).

3.4 Simulations

Equation (3.32) establishes the constraint in field change to guarantee that the system detects the change. We now wish to evaluate how different scenarios of field change affect K_{eff}. Although the representation of demagnetization due to radiation damage is not straightforward — as one can observe in Fig. 2.6 — simulations allow pre-evaluating system's performance.

A Matlab program allows estimating K_{eff} by using the equations presented in Section 2.4. The parameters used for the simulations are presented in Table 3.1. Notice that many parameters come from the SXR features in Table 2.1. The undulator end design was not relevant here, and it was not taken into account for these analyses.

Table 3.1: Simulation parameters based on SXR undulator features.

Parameter	Symbol	Values
Electron beam energy (GeV)	E	4
Lorentz factor	γ	7828
Undulator period (mm)	λ_u	39
Number of poles	N_p	174
K-parameter (specified)	K or K_{spec}	5.43
Nominal on-axis peak field (T)	$\hat{B}$	1.49
Sample spacing (µm)		1.5

First, the code calculates the amplitude of the vertical magnetic field as a function of K by isolating $\hat{B}$ in (2.35). The components B_x and B_z are not considered. Changes in the amplitude of specific poles can be performed manually, according to the desired test. The results of the algorithm are shown in Figs. 3.4 through 3.9 for different scenarios. In each, the magnetic field over the longitudinal axis and its relative change for each pole number are shown in the upper left and right of the figure, respectively. Given $B_y(z)$ and the parameters shown in Table 3.1, the program applies (2.14) and (2.16) to calculate the slope $\dot{x}(z)$ and the

trajectory $x(z)$, which are depicted in the middle left and right of the figures, respectively. The slippage, presented in the bottom left of the figures, is calculated from (2.37), with Ω_{fit} being computed from the fitted line and K_{eff} by applying (2.41). At the bottom right, the figures present the values of the main input and output parameters, including $\Delta K_{\text{eff}}/K_{\text{eff}}$.

One way to ensure that the program works correctly is by simulating the case in which the field behaves as a pure sinusoidal (i.e., with no errors). For this ideal scenario, there should be no difference between the specified K and calculated K_{eff}. In fact, this condition is met for no field errors, as shown in Fig. 3.4.

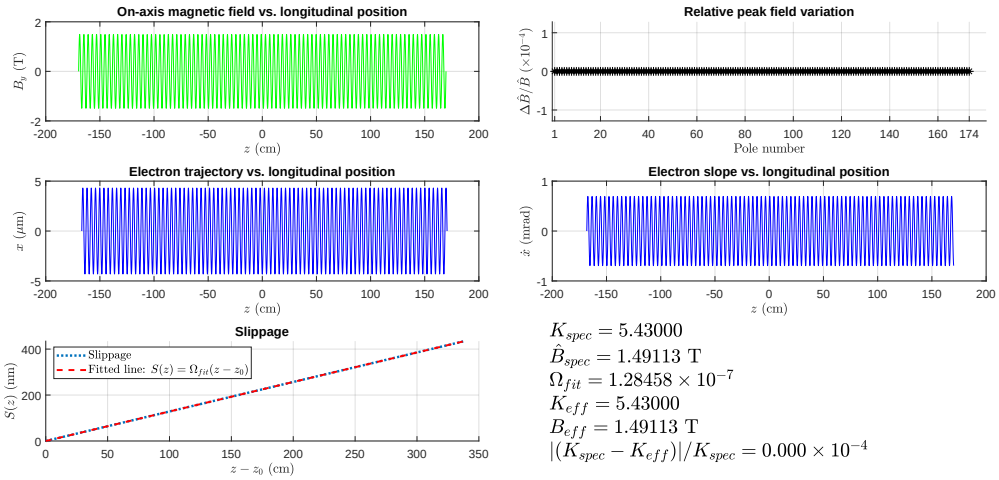

Figure 3.4: Simulation and K_{eff} calculation for a sinusoidal field with no errors.

Two situations that are not related to radiation damage may cause every pole to change the field by roughly the same amount: temperature changes and gap error. If every pole changes its strength by -10^{-4}, then (3.32) would be satisfied independently of the coil's position in the undulator. Besides, it would be expected that K_{eff} changes -10^{-4} as well, because the field in the undulator decreases proportionally along its whole length [see (2.36)]. Indeed, this relative change is confirmed in the results presented in Fig. 3.5, which reinforces the programs' validity once again.

We may now analyze how K_{eff} changes when a single pole strength decreases. First, consider that only the first pole had its strength decreased by 3×10^{-3} [(3.32) is satisfied]. As shown in Fig. 3.6, K_{eff} changed by 3.56×10^{-5}. This scenario also highlights how a small change in one of the pole's strength behaves as a small dipole, as depicted in the electron trajectory. Changing the strength of a single pole in the middle of the undulator (Pole #87)

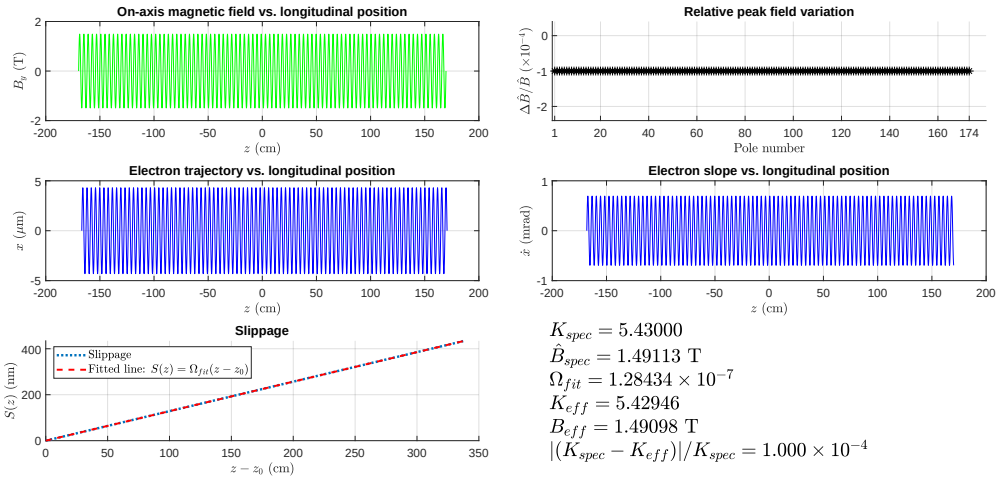

Figure 3.5: Simulation and K_{eff} calculation considering that all the undulator poles strength decrease by 0.01%.

by 3×10^{-3}, K_{eff} changed less than the previous case, as presented in Fig. 3.7. Indeed, decreasing the field of the poles one-by-one revealed that the maximum change in K_{eff} occurs when the first pole has its field altered.

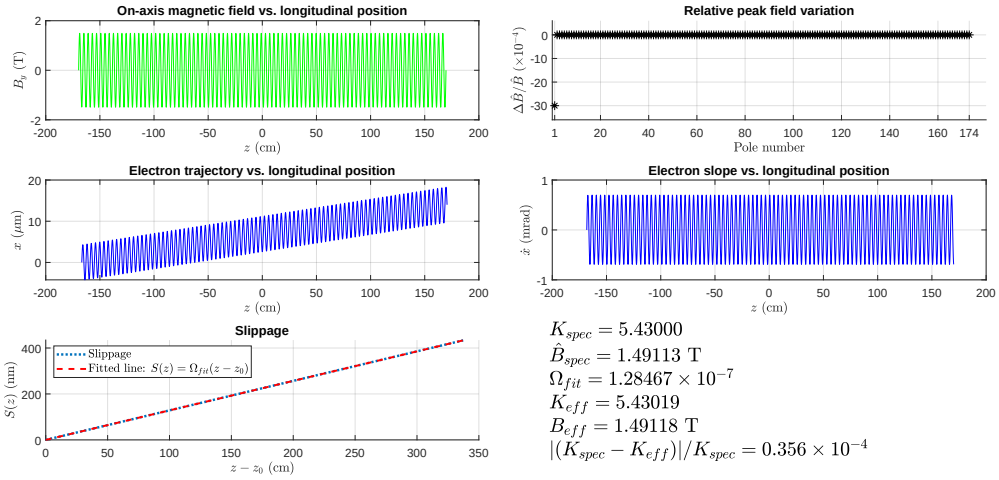

Figure 3.6: Simulation and K_{eff} calculation considering that Pole #1 (US end) strength decreases by 0.3%.

The flexible coil acts as a magnetic field change sensor that monitors a limited number of poles in the undulator. As mentioned in Section 3.3, the coil that will be presented in this thesis covers 30 poles of the SXR undulator. Therefore, it is worthwhile to evaluate the changes in K_{eff} when the strength of the poles covered by the coil decreases with respect to the desired amplitude.

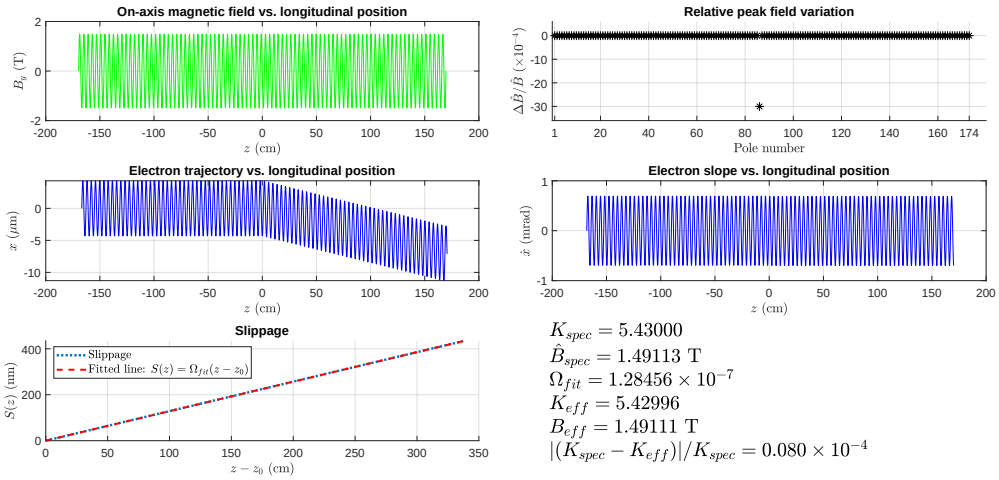

Figure 3.7: Simulation and K_{eff} calculation considering that Pole #87 (middle) strength decreases by 0.3%.

Let us assume that the coil is placed at the US end of the undulator, in such a way that its length covers Pole #1 through Pole #30. Only these 30 poles covered by the coil's length have their strengths decreased by 10^{-4}, so (3.32) is satisfied. As depicted in Fig. 3.8, K_{eff} changed less than 10^{-5} for this case. Besides, the electron trajectory was not considerably affected since 30 poles correspond to 15 pairs of poles canceling each other's deflections. The higher $\Delta K_{\text{eff}}/K_{\text{eff}}$ occurred when Pole #72 through Pole #101 (assume that the coil covers these 30 poles) had theirs strength reduced by 10^{-4}, which resulted in a relative change in K_{eff} that corresponds to approximately a quarter of the detectable ψ change. Figure 3.9 shows this case.

After analyzing the effect of a constant change over the 30 poles covered by the coil, we may also consider modeling the linear-changing tendency of field degradation along the undulator length. One might notice that an approximate linear pattern of field change along the poles is present in some of the plots shown in Fig. 2.6[3].

Figure 3.10 represents the results obtained with the code when the field degradation of the first 30 poles changes linearly from -2×10^{-4} (for Pole #1) to 0 (for Pole #1), which satisfies (3.32).

By testing the same profile of field variation (i.e., 30 poles with their strength changing

[3]See, for instance, the approximate linear change with respect to the distance along the undulator length in figures 2.6a, 2.6b, 2.6c, and 2.6e.

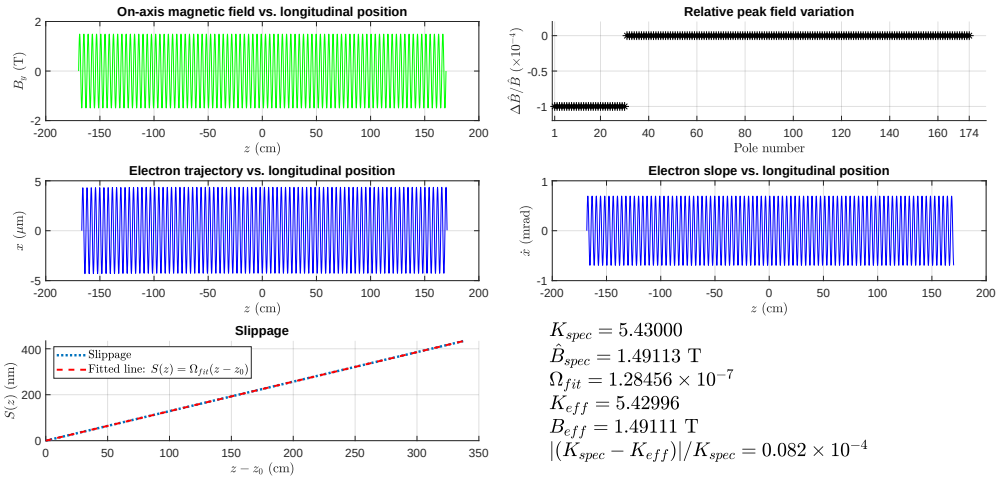

Figure 3.8: Simulation and K_{eff} calculation considering that the field decreases by 0.01% per pole over the coil's length from Pole #1 to Pole #30 (US end).

linearly from -2×10^{-4} to 0) for all possible cases within the undulator length, the scenario that the relative K_{eff} changed the most was for the degradation between Pole #78 to Pole #107, being 2.57×10^{-5}. Figure 3.11 depicts the results.

Although not necessarily realistic, we used simulations to test a few "extreme" scenarios considering the minimum detectable field change defined for the system. Such cases indicate that the relative resolution of 10^{-4} for ψ is appropriate for sensing K_{eff}: The worst case in terms of field degradation sensed by the coil corresponded to a relative change of 3.56×10^{-5} in K_{eff} (well below the tolerance). Nevertheless, it should be noted that a straightforward

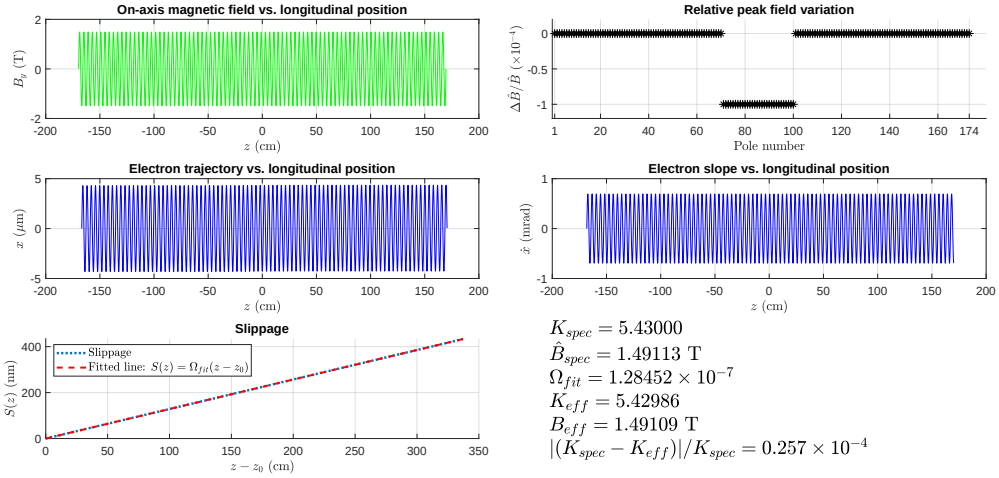

Figure 3.9: Simulation and K_{eff} calculation considering that the field decreases by 0.01% per pole over the coil's length from Pole #72 to Pole #101 (middle).

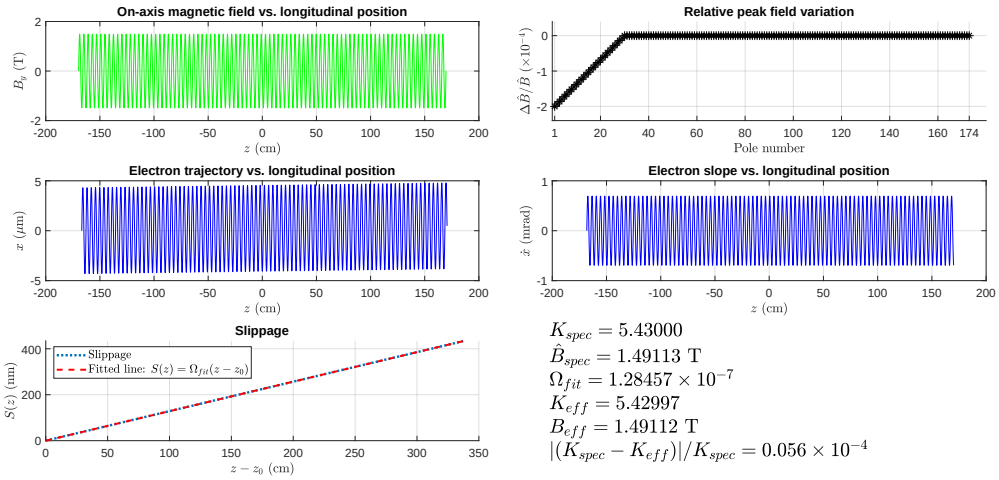

Figure 3.10: Simulation and K_{eff} calculation considering that the field decreases linearly from Pole #1 to Pole #30 (US end).

relationship between ψ and K_{eff} is hard to achieve, given that the coil covers a limited length of the undulator. As one may observe in the simulations, different scenarios, designed to generate the same change in ψ, provide different calculated changes in K_{eff}.

Having discussed the theoretical aspects, the remaining parts of this chapter addresses the actual system, namely, coil construction, software development, peripheral components, undulator gap motion, results, and discussion.

Before moving to the next section, let us comment on the tight requirements of undulator field integrals. As illustrated in figures 3.6 and 3.7, a single pole strength change acts as a

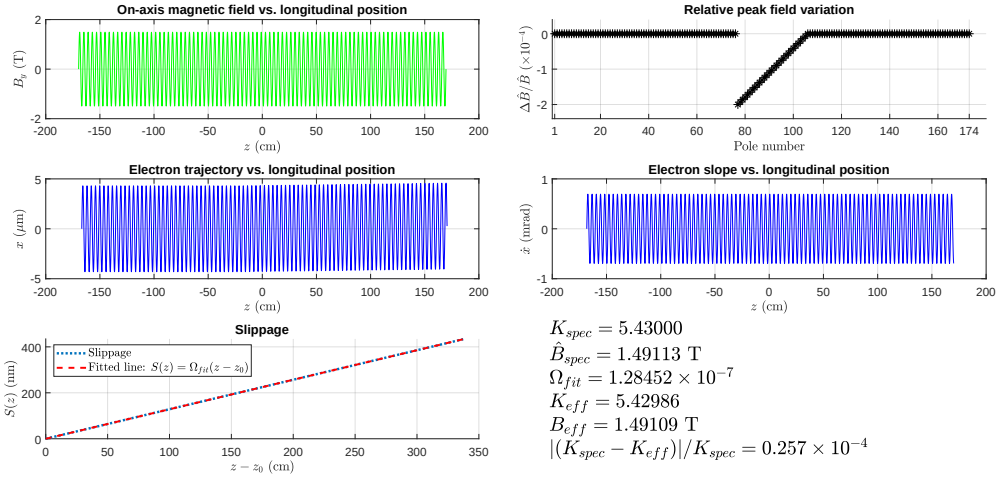

Figure 3.11: Simulation and K_{eff} calculation considering that the field decreases linearly from Pole #78 to Pole #107 (middle).

dipole field, deflecting the electron beam trajectory. To understand how this change "kicks" the electron, we integrate the field along the damaged pole length (half undulator's period) and multiply by $e/(\gamma m_e v_z)$, as previously defined as the electron slope. For a change of 0.3% in only one pole,

$$\begin{aligned}\dot{x}_{\text{kick}} =& \frac{e}{\gamma m_e v_z}\int_{\lambda_u/4}^{3\lambda_u/4} 0.003\hat{B}\cos\left(\frac{2\pi z}{\lambda_u}\right)\mathrm{d}z = \frac{e}{\gamma m_e v_z}0.003\hat{B}\frac{\lambda_u}{\pi} \\ =& 0.075\,(\mathrm{Tm})^{-1}\times 0.003\times 1.49\,\mathrm{T}\times 0.039\,\mathrm{m}\times\frac{1}{\pi} = 4.162\,\mu\mathrm{m/m}.\end{aligned} \tag{3.33}$$

The electron would be approximately 14 µm away from the axis at the end of the undulator if the kick happens at the first pole (4.162 µm/m × 3.4 m). If the kick occurs in the middle of the undulator, the end position is half of this value (i.e., approximately 7 µm). Both values match with the simulation shown in figures 3.6 and 3.7. As explained in Section 2.9, the electron end position must be smaller than 11 µm for the LCLS-II undulators. For the other cases, the effect on the trajectory was smaller, given that opposite polarity of adjacent poles cancels each other's deflection [34].

3.5 System Developments

3.5.1 Flexible Printed-Circuit Coil

Figure 3.12 shows the flexible coil designed to measure flux changes in the soft X-ray undulators for the LCLS-II project at SLAC. The coil is a double layer flexible Kapton

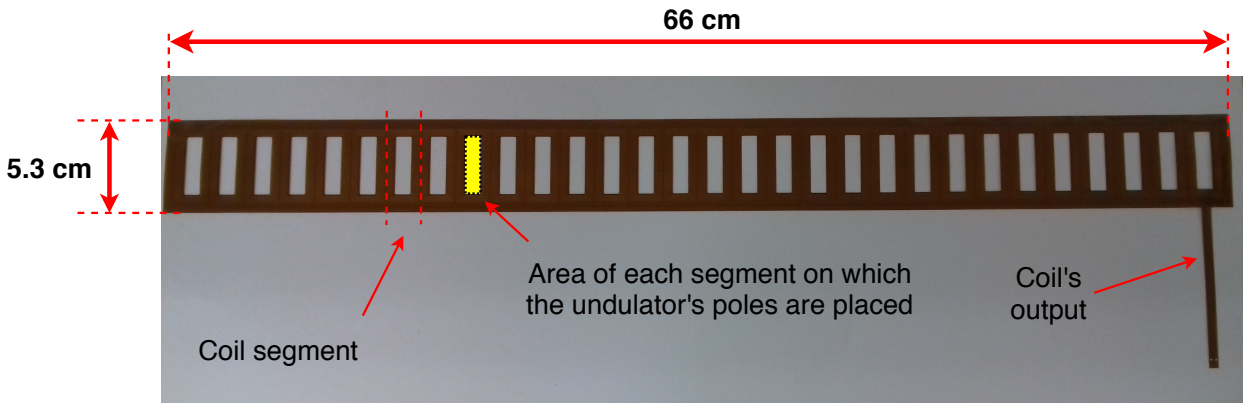

Figure 3.12: Flexible coil used for flux change measurements for soft X-ray undulators. ©2019 IEEE [53].

substrate with 40 windings per pole (or per coil segment) and 100 µm copper trace thickness. Figure 3.13 shows the details of a segment. Being a polyimide film, Kapton exhibits a good radiation resistance — with a threshold damage occurring at a dose of 8.6×10^5 rads [54] — and an exceptional thermal stability [55]. The total thickness of the coil is 120 µm. The coil length is 66 cm, which covers 30 poles, and the coil width is 5.3 cm.

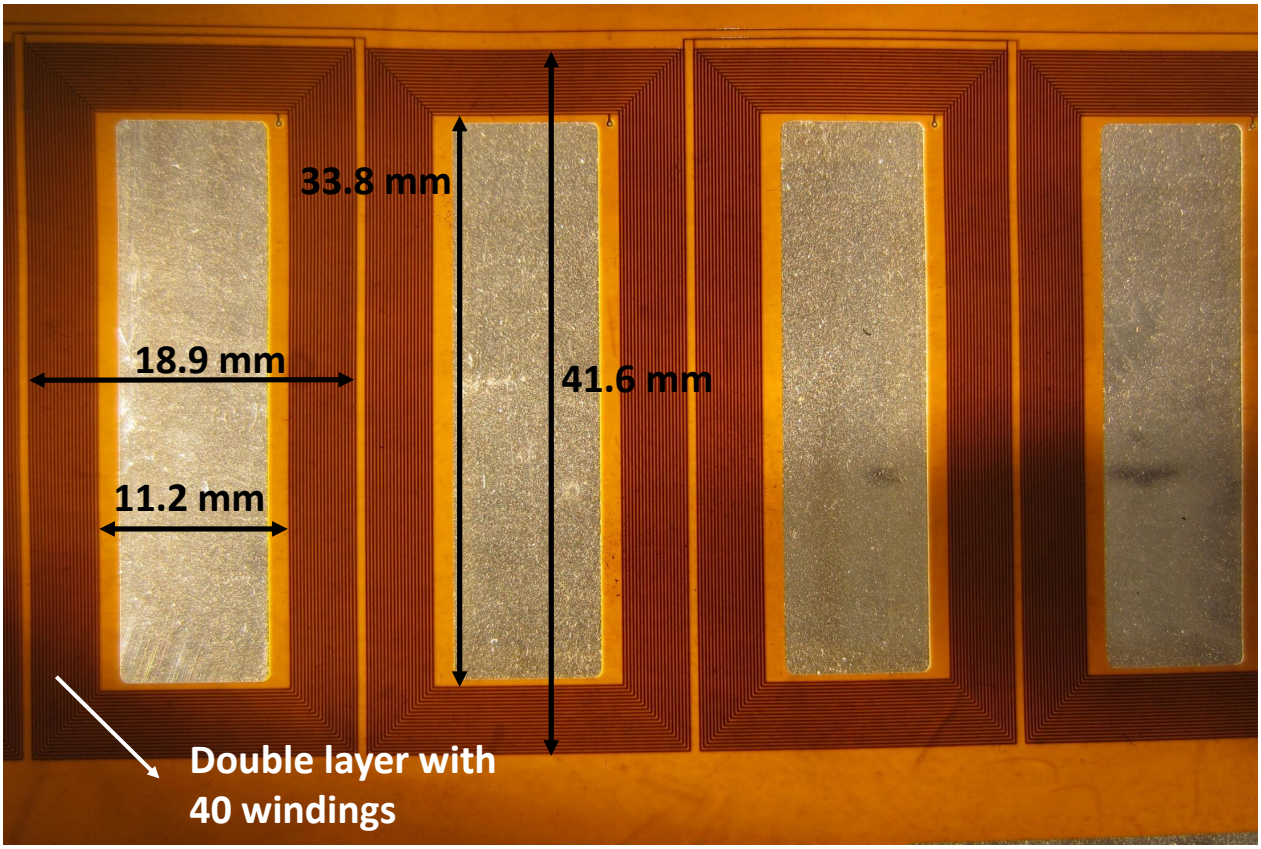

Figure 3.13: Detail of a coil segment. Each segment has 40 windings, and the winding direction alternates from pole to pole. ©2019 IEEE [53].

A program in Matlab creates the coil's layout based on the undulator's dimensions and desired features, making it convenient to change parameters and fabricate new coils for different undulators. Since adjacent poles have opposite field polarity in undulators, the coil winding direction alternates from pole to pole, so the signals add for all the windings around the poles.

The effective area was calculated by using the model presented in Section 3.2. Based on the features described above, $n_L = 2$, $N_w = 20$ (total of 40 windings per segment), $\lambda_u = 39\,\text{mm}$, $L = 11.2\,\text{mm}$, and $\Delta L = 0.1\,\text{mm}$. Since the width of the inner winding is

33.8 mm (see Fig. 3.13) and the pole's width is 32 mm, $W = 32\,\text{mm}$. Replacing these values into (3.28), we find $k_c = 0.413\,\text{m}^2$.

It is worthy of spending a few words pondering over the implications of the calculated effective area. Given that the coil has 30 segments, each one has an effective area of $0.014\,\text{m}^2$. The on-axis peak field is in order of 1 T. A change of 10^{-4} would be equivalent to roughly 1 G. Such a field change would induce a signal of $0.014\,\text{m}^2 \times 10^{-4}\,\text{T} = 1.4\,\mu\text{Vs}$ per segment, higher enough to be read according to the available technology for voltmeters and integrators. Therefore, the choice for the number of segments does not depend on the desirable signal strength, but on a reasonable number of poles that should be covered to monitor the field. Based on the literature review presented in Section 2.7, a length of about half a meter (0.66 m in our case) appears to be enough to detect field degradation.

For initial tests, the whole coil was attached to the undulator by using layers of Kapton tape, as shown in Fig. 3.14. This procedure avoids coil movement from air currents, which might be one of the main sources of errors in the system.

3.5.2 Temperature Control and Measurements

The temperature dependence of PM material is well known. Typically, the strength of permanent magnets is very sensitive to temperature, changing by approximately $-0.1\,\%/°\text{C}$ [56–58]. It means that a temperature change of 0.1 °C in the undulator's magnets would be enough to change the field by 10^{-4}, the same order of the requirements for the system. Therefore, the tests need to be carried out in a well-controlled temperature environment.

The room where we performed the tests was designed to keep the ambient temperature constant within ±0.5 °C [58]. The local undulator temperature in the LCLS-II undulator hall will stay stable within ±0.1 °C during operation, with an average undulator temperature of 20 °C [52].

Five two-wire thermistors model Keysight 34308A were used to measure temperature. Four were set in the undulator strongback, and one was used to measure room temperature. The sensors were embedded into an aluminum case by using the 3M™ Scotch-Weld™ Epoxy Adhesive EC-1838 B/A Green. This epoxy has high dielectric strength and thermal conductivity [59]. The encase was designed to be inserted in threaded holders that can be screwed

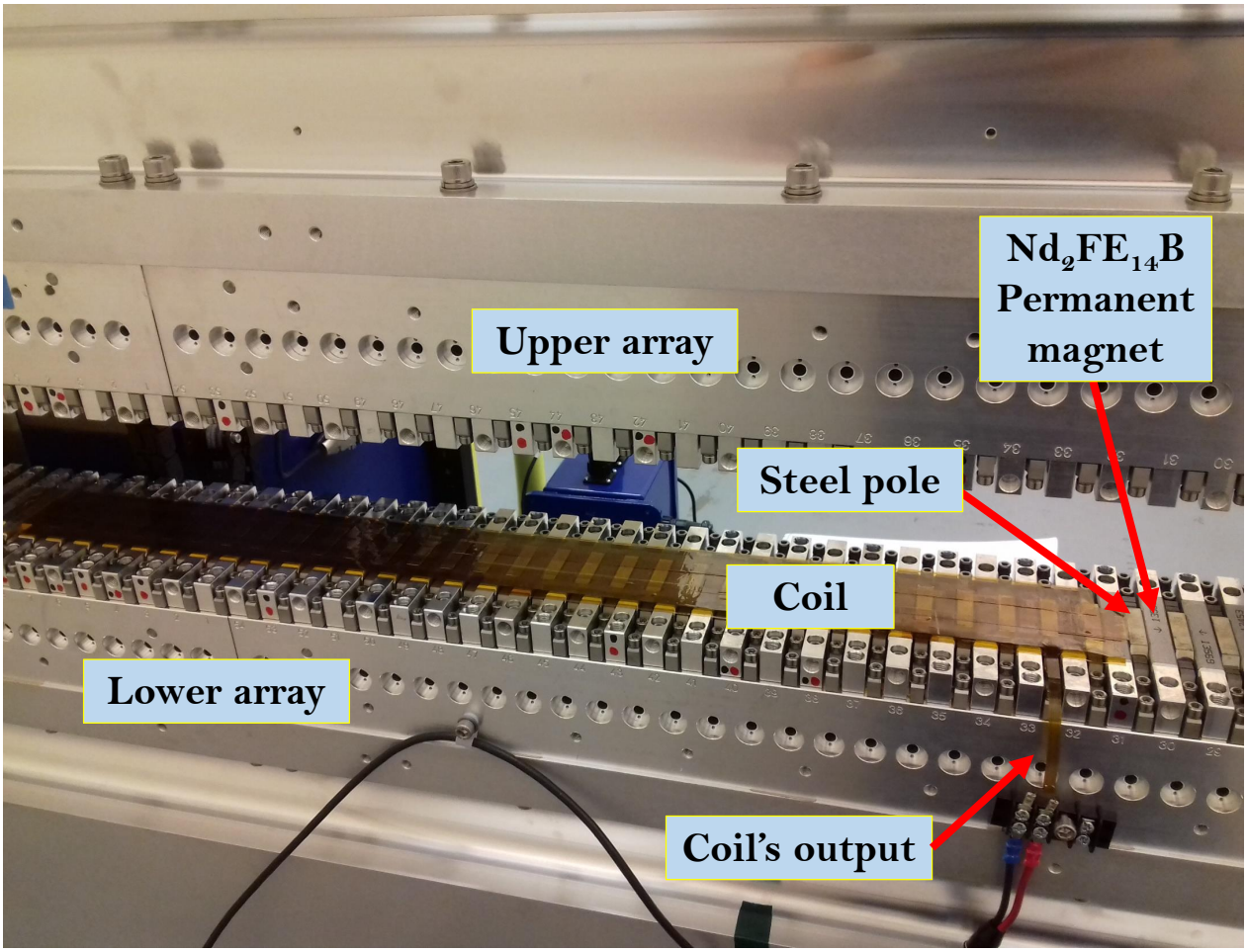

Figure 3.14: Coil attached to the soft X-ray hybrid undulator with Kapton tape. ©2019 IEEE [53].

into the sides of the permanent magnets, as shown in Fig. 3.15. Figure 3.16 illustrates the design and the actual component. The wires of each thermistor were soldered to a 20 AWG RG 58A/U coaxial cable of about 3 m. An Agilent 34970A reads out the temperature from all the thermistors and sends them to the computer via software through a GPIB connection.

3.5.3 Data Acquisition Systems

A program written in LabWindows/CVI, a National Instruments (NI) software, controls the undulator gap, acquires the signal for voltage and temperature, and creates the data files that contain the results. The software operates on a NI PXI-8840 controller. The voltmeter used for voltage acquisition was a NI PXIe-4464, a 24-bit ADC with four input channels and six full-scale ranges. At unity-gain (0 dB), the full-scale range is ±10 V; at the maximum

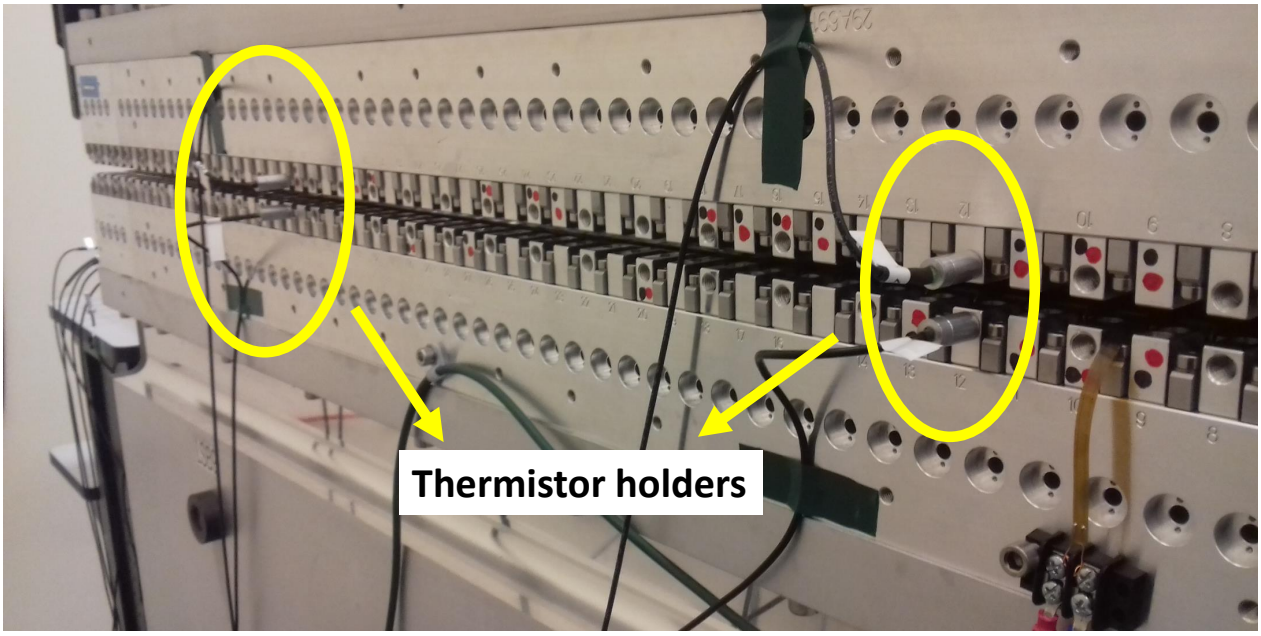

Figure 3.15: Temperature sensors set in the undulator.

gain (30 dB), the module can measure signal within ±0.316 V. We expect a signal level within the smallest range, which gives a resolution of 40 nV (disregarding the noise). To read 1 part in 10 000 (equivalent to 100 ppm or 10^{-4}), it would be necessary at least 14 bits ($1/2^{14} \approx 6 \times 10^{-5}$). Therefore, even with a noise level on the order of µV, the chosen voltmeter guarantees, in principle, the desired resolution.

Both the PXI-8840 and PXIe-4464 modules were installed in a NI PXIe-1062 crate. A 7.5 m 20 AWG RG 58A/U coaxial cable (50 Ω) connects the end of the coil to the PXIe-4464 channels. The sampling rate of the PXIe-4464 was set to operate at 100 Hz (minimum) to reduce high-frequency noise effects. Before and after the undulator gap movement, the signal is measured for 1 s (100 samples) and 4 s (400 samples), respectively. These samples are used to perform voltage offset correction. Many techniques for eliminating offsets were tested, and the most successful one regarding precision is described below.

The PXIe-4464 operates in two modes of input connections: differential and pseudodifferential mode. Both can be used for measuring floating signal source (i.e., not connected to building ground). We chose the differential mode since it offers a better common-mode rejection ratio (CMRR) than a pseudodifferential input, being suitable to deal with capacitive coupling.

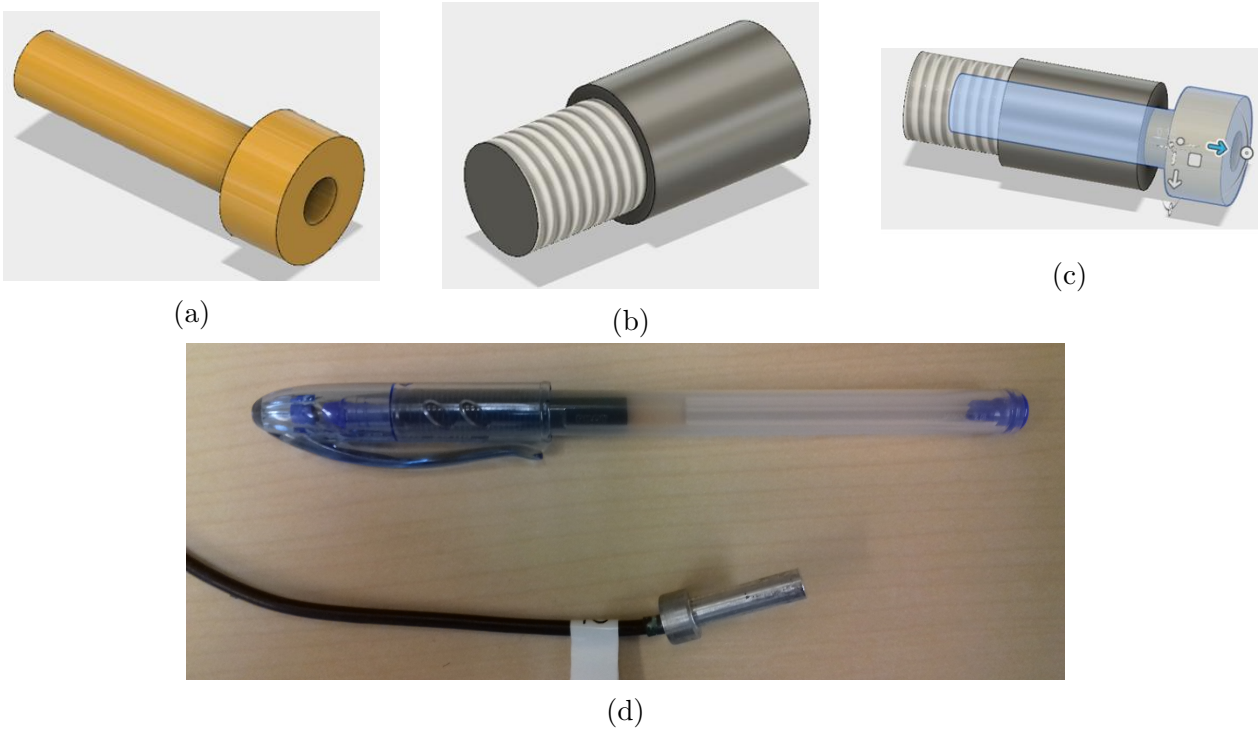

(a) (b) (c)

(d)

Figure 3.16: Structure used to measure room and undulator temperatures. (a) Thermistor encase. (b) Thermistor encase holder. (c) Thermistor encase and holder combined. (d) Actual sensor (the thermistor was embedded into the case with epoxy).

3.5.4 Capacitive Coupling

The undulator gap drive system is based on servo motors with feedback from internal rotary encoders and a gap encoder placed at the end of the undulator [60]. Given the features of the flexible coil (e.g., its several windings), electromagnetic interference-related issues inherent to these motors — or even from the environment — may affect the system.

During initial tests, we observed ground fluctuation between the measuring system and the undulator. More specifically, for a fixed gap and powered servo motors, a voltage difference of 3 mV DC and 0.6 $\mathrm{mV_{RMS}}$ AC between the ground of the PXI crate and the undulator strongback. The flexible coil windings and the array of magnets are separated by a Kapton material. As a consequence, undesirable capacitive coupling between the undulator jaws and the coil may appear, causing noise to the signal. Figure 3.17 illustrates the capacitive coupling issue.

Let V_g be the AC component of the voltage between the undulator strongback and building ground. It is possible to demonstrate that the AC component of the voltage between the

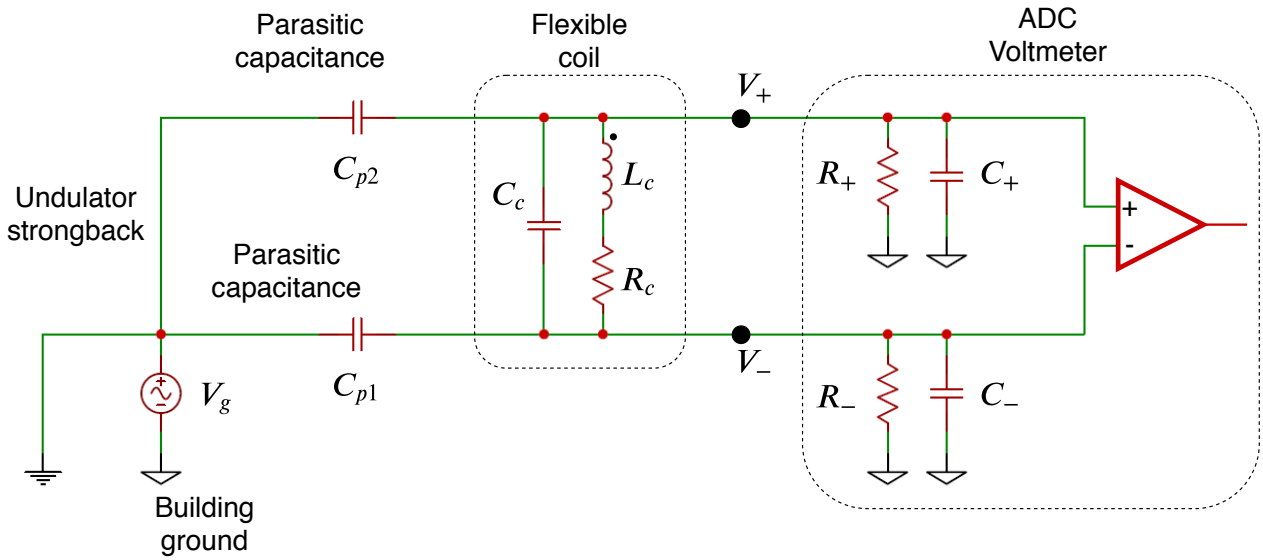

Figure 3.17: Representation of parasitic capacitances and equivalent circuit of the flexible printed-circuit coil.

PXIe-4464 input is proportional to V_g, which represents an error in the measurement. To overcome this problem, a 12 AWG wire was connected between the undulator strongback and the PXIe-4464 ground, reducing, in theory, V_g to zero.

The use of a low-pass filter may be consider to reduce electrical noise. Nevertheless, such devices must be carefully selected and applied, since it is necessary to ensure that the filter's components are stable to within the desirable resolution. Gain stability would be also required when using operational amplifier as buffer to isolate the flexible coil from the cable. Neither filters nor operational amplifiers were used for the tests we performed with the RDDS.

3.5.5 Undulator Motion Parameters

The larger the gap change, the higher the integrated voltage [see (3.17)] and the longer the sampling time. The choice of the initial and final gap g_1 and g_2 is an attempt to accomplish low sampling time and high signal levels or, in other words, to minimize the integration of electronic noise and to increase the signal-to-noise ratio. A gap change from 7.3 mm to 11.3 mm (or vice-versa) was found to give the best combination of signal and short movement time. Each jaw's speed was set to 0.4 mm/s and the acceleration was set to 0.25 mm/s^2.

The requirements of the motion control for the soft X-rays undulators establish that the gap repeatability must be smaller than 5 µm, and long-term gap stability (24 h) must be within ±1 µm [60]. The gap positioning variation for a specific gap was on the order of 0.5 µm. In this context, a *cycle* is defined as opening and closing the gap between two gap distances. Depending upon whether we open or close the undulator jaws, the signal of the integrated voltage will be positive or negative. The sections that follow will use absolute values of ψ.

3.6 Preliminary Measurements and Data Processing

This section presents the initial measurements performed with the RDDS. We took one measurement with 10 cycles every 30 minutes during a whole day to observe system performance, including noise levels, repeatability, and gap positioning.

3.6.1 Induced Voltage

Figure 3.18 shows all the voltage samples taken during the 24-hours measurement for opening and closing the gap between 7.3 mm and 11.3 mm. Considering the delay before and

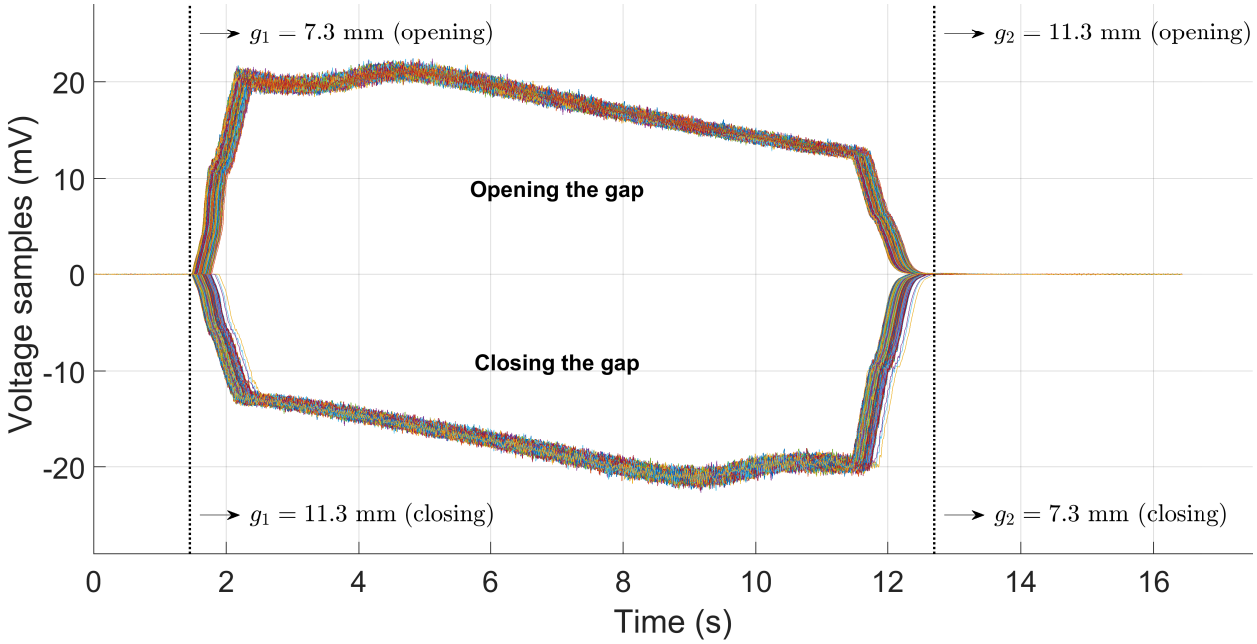

Figure 3.18: Voltage signal induced in the coil for gap cycles between 7.3 mm and 11.3 mm during one day.

after the gap movement, the total time is around 16 s. The amplitude is around 22 mV, and the reference integrated voltage (defined in Chapter 1) is approximately 0.17 Vs. For now, two significant figures are enough for the discussion that follows. Figure 3.18 also gives a qualitative idea about synchronism and repeatability.

The milliseconds of delay among the curves is not an issue, given that voltage samples are taken during a few seconds before and after the gap movement. In theory, these voltage samples are zero since the gap is fixed. Nevertheless, electronic noise and offset on the order of 10 µV is present; for instance, integrating a 10 µV offset over 16 s gives 160 µVs — an error almost ten times larger than the required limit. Before explaining how the voltage offset is compensated, let us identify and explain four distinct moments of the induced voltage profile. Consider the typical signal shown in Fig. 3.19. One of the curves of Fig. 3.18 for opening the gap was selected for no particular reason since all of them are similar. It should be noted that the signal profile for closing the gap has the same voltage profile, although flipped in amplitude and time.

At the gap g_1, the undulator gap movement starts from a stationary position, accelerating

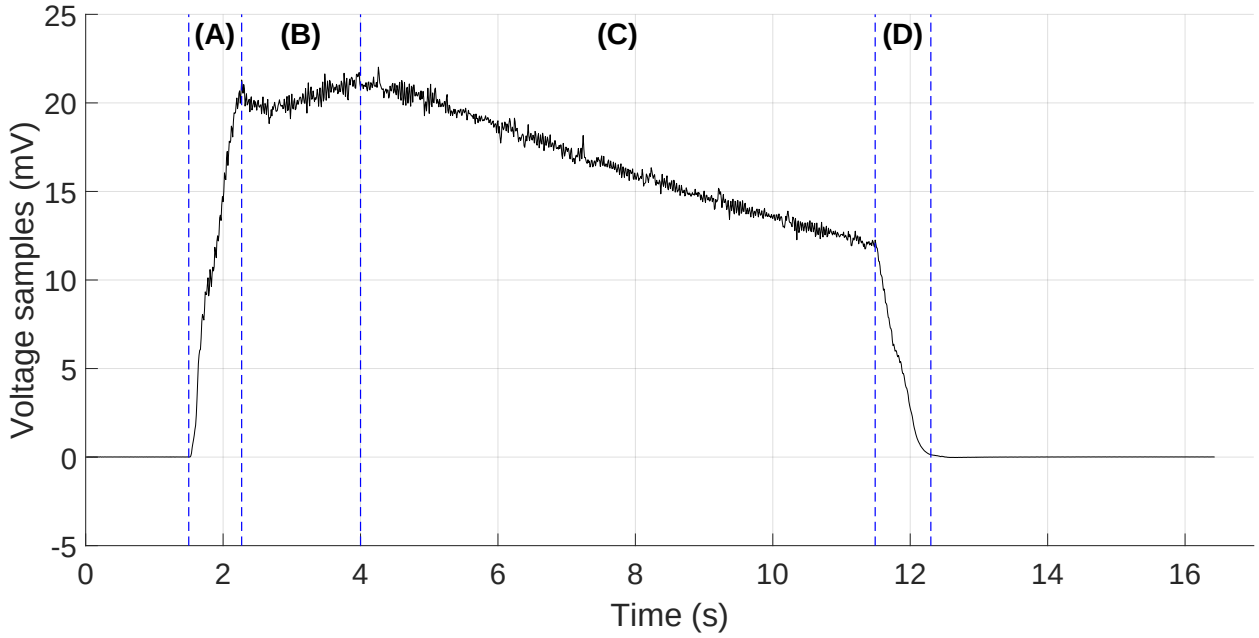

Figure 3.19: Typical voltage samples for gap changes between $g_1 = 7.3$ mm and $g_2 = 11.3$ mm. The period (A) and (D) represent the accelerated motion of the gap. The period (C) represents the constant motion of the gap. The period (B) shows small steps of acceleration/deceleration of the gap to reach the specified speed. Figure adapted from [53].

to its nominal velocity. The induced voltage linked to the acceleration corresponds to the region (A) in Fig. 3.19. The curve observed in (B) appears due to the undulator's motors accelerating/decelerating in small steps to reach the specified velocity smoothly. Once the nominal value is reached, the constant speed of the gap movement induces the profile seen in (C), up to roughly the gap position g_2. Then, the control system decelerates the movement on the same rate of the initial acceleration, generating the drop observed in (D). Notice that (A) and (D) take approximately the same interval of time.

3.6.2 Offset Correction

To understand the offset correction technique that was applied to voltage samples, consider the induced signal from a single gap movement. Zooming in on the samples around 0 V within the range of a few dozens of microvolts allows identifying the noise level clearer, as shown in Fig. 3.20a. To perform the correction, a line is fitted (red dashed line) by linear regression using 100 samples at the beginning and 150 samples at the end (blue). The corrected voltage samples are calculated by subtracting the fitted line values from the original samples. Figure 3.20b shows the samples before and after the jaw movement after the correction.

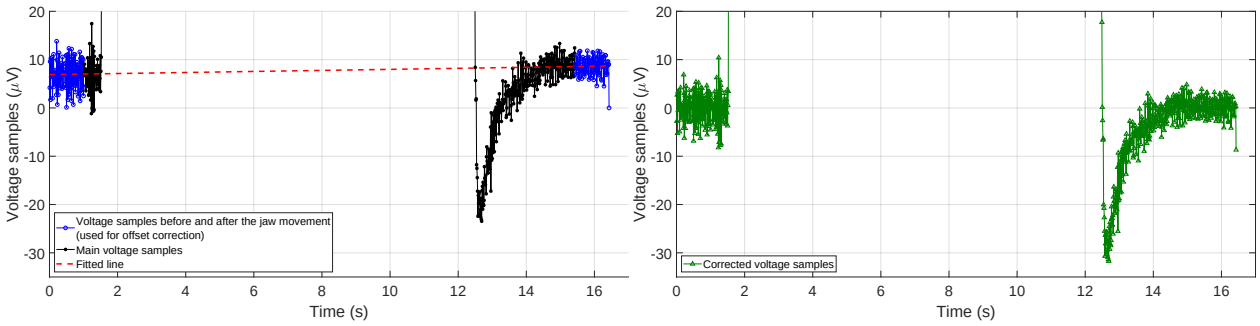

(a) (b)

Figure 3.20: (a) Original and (b) corrected voltage samples before and after the gap movement. The first 100 and the final 150 voltage samples (blue) define a fitted line (red dashed line) by linear regression. The corrected voltage samples (green) correspond to all the original samples (blue and black) with the fitted line subtracted. ©2019 IEEE [53].

The negative overshoot shown on the right side of Fig. 3.20a is caused by the undulator's motors correcting the gap position after the jaws overshoot their defined positions. Because of that, it is necessary to take voltage samples for a few seconds after the nominal movement stops. Since the jaws are stationary at the beginning, one second of sampling is sufficient.

3.6.3 Flux Change Calculation

After the offset correction, a flux change sample is calculated by numerically integrating the voltage samples. Mathematically,

$$\psi_{\text{samp}} = \frac{1}{2f_s}\left|\sum_{i=1}^{T_t f_s}(V_{i+1} + V_i)\right|, \tag{3.34}$$

where f_s is the sampling rate, V_i is the i-th corrected voltage sample, and T_t is the total time of acquisition. Figure 3.21 shows all the flux change samples associated with positive and negative gap movements.

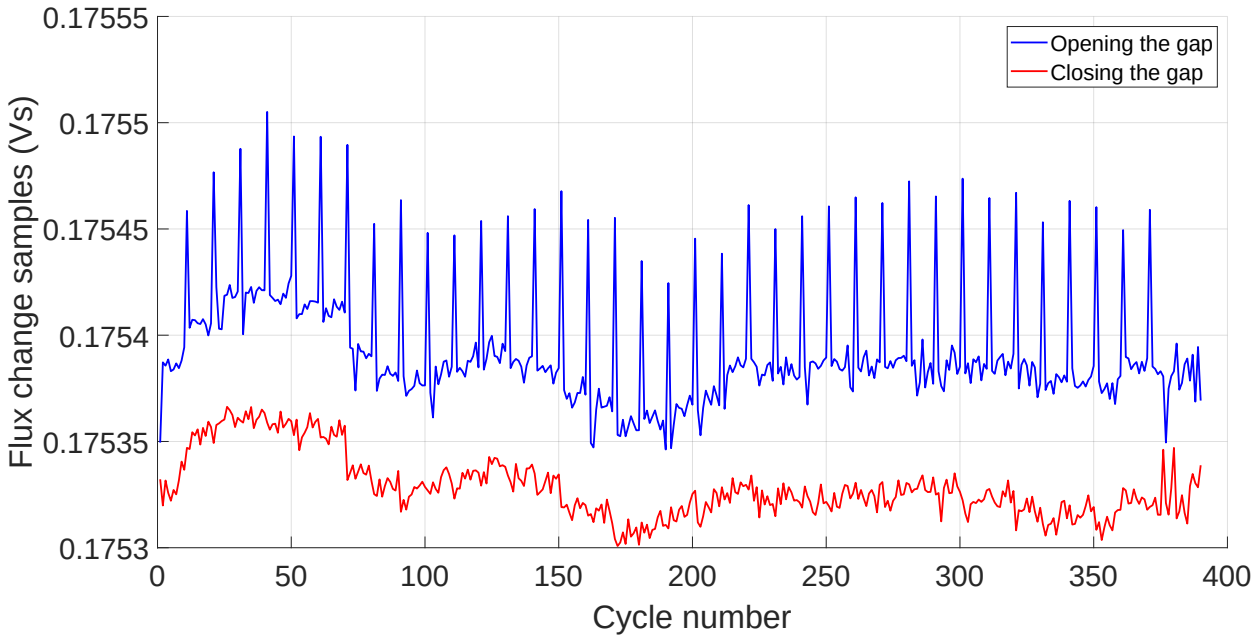

Figure 3.21: Flux change samples obtained from the 24 h test shown in Fig. 3.18.

A systematic spike appears in the samples for positive movements, more specifically at the first opening of each set of 10 cycles. A close investigation showed that the spikes occurred due to a small displacement of the initial gap g_1 at the beginning of each set (so far for unknown reasons). Figure 3.22 presents the gap values (initial, final, and change) read from the linear encoders during the opening and closing of the gap.

Although the spikes are undesired, they show the high sensitivity of the system, given the correlation between the peaks from the flux change samples and the gap change. Besides, they prove that a linear correction can be applied to the data for small gap changes if the

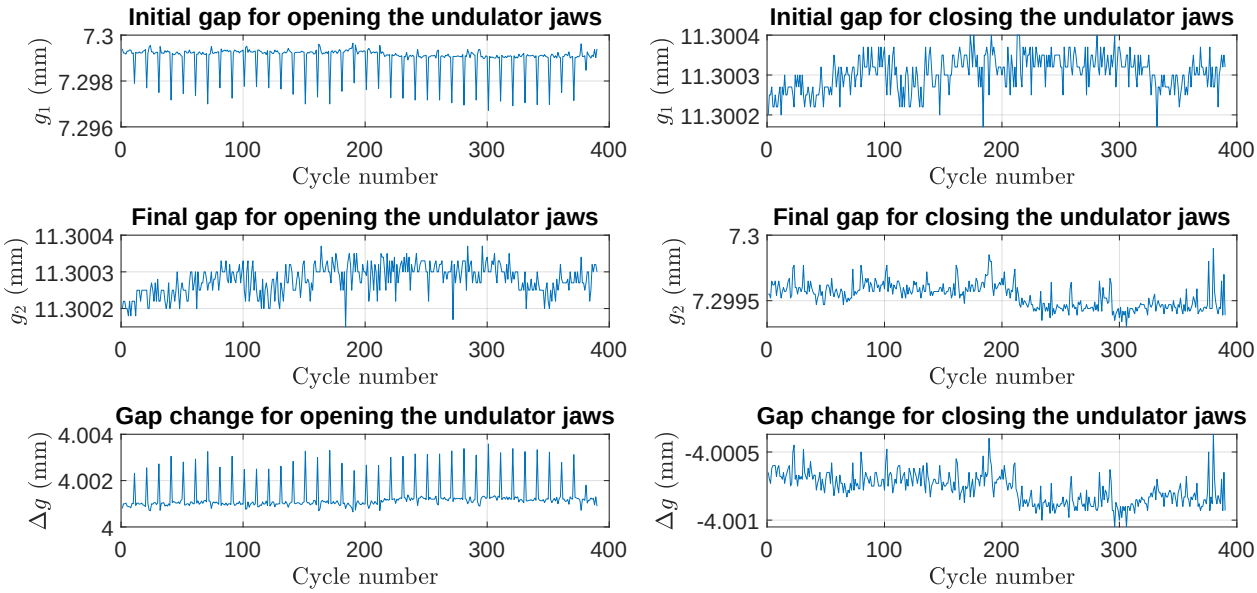

Figure 3.22: Initial gap, final gap, and gap change for opening and closing during the 24 h test.

gap position is precisely known. Let Δg_R be a gap change reference during one cycle and Δg_i be the i-th gap change read during the i-th gap movement. The corrected flux change ψ'_{samp} can be calculated as

$$\psi'_{\text{samp}} = \psi_{\text{samp}} \frac{\Delta g_R}{\Delta g_i}, \tag{3.35}$$

where ψ is given by (3.34). The reference Δg_R is calculated by averaging all the Δg_i associated with the cycle except the first sample, which corresponded to a spike for all the cycles while opening the gap. Figure 3.23 compares the previous result with the corrected samples.

The data depicted in this section, while preliminary, suggest two things. First, the peaks in Fig. 3.21 are approximately 6×10^{-4} higher than the "natural trend" of the curve. Since the spikes occurred whenever the gap change is different by roughly 1 µm (see Δg for opening the gap in Fig. 3.22), the correlation indicates that the system's resolution level is better than 0.06%. Notice that the spikes are not present for closing the gap, and the original and corrected data are quite similar. Second, the smother profile of the corrected curve for opening the gap in Fig. 3.23 implies that the gap correction technique is suitable for its purpose.

Figure 3.23 suggests that the stability can be improved by applying gap corrections,

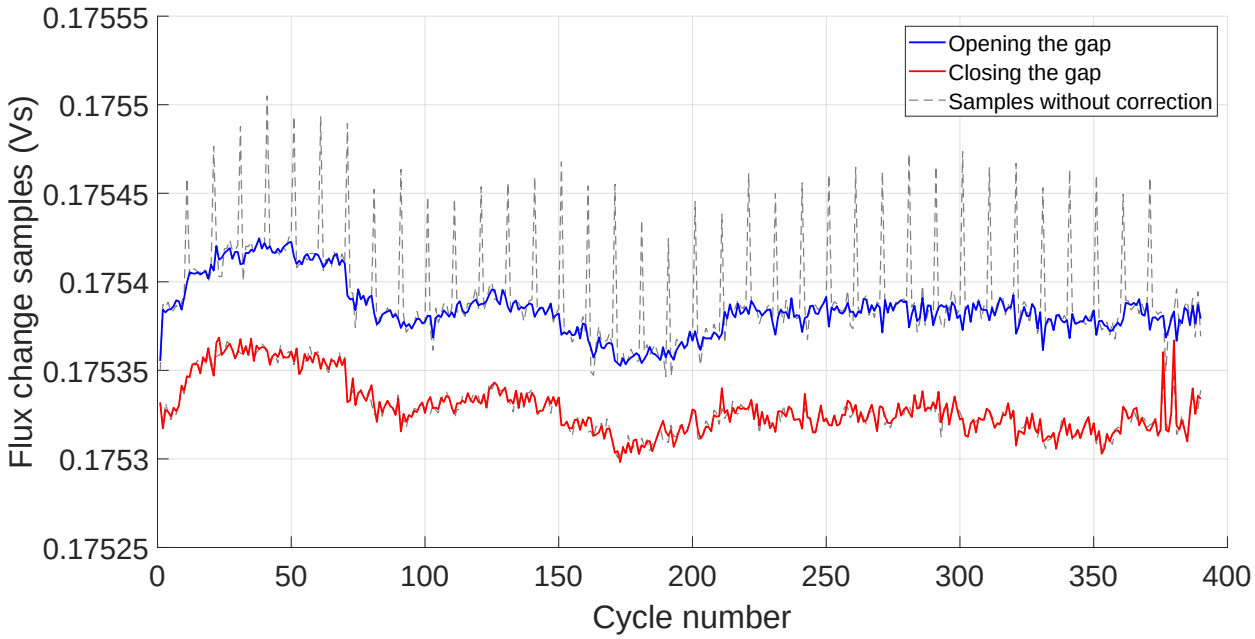

Figure 3.23: Corrected flux change samples for opening and closing the gap, and comparison with the uncorrected data.

mainly for cases in which the gap positioning is not as precise as micrometers. In our case, the gap positioning is highly precise, and the spikes consistently occur in the first opening movement; hence, the data associated with them can be removed from the set of data with no loss of information.

3.6.4 Flux Change Repeatability

In the tunnel, the undulator is not expected to be available for the whole day as it was for the measurements showed above, but rather available to perform a few gap movements. We decided to define a single measurement as the average of 10 flux change samples, which are calculated from (3.34) and (3.35). Indeed, this was the primary reason for taking a delay of 30 minutes between a set of 10 cycles. Besides, averaging helps in increasing the signal-to-noise ratio. Considering the time that the undulator takes to move Δg and the further delays, the system requires approximately 8 minutes to perform the data acquisition of 10 cycles. The results with error bars ($\pm 1\sigma$, with σ being the standard deviation of the set of samples) are depicted in Fig. 3.24 for opening and closing the gap. We adopted the variable ψ_k to represent the averaged flux change associated with the k-th set of samples, as will be seen in

Section 3.8. In relation to the total average, most of the data points fall into the $\pm 10^{-4}$ limit. The room temperature oscillated between 19.85 °C and 20.54 °C ($\Delta T = 0.69$ °C), while the magnet array temperature changed from 19.98 °C to 20.09 °C ($\Delta T = 0.11$ °C). The long-term errors are higher than the short-term errors, probably due to thermal drifts.

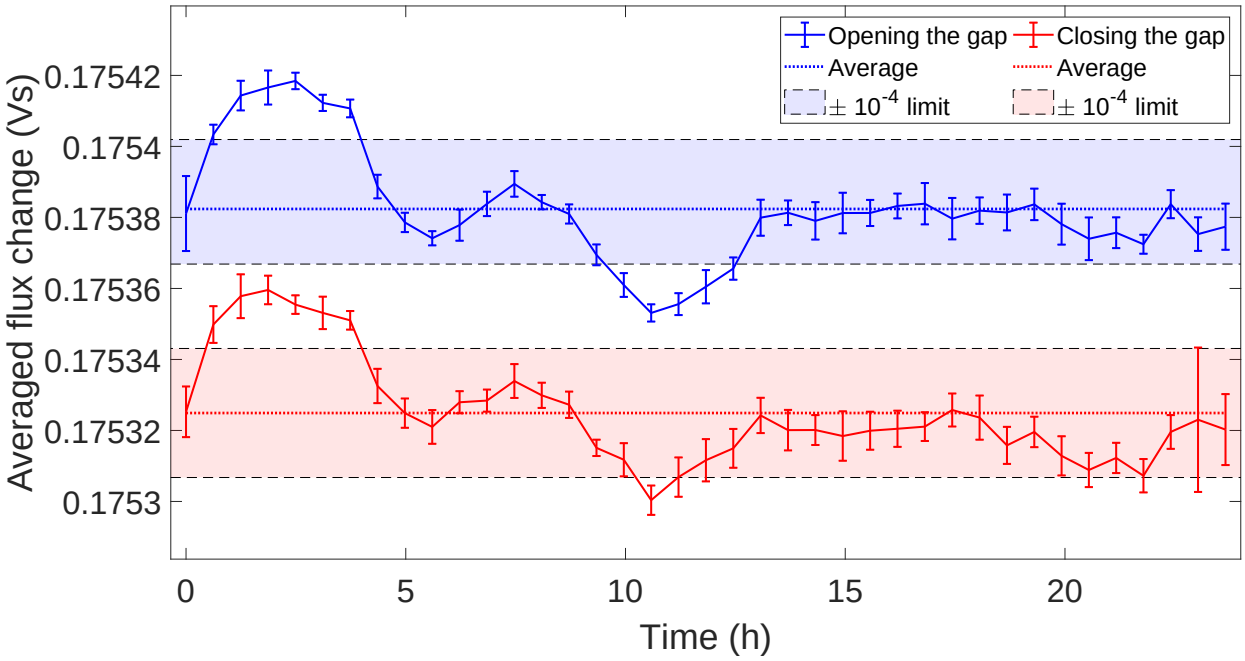

Figure 3.24: Averaged flux change and error bars over set of 10 flux change samples for the 24 h test.

One may notice the difference between the samples for opening and closing the gap; both curves have a similar profile, such that the separation is practically constant with a discrepancy of roughly 60 µVs (approximately 0.03%). According to (3.17), for a fixed gap change $|\Delta g|$, the absolute value of ψ should be the same, independently whether the undulator jaws are opening or closing. Indeed, the $|\Delta g|$ difference between the opening and closing of the gap was always smaller than 0.8 µm (disregarding the spikes), which therefore does not justify the difference in ψ. The coil is well-fixed in the undulator, and the difference between the curves is systematic. Thus, we assume that the effective area of the coil is constant. A possible explanation of the difference may be attempted by considering that the magnetic field through the coil changes depending upon the gap movement orientation. Two sources of error were analyzed: eddy-current losses and external noise from servo motors. Besides them,

undulators may also exhibit some level of hysteresis. Nevertheless, it is unlikely that such a phenomenon produces a change of 0.03% in the field strength of the SXR undulators [61].

The SXR undulator poles are made of Vanadium Permendur, a cobalt-iron soft magnetic alloy. When the gap changes, the variation of the undulator field induces a circular current in the pole in such a way that the magnetic field generated by this current opposes the change that induced it, as dictated by Lenz's law. As a consequence, the field variation over time is reduced, which decreases the induced voltage signal. Fortunately, the integration of the induced voltage overcomes this issue. The integrated voltage depends, in principle, only on the magnetic flux at the gap g_1 and g_2 [see (3.14)]. If the system waits enough time before and after the gap movement (when the jaws are stopped and, therefore, the eddy current no longer exists), then flux change is not affected. As shown in Subsection 3.6.1, the RDDS starts the voltage acquisition and waits a few seconds before and after the gap movement. This feature of the system also demonstrates that the current induced on a metallic beam pipe due to the gap movement would not be an issue. Indeed, no difference has been observed between measurements with and without a beam pipe.

As known, servo motors may produce electromagnetic interference. We speculated that the influence of the motors during the gap movement might be responsible for the offset observed in Fig. 3.24. If this is the case, then the higher the gap movement time, the higher the difference in ψ between the opening and closing of the gap. To test it, we performed 10 cycles for several different gap changes Δg. In a single cycle, the undulator gap starts at 7.3 mm, opens to 7.3 mm + Δg, and closes to 7.3 mm. Among the groups of cycles, Δg was changed from 2 mm to 13 mm in steps of 0.5 mm. We averaged the samples taken with the opening (ψ_{opening}) and closing (ψ_{closing}) of the undulator gap, calculated the difference for each gap change, and propagated the error. The movement time changes linearly with the gap change. Given the constant speed and acceleration of the jaws during the measurements, we calculated the movement time as a function of Δg. Figure 3.25 shows the results.

The increasing trend reinforces the hypothesis that something external that operates during the movement (seemingly the servo motors) are the main source of interference between the measurements. It should be mentioned that the offset is not necessarily a problem, given that the system's principle requires high relative resolution and precision — considered our

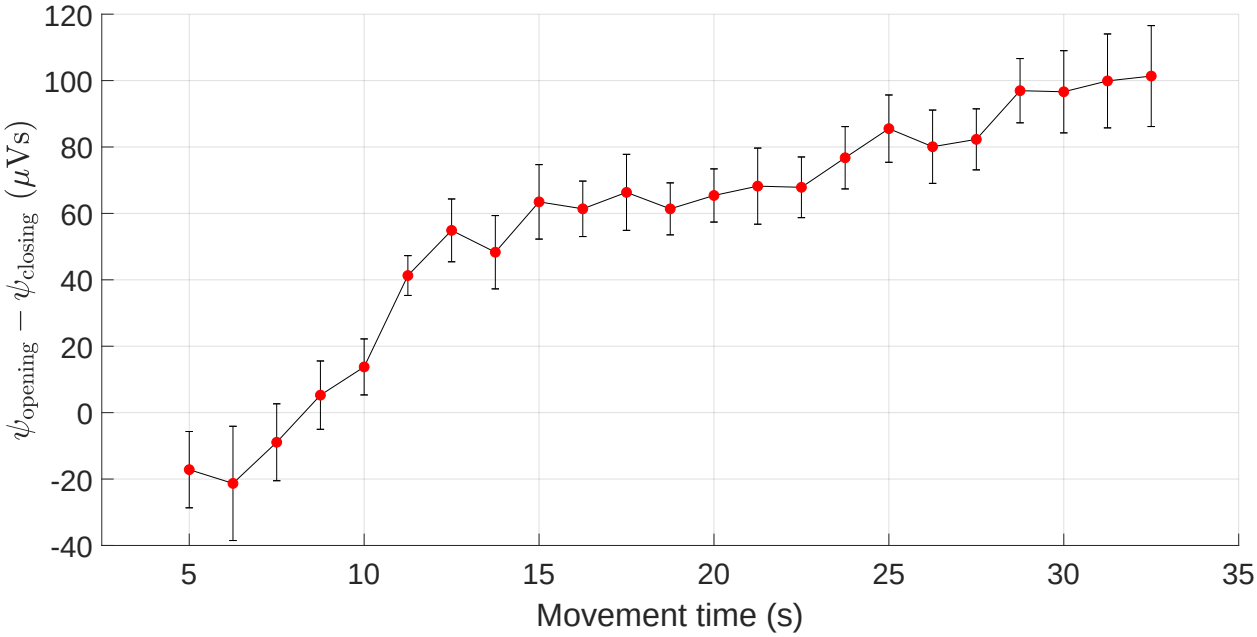

Figure 3.25: Flux change difference between the opening and closing of the undulator gap for different movement time.

leading figures of merit — rather than high accuracy.

By comparing the precision of the measurements for opening and closing of the undulator gap, it is possible to observe that the results oscillate within a similar range. In practical terms, we may assume that the precision for both are equal. Furthermore, the results of this section demonstrated a higher signal strength for the measurements taken with the gap opening, at least for gap movements between 7.3 mm and 11.3 mm. Since it is desirable that the relative precision (or relative error) is as smaller as possible, only the samples with the gap opening will be used in what follows.

3.7 Model Validation and Effective Area Estimation

The Magnetic Measurements Facility (MMF) at SLAC has many different systems to measure and tune undulators, including a Hall probe carried by a high precision Kugler magnetic measurement bench. On-axis peak field measurements for different gaps were performed by using the Hall probe system, which allows fitting the data into (2.46) to determine coefficients B_0, a and b. Figure 3.26 shows the on-axis peak field for different gaps taken for the undulator under test and the fitted line obtained by using the least-squares fitting method.

The calculated coefficients are $B_0 = 4.0623\,\mathrm{T}$, $a = -5.3938$ and $b = 2.1734$, and the Root Mean Square Error (RMSE) is 5 mT.

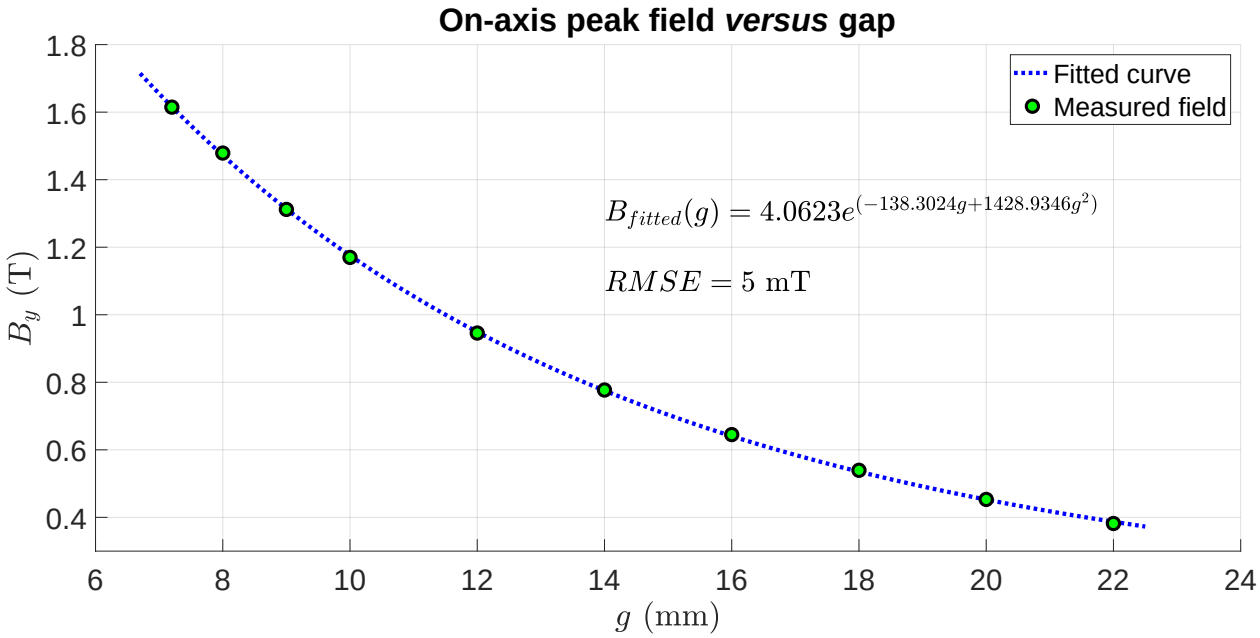

Figure 3.26: On-axis peak field of a SXR undulator and the best fit curve as a function of the gap.

In addition, the flux change ψ was measured for different gap changes Δg. The initial gap g_1 was set as 7.3 mm, and the final gap g_2 was changed by 0.5 mm steps from 7.8 mm to 20.3 mm (i.e., Δg changed from 0.5 mm to 13 mm in steps of 0.5 mm). By replacing the coefficients a and b calculated previously in η [see (3.9)] and fitting the data into (3.17), it is possible to estimate $k_c\overline{B_0}$, as illustrated in the results shown in Fig. 3.27. By doing so, $k_c\overline{B_0} = 1.6946\,\mathrm{Vs}$ with RMSE of 2 mVs. Assuming $B_0 = \overline{B_0}$,

$$k_c = \frac{k_c\overline{B_0}}{B_0} = 0.417\,\mathrm{m}^2, \tag{3.36}$$

which is very close to the value $0.413\,\mathrm{m}^2$ from the model reported in Section 3.2.

The results presented in this section show the validity of the expected gap dependence of the signal presented in (3.17). They also demonstrate that larger gap changes have diminishing increases in signal strength. It is interesting to point out that the RMSE represents the estimation of the standard deviation of the random component in the data. Small values of RMSE observed for the results presented in this section means that the fitted model predicts

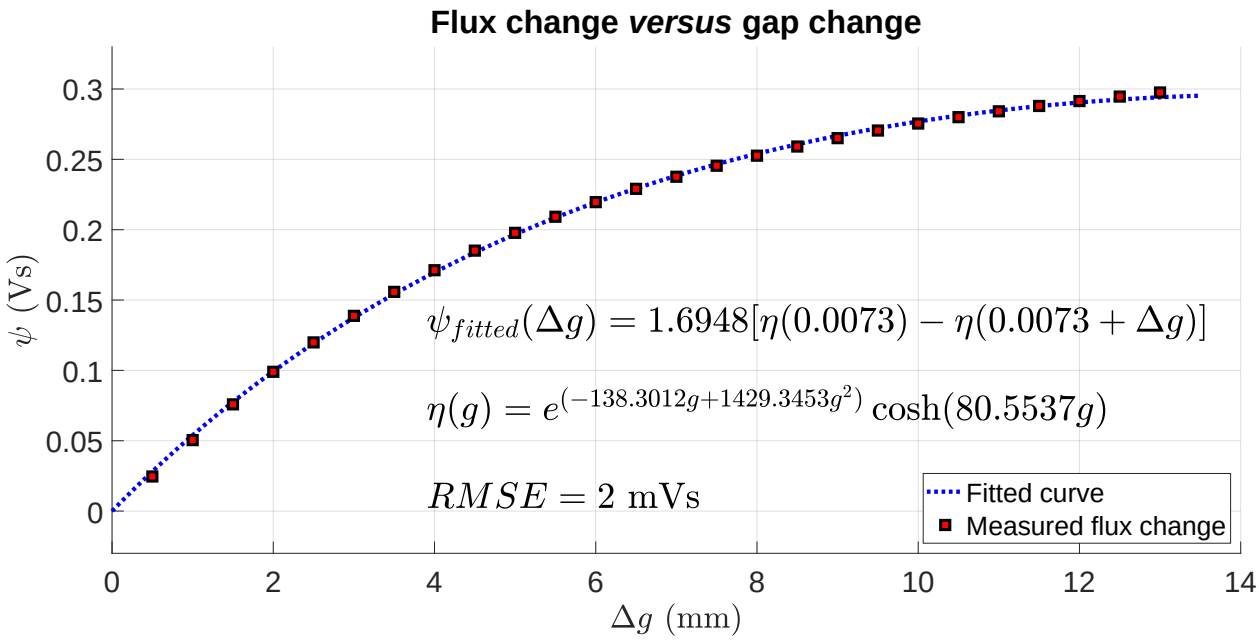

Figure 3.27: Integrated voltage measurements and the best fit curve for different gap changes $\Delta g = g_2 - g_1$.

the data accurately.

3.8 Long-term Measurements

Let the relative deviation of each flux change measurement be

$$\epsilon_k = \frac{\psi_k - \langle\psi\rangle}{\langle\psi\rangle}, \tag{3.37}$$

where ψ_k corresponds to the k-th flux change measurement and $\langle\psi\rangle$ is the mean over all ψ_k values. Figure 3.28 shows ϵ_k and the undulator strongback temperature measured during approximately eight days. The time separation between each measurement was 30 minutes. The standard deviation and mean over all the measurements were 12 µVs and 0.170 976 Vs, respectively, which gives a relative error (standard deviation divided by the mean) of 7.1×10^{-5}.

Mostly, temperature variation was responsible for ψ_k variation. For instance, if we separate the data points shown in Fig. 3.28 before and after 90 h — close to the time that the temperature oscillations started going up — the relative error associated with each group would be 5.2×10^{-5} and 4.6×10^{-5}, respectively. Error bars for individual set of measurements are suppressed here since those errors were typically smaller than 0.005% and do not

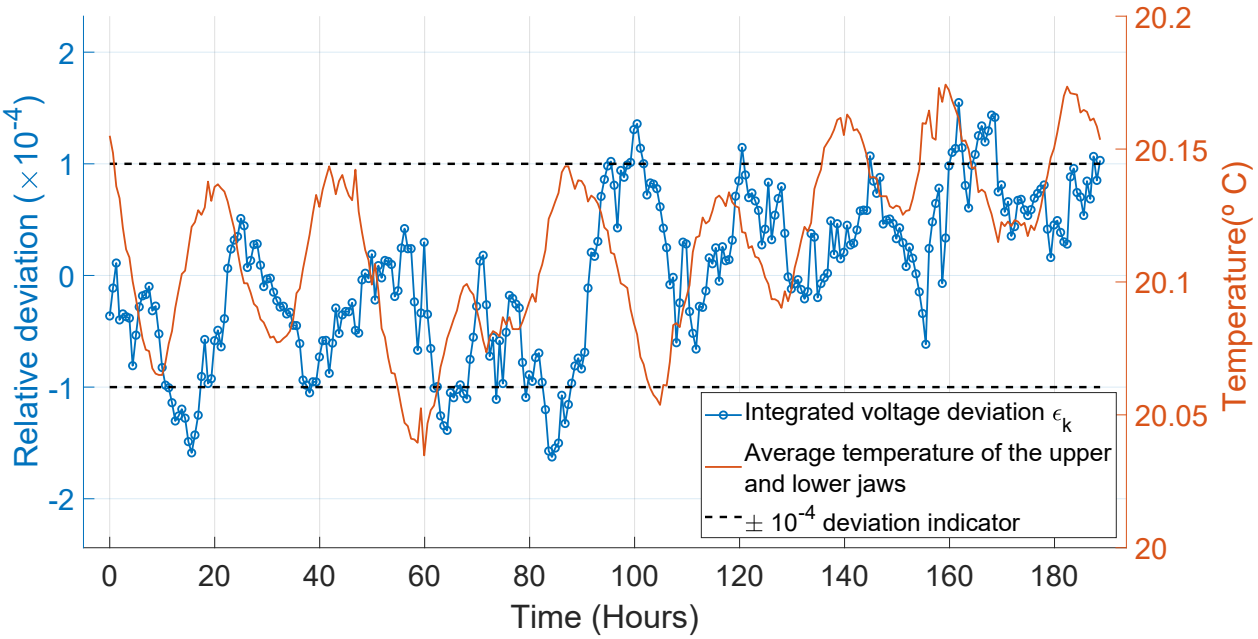

Figure 3.28: Long-term integrated voltage deviation and the average temperature of the magnets for approximately eight days. ©2019 IEEE [53].

add any significant meaning to this analysis. During the long-term test, the room temperature changed between 20.05 °C and 20.71 °C ($\Delta T = 0.66$ °C). The magnet array temperature (shown in Fig. 3.28) kept within the range of 20.04 °C to 20.17 °C ($\Delta T = 0.13$ °C).

Contrary to expectations, the thermal drift observed in Fig. 3.28 produces a positive correlation between integrated voltage and temperature, in such a way that the temperature changes cause the signal changes. Although the field strength of permanent magnets gets weaker when the temperature rises ($\Delta B/(B\Delta T) \approx -10^{-3}/$°C, as described in Subsection 3.5.2), we associate the opposite behavior with the encoder arm (responsible for controlling the gap) changing with temperature more rapidly than the jaws.

3.9 Local Sensitivity Measurements

To test the local sensitivity (i.e., how a system's output varies according to small changes in a system's input around a specific working point), small field changes were performed in a pole covered by the coil. We used tuner magnets [62] — small permanent magnets applied for field correction that can be inserted in the undulator — to change the field (the input in this case) and measure the relative changes on ψ (the output in this case) close to the

reference integrated voltage. It should be noticed that the working point corresponds to the reference integrated voltage, being associated with the given state of the magnetic strength. Therefore, we are interested in the local sensitivity around this point rather than evaluating the global sensitivity — over the entire range — of the system.

A picture of a tuner is shown in Fig. 3.29. Each tuner magnet changes the field by approximately 30 G (3 mT). One controls the orientation of the tuner's field by rotating and fixing it inside holes under the steel poles.

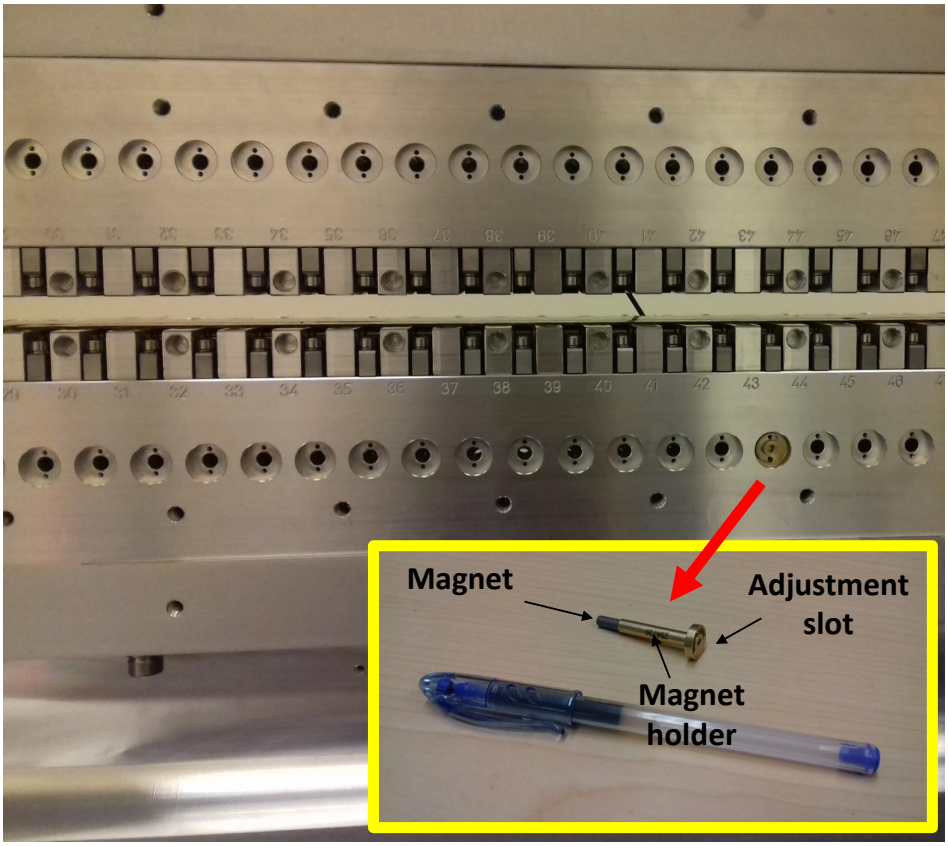

Figure 3.29: Magnet tuners used to adjust magnetic field in undulators.

The gap dependence of the added magnet's field is different from the gap dependence of the undulator field. The additional flux change that the coil measures depends on the gap dependence of the added magnet's field. Experimentally, we could modulate the coil signal by $\pm 10^{-4}$.

First, we took 40 integrated voltage samples in the following order:

(i) 10 samples without the tuners (to define the reference);

(ii) 10 samples with 2 tuners increasing the field;

(iii) 10 samples without the tuners (to define the reference);

(iv) 10 samples with the 2 tuners decreasing the field.

To avoid temperature changes, the samples were taken without delays between them. Figure 3.30 shows the relative deviation of each flux change sample in relation to the average of the first set of 10 samples.

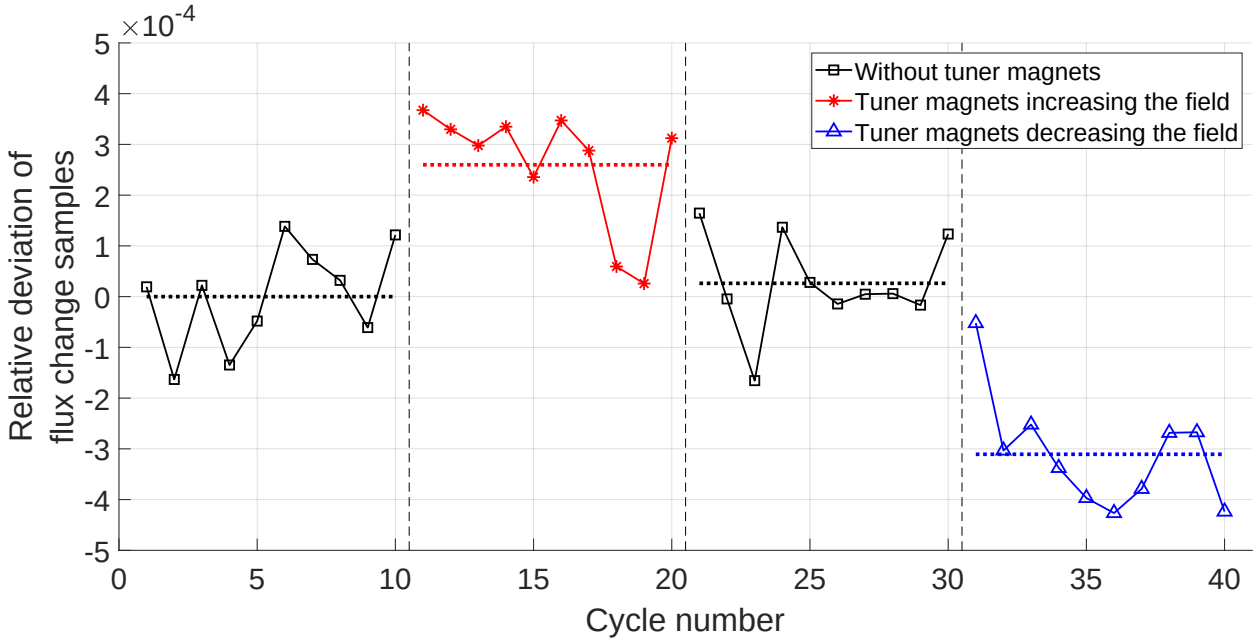

Figure 3.30: Flux change sensitivity measured by performing small field changes with two tuner magnets.

The samples' average with respect to the reference signal (i.e., first set of 10 samples) changed by $+2.6 \times 10^{-4}$ with two tuners increasing the field and -3.1×10^{-4} with two tuners decreasing the field. The third set of samples (also without tuners) showed a relative change of $+2.6 \times 10^{-5}$, being within the random error of the measurement. The changes are larger than the rms variation, which demonstrates local sensitivity for both increasing and decreasing the field. Even for a single slug, the system can detect changes in the order of 10^{-4}, as shown in Fig. 3.31.

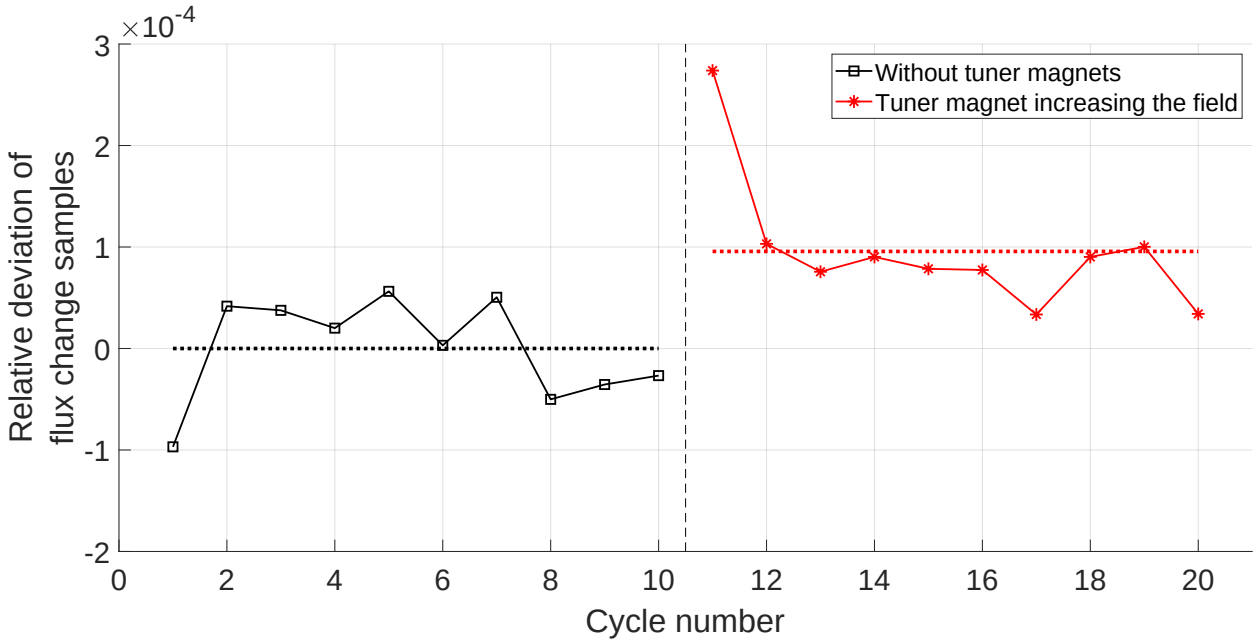

Figure 3.31: Flux change sensitivity measured by performing small field changes with a single tuner magnet.

3.10 Cable Length Tests

Measurements with 20 AWG RG 58A/U coaxial cables (the same cable used in the measurements presented previously) of 30.5, 61, 100, and 200 meters were also performed to evaluate noise issues. For all the cases, the relative error of the measurements was never larger than 6×10^{-5}. It means that the acquisition system can be far away from the undulators and, therefore, a central system may control and measure several undulators at the same time. The combination of many PXIe-4464 modules operating in a PXI crate with an embedded control makes it possible to concentrate the whole system at the same place.

3.11 Chapter Remarks

A novel *in situ* radiation damage detection system for undulators has been proposed, modeled, built, and tested. Its development is based on using a voltmeter to monitor magnetic flux changes on a flexible coil attached to the magnet array. The new approach proved to be capable of measuring field changes with relative resolution on the order of 0.01%. The on-axis peak field and flux change measured for a wide range of gaps have validated the model. It

demonstrates that integrated voltage changes can measure field variations. The next chapter describes a peripheral system design to test voltmeters used to sense magnetic flux changes.

Chapter 4

High-Precision Reference Pulse Generator

Although the profile of the signal depends upon the gap motion features (e.g., speed, acceleration/deceleration rates, position compensation, etc.), integrating the induced voltage makes the flux change dependent only of coil's features, initial gap, and final gap. The system is demonstrably capable of detecting small changes in the integrated voltage changes — better than 10^{-4}, as specified for the LCLS-II project and presented in Chapter 3. Nevertheless, a high-precision reference signal is required to ensure that any measured relative changes in $\Delta\phi$ detected by changes in $\int \varepsilon \, \mathrm{d}t$ with the diagnosis system comes from the reduction of field strength and not due to voltmeter drifts. We designed a circuit for testability that generates a reference signal that has a similar voltage-time area in relation to the typical values from the RDDS. Its design, construction, and characterization are the subject of this chapter[1].

We chose a pulse as the signal's waveform due to the simplicity to specify its features based on the requested output. In principle, only two variables (namely, amplitude and high time[2], as shown in Fig. 4.1) need to be controlled. Disregarding the transients and the electrical noise, the desired time integral of the pulse generated from the verification circuit's output must satisfy

[1]This chapter is an amended version of the following manuscript: J. E. Baader, S. D. Anderson, and Z. R. Wolf, "High-precision reference pulse generator for testing radiation damage in undulators," *IEEE Transactions on Instrumentation and Measurement*, under review.

[2]The literature commonly refers to the amount of time that the pulse is at the high level as *pulse width* or *pulse duration*. Nevertheless, the National Instruments — the company that the voltage acquisition and timer modules applied in this project were purchased — defines the same parameter as *high time* [63], which therefore will be the term used along with this chapter. Similarly, we will use *low time* to represent the amount of time the pulse is at the low level.

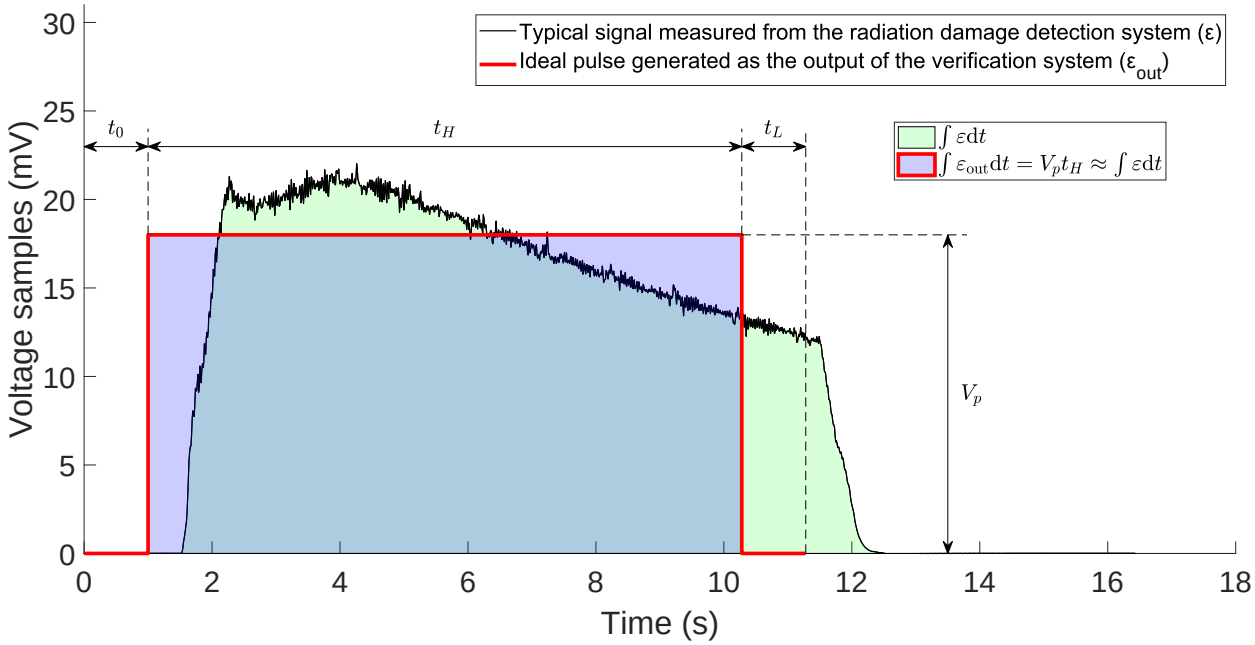

Figure 4.1: Typical signal from the RDDS (ε) and the desired pulse (ε_{out}). Ideally, both signals have approximately the same area of 0.171 Vs and the same time interval of 10 s. The initial delay, the pulse high time and the pulse low time are represented by t_0, t_H, and t_L, respectively.

$$\int \varepsilon_{\text{out}}\, dt = V_p t_H = 0.171\,\text{Vs}, \tag{4.1}$$

where ε_{out} is the output voltage, V_p is the pulse amplitude, and t_H is the high time. Even though a pulse with 17.1 mV of amplitude and 10 s of high time satisfies the 0.171 Vs reference, there are some degrees of freedom to choose V_p and t_H. For instance, once the amplitude is established, fine adjustments on the pulse duration would allow reaching the desired value.

4.1 System Developments

4.1.1 Design

Figure 4.2 shows the schematic of the verification circuit. The fast switch Maxim MAX4544 controls the signal that comes from the low-noise voltage reference Maxim MAX6350 between a positive value (during t_H) and 0 V. The timer module NI PXI-6608 controls the switch and the signal that goes through the common terminal by sending TTL pulses. The switch is considered to be ON when the common terminal is connected to the voltage reference

(the same state shown in Fig. 4.2). Conversely, the switch is OFF when the common terminal is connected to the GND. To adjust the signal's amplitude to the desired amplitude, a passive voltage divider with high precision resistors is used. Table 4.1 shows the electronic components that compose the verification circuit and their main operational characteristics.

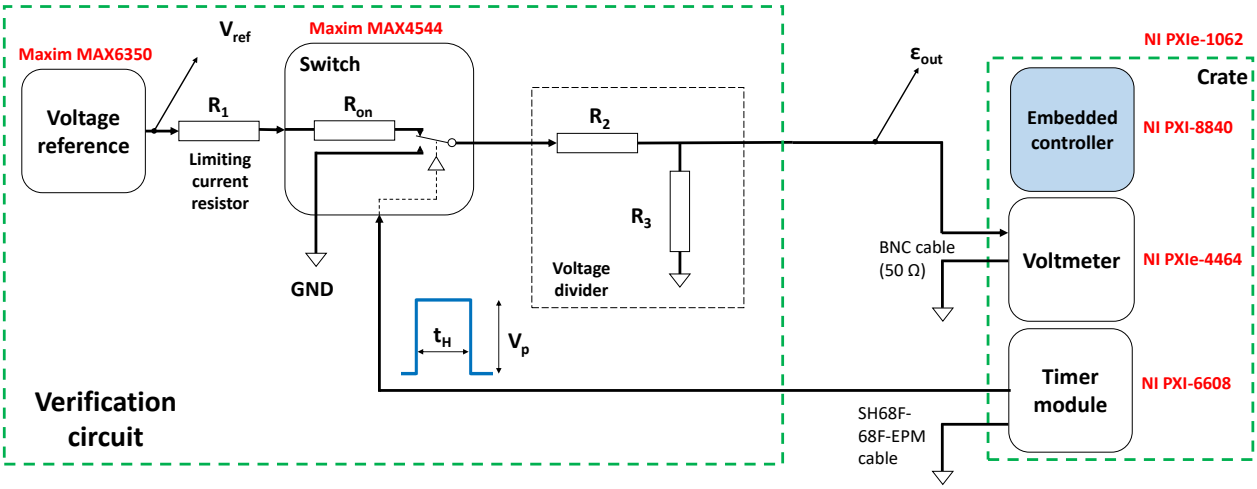

Figure 4.2: Schematic of the verification circuit operation and main components.

The NI PXI-8840 controls both the PXI-6608 and PXIe-4464 modules. The latter is the same voltmeter used to perform the measurements with the RDDS. All these modules were installed in the NI PXIe-1062 crate.

Two low-dropout voltage regulators of 12 V and 9 V LM2940 were used as the power supply for the MAX6350 and MAX4544, respectively. A resistor R_1 was placed between the voltage reference and the switch to limit the current that goes through them. A large value for R_1 significantly reduces V_p, while a small value increases the current, bringing considerable changes to the voltage reference output stability. A resistor $R_1 = 1.5\,\mathrm{k\Omega}$ was chosen to mitigate the issues just mentioned, while resistors $R_2 = 12\,\mathrm{k\Omega}$ and $R_3 = 50\,\Omega$ were selected to guarantee a small output impedance and reduce the signal from 5 V (the voltage reference output) to 18.4 mV, as follows.

The output voltage is

$$\varepsilon_{\mathrm{out}} = \begin{cases} V_p, & \text{if the switch is ON} \\ 0, & \text{if the switch is OFF,} \end{cases} \tag{4.2}$$

where

Table 4.1: List of components and specifications [64–67].

Item	Electronic component	Parameter	Value
Voltage reference	Maxim MAX6350	Output voltage (V_{ref})	5 V
		Output voltage temperature coef.	1 ppm/°C
		Output noise	3 $\mu V_{\text{pk-pk}}$
Switch	Maxim MAX4544 (SPDT)	Turn-on time	25 ns
		Turn-off time	35 ns
		On-resistance (R_{on})	33 Ω (typ), 60 Ω (max)
		On-resistance temp. coef.	approx. ±0.1 Ω/°C
Timer module	NI PXI6608	Oven-controlled crystal oscillator (OCXO) freq.	10 MHz
		Temperature stability	±5 ppb (0 °C - 50 °C)
		Drift in frequency	±0.45 ppm/day
		Base clock accuracy	±200 ppm
Voltage divider and current limiting resistor	Metal Film Resistors	Resistor 1 (R_1)	1.5 kΩ
		Resistor 2 (R_2)	12 kΩ
		Resistor 3 (R_3)	50 Ω
		Tolerance	±0.1%
		Temperature coef.	±5 ppm/°C

$$V_p = \frac{V_{\text{ref}} R_3}{R_1 + R_2 + R_3 + R_{\text{on}}} = 18.4\,\text{mV}. \tag{4.3}$$

Substituting (4.3) in (4.1),

$$t_H = \frac{0.171}{V_p} = 9.3\,\text{s}. \tag{4.4}$$

The output impedance when the switch is ON is

$$Z_{\text{out}} = \frac{R_3(R_1 + R_2 + R_{\text{on}})}{R_3 + (R_1 + R_2 + R_{\text{on}})} = 49.8\,\Omega. \tag{4.5}$$

4.1.2 Error Analysis

From (4.2), the integrated voltage for one single pulse is

$$\Psi = \int_0^{t_T} \varepsilon_{\text{out}}\,\mathrm{d}t = \int_{t_0}^{t_0+t_H} V_p\,\mathrm{d}t, \tag{4.6}$$

where t_0 is the time when the switch changes from OFF to ON and t_T is the total time of the pulse. Equation (4.6) leads to $\Psi = V_p t_H$, the same equation shown in (4.1). Replacing (4.3) in (4.6) and solving the integral:

$$\Psi = \frac{V_{\text{ref}} R_3 t_H}{R_1 + R_2 + R_3 + R_{\text{on}}}. \tag{4.7}$$

The systematic error associated with temperature changes can be calculated from the specifications presented in Section 4.1.1. The room air conditioning system keeps the ambient temperature constant within $\pm 0.5\,^{\circ}\text{C}$ [58]. To guarantee the components were well-selected, a change of $\pm 1\,^{\circ}\text{C}$ was considered. Then, the variation on Ψ was estimated from the expected error on each variable in (4.7) according to the specifications on Table 4.1. By propagating the error [68] and assuming that t_H does not change with temperature,

$$\begin{aligned}\sigma_{\Psi}^2 = &\left(\frac{\partial \Psi}{\partial V_{\text{ref}}}\right)^2 \sigma_{V_{\text{ref}}}^2 + \left(\frac{\partial \Psi}{\partial R_3}\right)^2 \sigma_{R_3}^2 + \left(\frac{\partial \Psi}{\partial t_H}\right)^2 \sigma_{t_H}^2 + \\ &\left(\frac{\partial \Psi}{\partial R_1}\right)^2 \sigma_{R_1}^2 + \left(\frac{\partial \Psi}{\partial R_2}\right)^2 \sigma_{R_2}^2 + \left(\frac{\partial \Psi}{\partial R_{\text{on}}}\right)^2 \sigma_{R_{\text{on}}}^2.\end{aligned} \tag{4.8}$$

Combining (4.7) and (4.8) and representing the estimated result as $\Psi_{\text{est}} = \Psi \pm \sigma_{\Psi}$,

$$\Psi_{\text{est}} = (0.171\,000 \pm 0.000\,002)\,\text{Vs}, \tag{4.9}$$

which corresponds to an error of 12 ppm.

4.1.3 Circuit Layout and Fabrication

Figure 4.3 shows the circuit layout of the verification system based on the schematic of Fig. 4.2. The components and connectors were mounted and soldered on a two-layer laminate FR-4 epoxy glass. Figure 4.4 shows the prototype of the hardware[3].

The board's dimensions are 9.5 cm by 8.6 cm, and the trace width is 0.6 mm. We used a copper ground plane on the backside of the board to improve the signal integrity, accuracy,

[3]The operational amplifier OPA227 was initially set after the voltage divider (at the node ε_{out} in Fig. 4.2) to act as a unity gain buffer. This procedure reduces the circuit output impedance (Z_{out}) and, therefore, makes the circuit independent of the voltmeter input impedance (Z_{in}). However, Z_{in} is at least 20 000 times larger than Z_{out} calculated in (4.5) for the tested voltmeters, so we decided to perform the characterization without the buffer.

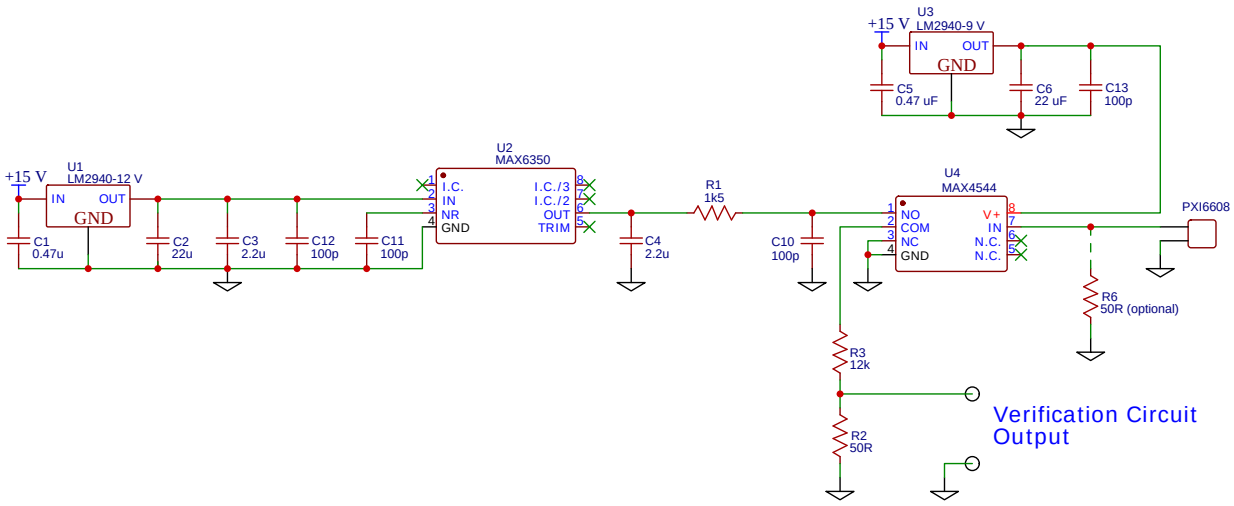

Figure 4.3: Circuit layout of the verification system.

and resistance to interference. Ceramic capacitors of 100 pF were placed near to the integrated circuits' ports, as filters for high-frequency effects and reducing the pulse overshoot.

The I/O connector of the timer module NI PXI-6608 is the 68-pin female SCSI-II which connects to a 68 pine D-dub connector on the board to send the TTL pulses from the PXI-6608 to the MAX4544.

4.1.4 Data Acquisition

Code written in C using LabWindows/CVI software was used to control the TTL pulse sent from the timer module PXI-6608 to the switch MAX4544 and to start and stop the acquisition with the PXIe-4464. A 20 AWG RG 58A/U coaxial cable (the same model mentioned in sections 3.5 and 3.10) of about 1 m connects the output terminal of the circuit to the PXIe-4464. The sampling frequency was set at $f_s = 100\,\text{Hz}$, the same rate used with the RDDS. The TTL pulses used to operate the switch had the initial delay t_0, the high time t_H, and the low time t_L set as 1 s, 9.28 s, and 1 s, respectively. Consequently, the acquisition time was $t_T = 11.28\,\text{s}$, with 1128 voltage samples ($t_T f_s$) being read during one complete pulse generation. The samples taken during the initial delay and low time (in which the circuit's output is, in theory, 0 V) are used to perform offset corrections by using the technique described in Subsection 3.6.2. The program calculates the integrated voltage sample Ψ_s by numerically integrating the voltage through the trapezoidal integration method

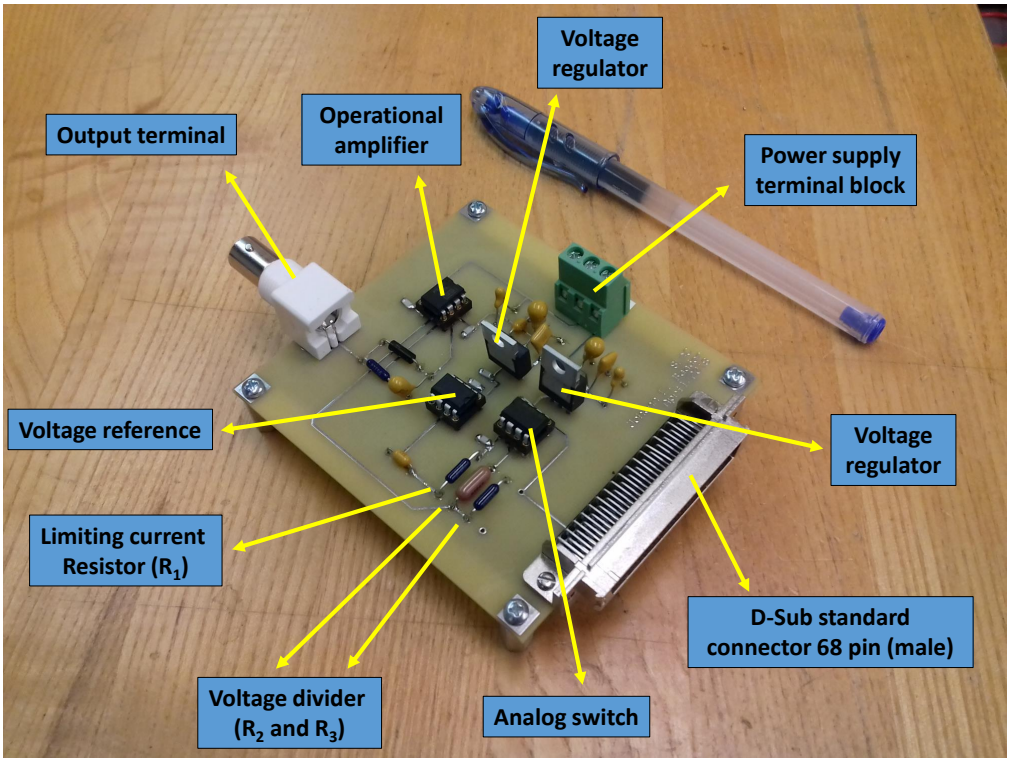

Figure 4.4: Verification circuit hardware prototype.

expressed by

$$\Psi_s = \frac{1}{2f_s}\left|\sum_{i=1}^{t_T f_s}(V_{i+1} + V_i)\right|, \tag{4.10}$$

where V_i is the i-th corrected voltage samples during a single pulse. Notice that we repeat (3.34) here as (4.10) for convenience.

4.2 Circuit Characterization

Two tests were defined to validate the verification circuit:

1. A long-term measurement to confirm the system has a (long-term) precision better than 5×10^{-5} (half of the resolution specified for the RDDS).

2. A reproducibility test to show that turning off all the components and changing the feeding voltage (which would simulate the effects of variations) does not affect the measurements.

The long-term test must have at least 24 h to verify temperature variation periodically. We decided to perform uninterrupted measurements for 38 h. This section presents the results of the validation tests, including the main features of the pulse, as follows.

4.2.1 Pulse Features

Figure 4.5 shows a typical signal from the verification circuit. The amplitude V_p and high time t_H shown in Fig. 4.5a matches with the numbers calculated in (4.3) and (4.4), as expected. Five hundred pulses were generated and measured to evaluate the main features. The overshoot and undershoot were never larger than 9%, and the settling time was always between 20 ms and 60 ms for a tolerance band of 2%. For each measured pulse, we compared the area Ψ_s calculated from (4.10) and the area of an ideal pulse Ψ_i, free of transients. For $\Psi_i = V_p t_H$, the amplitude V_p was measured as the voltage level at the stationary period, while the high time interval t_H was measured as the time separation between the moment that the signal crosses the half of the amplitude. Figure 4.5b presents the same pulse shown in Fig. 4.5a zoomed to show the transients. The red dash-dot line represents the ideal pulse,

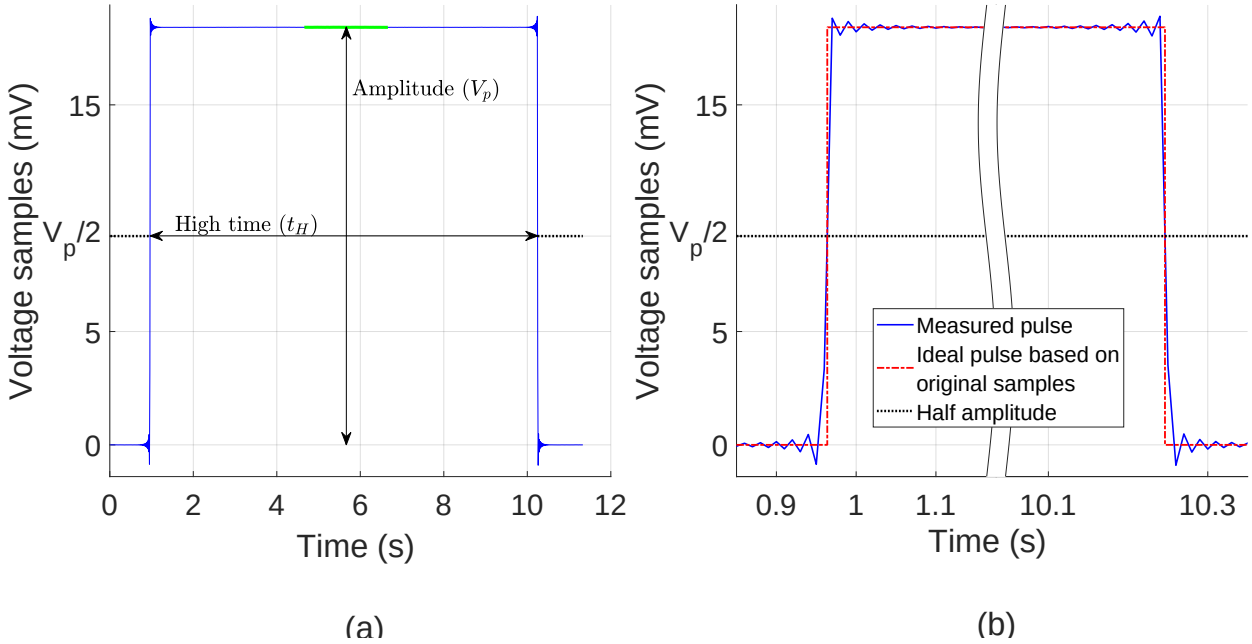

Figure 4.5: Typical pulse generated from the circuit (a) and the transients (b). The amplitude is 18.4 mV, and the high time is 9.3 s. The blue line corresponds to the measured voltage samples. The red dash-dot line represents an ideal pulse defined from the original samples. The black dotted line draws the half amplitude $V_p/2$.

and the black dotted line represents the half amplitude.

The comparison between Ψ_s and Ψ_i allowed us to estimate the influence of the transients. Figure 4.6 shows $|\Psi_s - \Psi_i|$ over 500 samples.

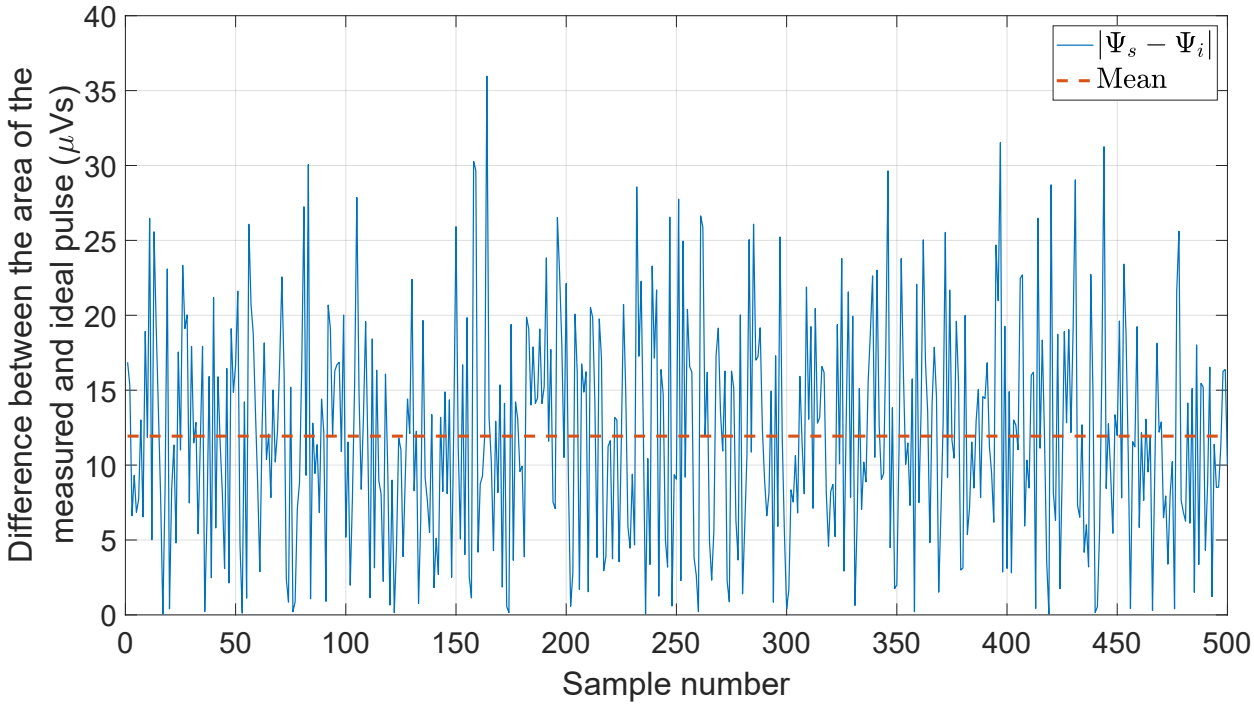

Figure 4.6: Absolute difference between the measured (Ψ_s) and ideal ($\Psi_i = V_p t_H$) voltage integral and its average over 500 samples. V_p and t_H are the amplitude and high time of the measured signal, respectively, being calculated from the voltage samples.

The difference between the area of the measured and the ideal pulse represents an error of approximately 12 µVs (mean), which corresponds to 70 ppm. Given that the overshoot and undershoot amplitude are random, averaging the integrated voltage reduces the error, and will be discussed in the next section.

4.2.2 Long-term Measurements and Statistical Analysis

Figure 4.7 shows the histogram of 8270 samples of integrated voltage from the circuit measured with the PXIe-4464. The bin width h was calculated by using Scott's normal reference rule [69], mathematically expressed as

$$h = \frac{3.5\sigma}{N^{\frac{1}{3}}}, \tag{4.11}$$

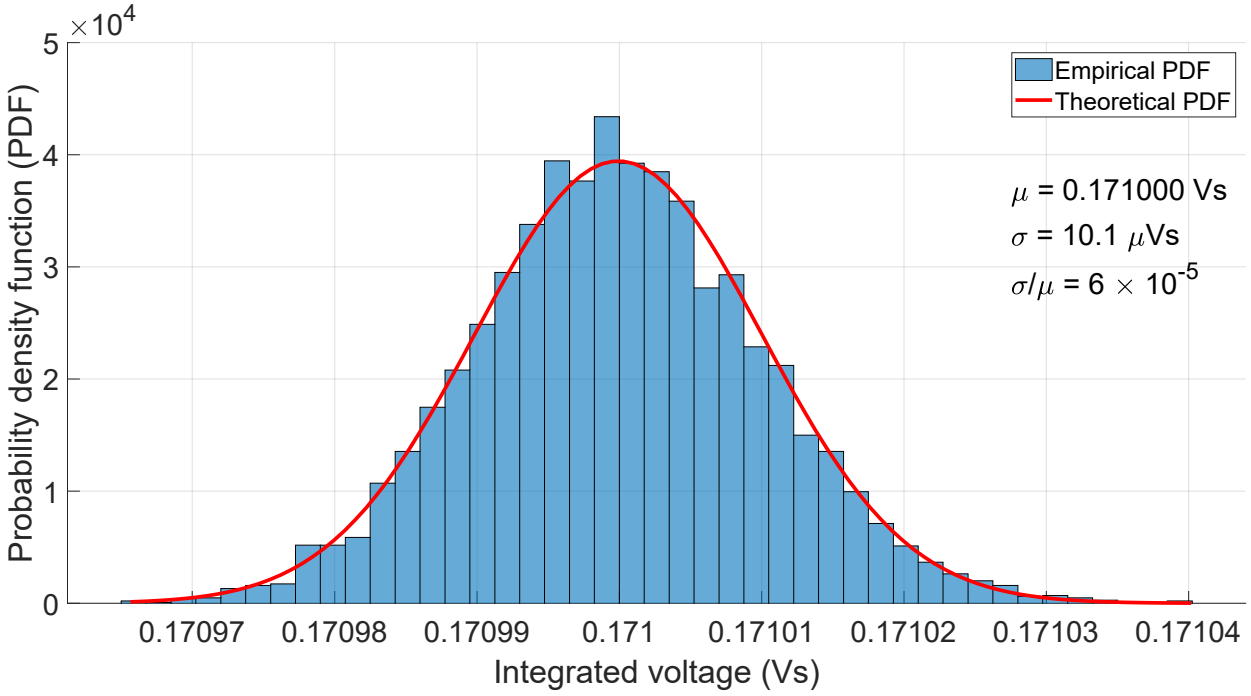

Figure 4.7: Mean, standard deviation, and histogram of 8270 integrated voltage samples taken during approximately 38 hours. The bell-shape line corresponds to a Gaussian distribution plotted from the calculated mean and standard deviation.

where σ is the standard deviation over all the N samples. The similarity between the error measured from the overshoot and undershoot in the previous section, and the error σ estimated from all the samples suggests that the transients are the leading cause of the observed random errors.

The bell shape in Fig. 4.7 corresponds to the plot of a Gaussian probability density function [68], which is given by

$$f(\Psi) = \frac{1}{\sigma\sqrt{2\pi}} e^{-\frac{1}{2}\left(\frac{\Psi-\mu}{\sigma}\right)^2}, \tag{4.12}$$

where μ are the mean over all the samples.

Figure 4.7 suggests that the samples have a Gaussian distribution, as one would expect. The χ^2 test at 5% significance level failed to reject the null hypothesis that the data has a normal distribution. Therefore, we assumed it as a Gaussian.

Let $\Psi_m = \mu_\Psi \pm \sigma_\Psi$ be the representation of a set of n integrated voltage samples (Ψ_s), where μ_Ψ is the average over the samples and σ_Ψ is the standard deviation of the mean. The

parameter σ_Ψ is estimated from the standard deviation over n samples (σ_n) divided by square root of n, or

$$\sigma_\Psi = \frac{\sigma_n}{\sqrt{n}}. \tag{4.13}$$

The relative variation of the measurements, defined by

$$\delta = \frac{\Delta\mu_\Psi}{\mu} = \frac{\mu_\Psi - \mu}{\mu}, \tag{4.14}$$

has to be inside the range of 5×10^{-5}, as we specified. Since the data shows a Gaussian distribution, we express $\Delta\mu_\Psi$ as a constant k times the standard deviation σ_Ψ. Small values of k would exclude many samples, whereas increasing k values would not increase confidence level significantly. For $k = 2.58$, the confidence level is 99%, which is good enough for this application. Using the results shown in Fig. 4.7, $\mu = 0.171\,\text{Vs}$, and $\sigma = 10.1\,\mu\text{Vs}$. Writing δ as a function of n and all the known parameters:

$$\delta = \frac{\Delta\mu_\Psi}{\mu} = \frac{k\sigma_\Psi}{\mu} = \frac{k\sigma}{\mu\sqrt{n}} = \frac{1.524 \times 10^{-4}}{\sqrt{n}}. \tag{4.15}$$

Solving (4.15) for $\delta \leq 5 \times 10^{-5}$ proves that $n \geq 10$ guarantees the required value. Also, increasing the number of samples for averaging does not reduce the relative error significantly. Therefore, one measurement result is represented as the average over 10 integrated voltage samples ($n = 10$). Figure 4.8 shows the long-term measurements during 38 hours.

Most of the data lie within the $(1 \pm \delta) \times \mu$ limit. We associate the systematic error with temperature changes. As expected in theory, the standard deviation of μ_Ψ is $3.48\,\mu\text{Vs}$, approximately $\sqrt{10}$ times lower than $10.1\,\mu\text{Vs}$ shown in Fig. 4.7.

4.2.3 Reproducibility Tests

Three sets of five measurements were performed. The first set established a basis value for comparison. Then, the second set was takes after shutting down all the equipment and waiting for 1 hour. Finally, we changed the circuit power supply voltage from 15 V to 14 V and took an additional set of data. Figure 4.9 presents the results.

No significant differences among the measurements were observed. Furthermore, the samples fell into the limit defined by $\delta = 5 \times 10^{-5}$ in relation to the reference $\mu = 0.171\,\text{Vs}$.

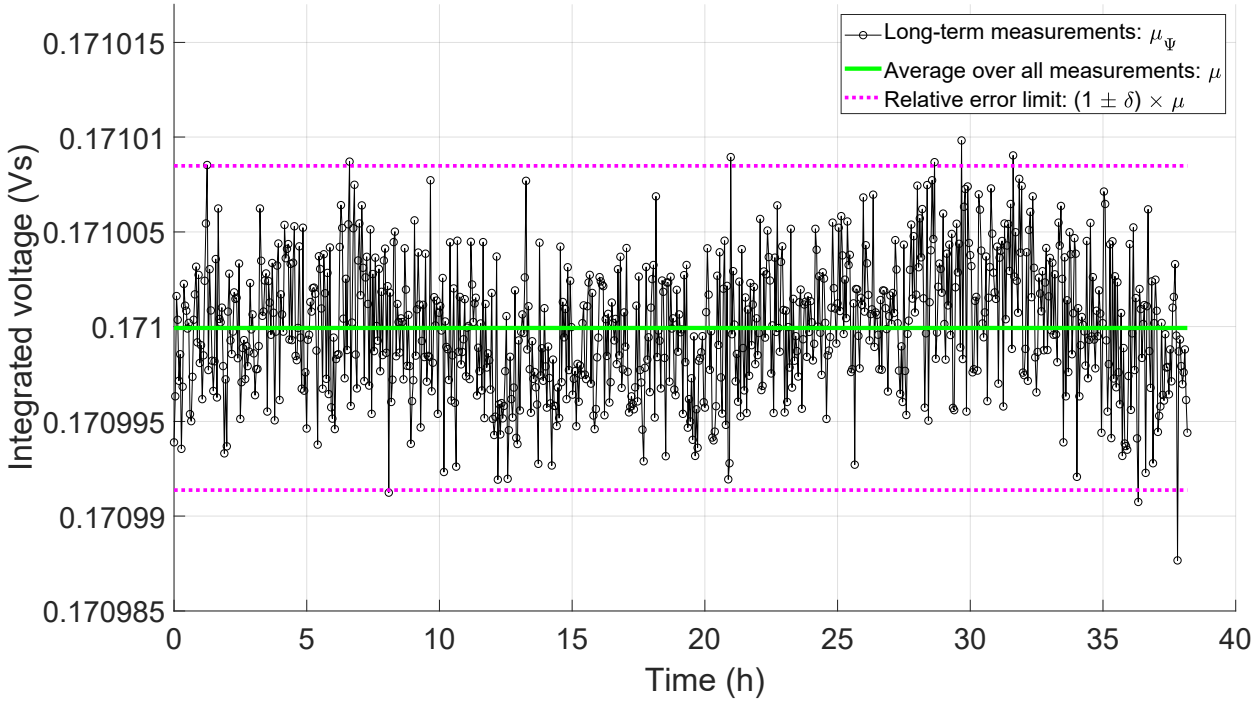

Figure 4.8: Long-term measurements over time showing the random and systematic errors. We assume that the latter occurs due to temperature variations. Nevertheless, almost all the results fall into the $(1 \pm \delta) \times \mu$ boundaries.

Figure 4.9 expresses the reference as Ψ_{ref}. This result shows the integrated pulse is unaffected by turning off the circuit or by changing the power supply up to 1 V. The latter demonstrates that the circuit's stability is unaffected by small variations on the power supply.

The error bars amplitude were calculated by dividing the standard deviation over 10 samples of one measurement by $\sqrt{10}$ [68]. For the results shown in Fig. 4.9, the standard deviation varied from 1.8 µVs to 4.3 µVs.

4.2.4 Comparison between the PXIe-4464 and HP 3458

Because of the differences between the PXIe-4464 and HP 3458 accuracy, the relative error of the voltage-time integral measured with these ADCs may be higher than 5×10^{-5}. However, the primary purpose of the circuit is to verify whether a specific voltmeter integral voltage measurement has changed more than 5×10^{-5}. The results presented in the last two sections show that the circuit has high repeatability.

To compare the variation of the signal between a set of measurements with two different

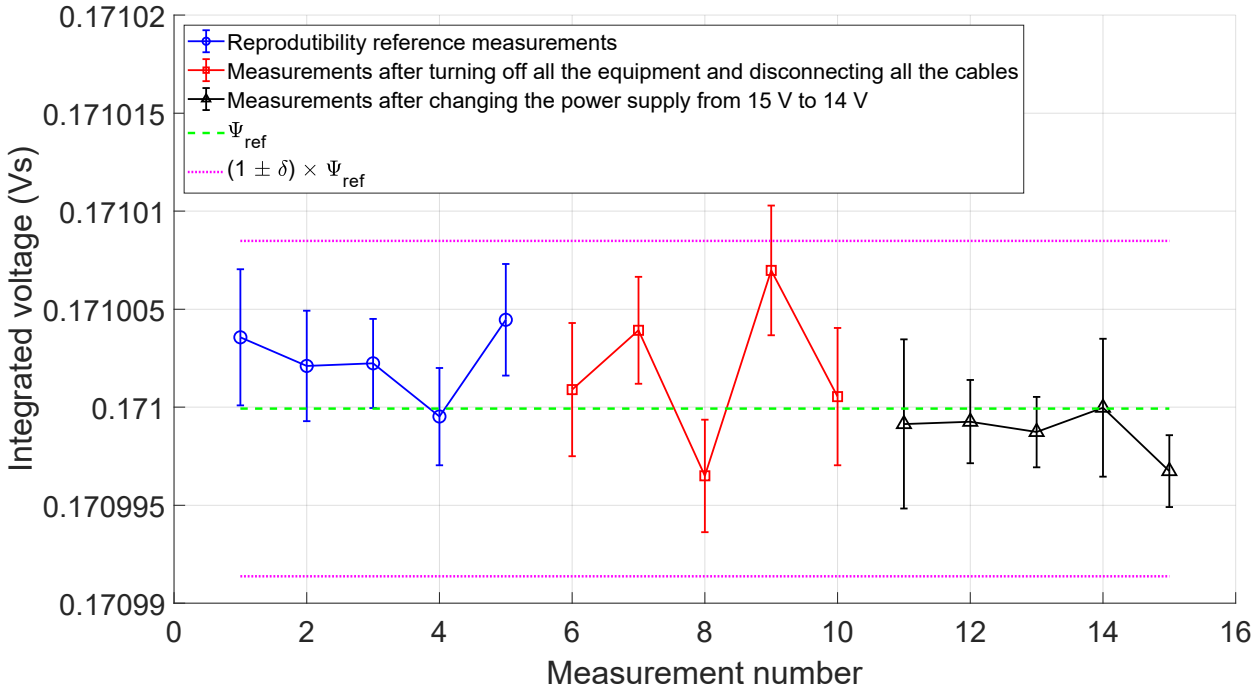

Figure 4.9: Reproducibility tests. First, five measurements were taken to establish a reference (blue). Then, the voltmeter and the circuit were turned off. After 1 hour, both were turned on again, and five new measurements were performed (red). Finally, the third set of five measurements were obtained, this time with the circuit's power supply at 14 V instead of 15 V.

voltmeters, we subtracted the average from each set — a process called *demeaning* — which results in data with zero-mean and allows comparing variation. Figure 4.10 contrasts the differences in the integrated voltage measured ten times with both the PXIe-4464 and the HP 3458.

The HP 3458 has normal mode rejection for 60 Hz noise, which is not possible to set on the PXIe-4464. Thus, we believe that most of the random errors observed in the previous results with the PXIe-4464 (figures 4.8, 4.9, and 4.10) come from non-filtered noise from power line. The standard deviation of the measurements with the HP 3458 depicted in Fig. 4.10 was six times lower than with the PXIe-4464.

4.3 Hypothesis Test

If the RDDS detects a variation of the integrated voltage larger than 100 ppm, the verification circuit performs a double-check test. In this section, we propose how to test the

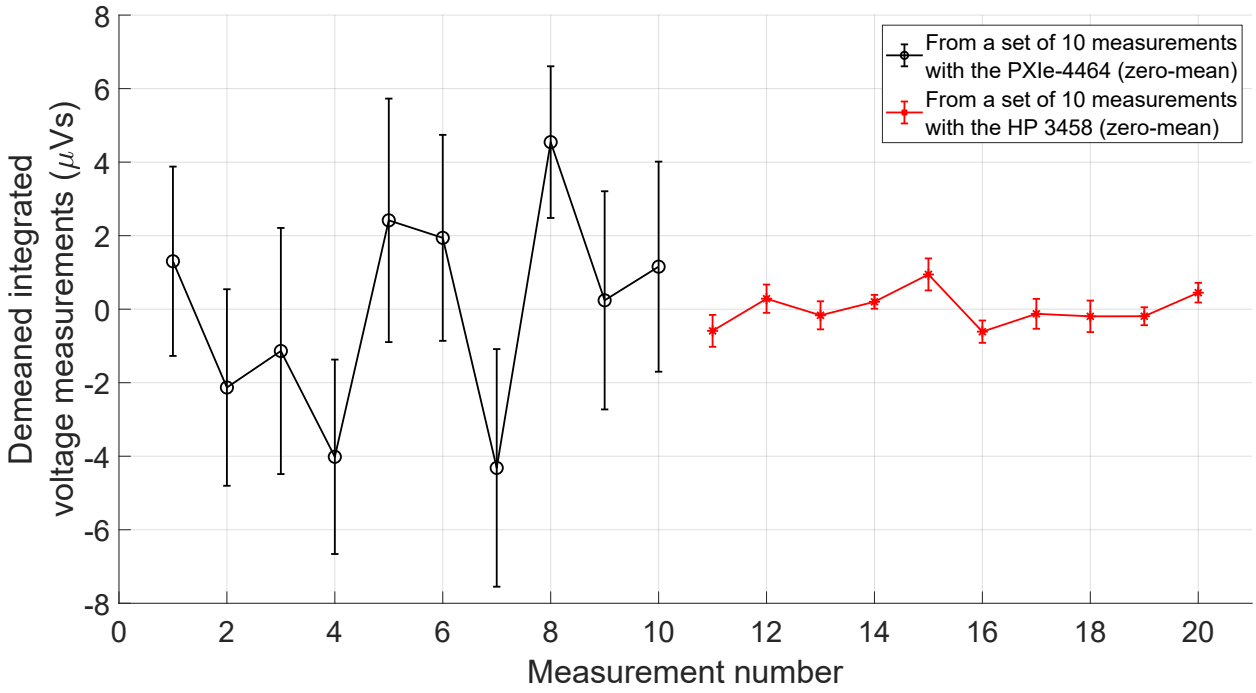

Figure 4.10: Comparison between the PXIe-4464 and HP 3458 stability.

hypothesis that the voltmeter used along with the RDDS changed the signal (and not a damaged undulator). The test consists of measuring the signal from the verification system a few times, according to the confidence we would like to have and the available time. Let define the null and alternative hypothesis as follow:

- *Null Hypothesis (H_0)*: the voltmeter changed the result less or equal than maximum relative variation δ_{lim}. Therefore, it measures properly.
- *Alternative Hypothesis (H_a)*: the voltmeter changed the result more than the maximum relative variation δ_{lim}. Therefore, it does not measure properly.

Considering $\delta_{\text{lim}} \geq 0$, we express those statements as:

- H_0: $|\delta| \leq \delta_{\text{lim}}$
- H_a: $|\delta| > \delta_{\text{lim}}$

Let the number of measurements be n_m. For less than 30 measurements ($n_m < 30$), the one-tailed t-student test might be applied to test the hypothesis. According to the variable we defined and by definition of Student's t distribution [70]:

$$t = \frac{|\delta| - \delta_{\text{lim}}}{S/\sqrt{n_m}}, \tag{4.16}$$

where S is the standard deviation of $|\delta|$. We reject the hypothesis H_0 and accept H_a when $t > t_{\alpha,n_m-1}$, where α is the significance level and $n-1$ is the number of degrees of freedom; when $t \leq t_{\alpha,n_m-1}$, we fail to reject H_0 and, therefore, we accept it as true. In other words, if

$$\frac{|\delta| - \delta_{\text{lim}}}{S/\sqrt{n_m}} \geq t_{\alpha,n_m-1}, \tag{4.17}$$

then we assume that the voltmeter changed the gain more than the threshold.

By manipulating $|\delta|$, it is possible to demonstrate that its standard deviation is

$$S = \frac{\sigma_\Psi}{\Psi_{\text{ref}}}. \tag{4.18}$$

Replacing (4.18) and (4.14) in (4.17) and manipulating the inequality,

$$\frac{|\mu_\Psi - \Psi_{\text{ref}}|}{\Psi_{\text{ref}}} \geq t_{\alpha,n_m-1}\frac{\sigma_\Psi}{\Psi_{\text{ref}}\sqrt{n_m}} + \delta_{\text{lim}}. \tag{4.19}$$

In summary, if (4.19) is satisfied, then we assume that the voltmeter does not measure within the required precision.

4.4 Chapter Remarks

A verification circuit capable of generating a high-precision reference pulse has been designed, built, and tested. The reference of 0.171 Vs was established based on the initial tests with the novel *in situ* RDDS presented in Chapter 3. Long-term measurements allowed statistical analysis and showed that averaging a few samples allows reaching a relative precision better than 5×10^{-5}. Moreover, reproducibility tests confirmed that the circuit's output is invariable under small power supply instabilities and equipment shutdown.

Chapter 5

Concluding Remarks and Perspectives

We successfully designed, built and tested a novel *in situ* radiation damage diagnostic system capable of detecting field changes with relative resolution and precision — considered the leading figures of merit — better than 0.01% (100 ppm), being comparable to techniques available in dedicated measurements facilities, such as Hall probes and induction sensors. Tuners reproduced local field changes around 3 mT, which have been detected by the system. The complete system would take less than 10 minutes to perform flux change measurements during the beam shuts-off if one flexible coil is set for each undulator simultaneously. The data acquisition and analysis are straightforward.

Long-term runs proved the high repeatability, even in an environment with temperature changes higher than 0.5 °C. The magnet array temperature oscillated within ±0.1 °C and is considered the primary source of error. For the LCLS-II, local room temperature stability must fall within ±0.1 °C, hence the strongback temperature variation and errors related to temperature changes would be presumably smaller.

As opposed to the beam-based techniques, this thesis presents the approach to monitor field changes in undulators based on local magnetic flux measurements. The new technique does not require full access to the control systems, but rather only the undulator gap. On the other hand, because the coil is fixed to the undulator, relative K-value changes based on vertical/horizontal positioning may not be deduced. Consequently, the proposed technique is not suitable for alignment purposes as beam-based measurements are.

The effective area of the flexible coil depends, among many variables, of the number on layers, which is the most effective way to increase the system's sensitivity, if necessary.

The tiny thickness of the board allows stacking up more layers without increasing the coil's thickness significantly. The number of coil segments and windings per pole also increases sensitivity, although the former might make the coil unnecessarily longer, while the latter would increase costs to produce the board.

Even though the flexible coil has been tested using hybrid undulators in the context of the LCLS-II developments, its principles work for any planar variable gap undulator. Fixed gap undulators have a constant magnetic field, therefore a different approach must be used to evaluate magnetic field quality in such devices. For instance, a coil attached to the beam pipe could measure flux change when the undulator is horizontally displaced by making use of the common "roll-away" capabilities. Another option is to develop a system that moves a few segments of the coil along the longitudinal axis in a reproducible way and integrates the induced voltage. It should be mentioned, however, that most of FEL facilities in operation or under construction will install variable gap undulators systems since they enable tuning of the photon beam properties.

For the initial tests, the coil was attached to the undulator with Kapton tape covering its whole extent. For real operation, a different approach to firmly fixing the coil to the undulator magnet array needs to be explored. The board of the coil covers a fraction of the magnet array length, given that its extension monitors 30 poles, whereas the SXR undulator has 174 poles. The number of coil segments is justified by the fact that most of the radiation damage is likely to occur in a limited region of the undulator length. It means, however, that the RDDS only detects field changes confined to the region where the coil is attached.

The position of the coil in the undulator was irrelevant during the testing stage. During operation in LCLS-II, the coil will be placed near the upstream end, where we expect the most substantial radiation damage. So far, simulations have demonstrated that a relative resolution of 10^{-4} of the RDDS detects smaller relative changes in the effective K-parameter (K_{eff}) — indeed, the desired characteristic — although they also have suggested that a straightforward connection between the measured flux change (ψ) and K_{eff} is challenging to accomplish. Further studies must be carried in the future to evaluate the coil's features (e.g., radiation-resistance and stability) and the relationship between photon beam characteristics and relative changes detected with the RDDS over the years under the LCLS-II operation.

A high precision verification system designed for testability generates electrical pulses on the same order of the signal generated from the radiation damage detection system (roughly 0.171 Vs) with relative precision better than 50 ppm. We expect to test the verification circuit along with the RDDS in the LCLS-II, aiming to verify whether long-term component failures are likely to occur.

The results are encouraging: The proposed RDDS lays the groundwork for developing *in situ* magnetic measurement techniques to detect radiation damage in variable-gap permanent-magnet undulators during real operation. Additionally, the proposed verification system is suitable for testing purposes on instruments and applications designed to quantify the magnetic field by integrating voltage signals, as commonly used in induction sensors techniques, such as harmonic coil, stretch wire, and flip coil systems.

Bibliography

[1] C. Bostedt *et al.*, "Linac coherent light source: The first five years," *Rev. Mod. Phys.*, vol. 88, p. 015007, Mar. 2016.

[2] H. Onuki and P. Elleaume, *Undulators, Wigglers and Their Applications*. Abingdon, UK: Taylor & Francis, 2003.

[3] M. Couprie, "Panorama of new generation of accelerator based short wavelength coherent light sources," *Nuclear Instruments and Methods in Physics Research Section B: Beam Interactions with Materials and Atoms*, vol. 364, pp. 4 – 15, Aug. 2015.

[4] J. A. Clarke, *The Science and Technology of Undulators and Wigglers*. Oxford University Press, Jul. 2004.

[5] J. Pflueger, "Undulator technology," *CERN Yellow Reports: School Proceedings*, vol. 1, no. 0, p. 55, 2018. [Online]. Available: https://publishing.cern.ch/index.php/CYRSP/article/view/388

[6] M. Petra, P. D. Hartog, E. Moog, S. Sasaki, N. Sereno, and I. Vasserman, "Radiation effects studies at the Advanced Photon Source," in *Proc. 24th International Conference and 9th FEL Users Workshop*, Argonne, Illinois, USA, Sep. 2002, pp. 422–425.

[7] M. Tischer, P. Neumann, A. Schöps, and P. Vagin, "Refurbishment of radiation-damaged undulators," in *Proc. 12th International Conference On Synchrotron Radiation Instrumentation*, New York, NY, USA, Jul. 2016, p. 020022.

[8] J. Skupin, Y. Li, J. Pflüger, B. Faatz, and T. Vielitz, "Undulator demagnetization due to radiation losses at FLASH," in *Proc. 11th European Particle Accelerator Conference (EPAC08)*, Genoa, Italy, Jun. 2008, pp. 2308–2310.

[9] T. Bizen, R. Kinjo, T. Hasegawa, A. Kagamihata, Y. Kida, T. Seike, T. Watanabe, T. Hara, T. Itoga, Y. Asano *et al.*, "Radiation-induced magnetization reversal causing a large flux loss in undulator permanent magnets," *Scientific Reports*, vol. 6, Nov. 2016.

[10] F. Wolff-Fabris, J. Pflueger, F. Schmidt-Foehre, and F. Hellberg, "Status of radiation damage on the European XFEL undulator systems," *Journal of Physics Conference Series*, vol. 1067, p. 032025, Sep. 2018.

[11] H. Nuhn, C. Field, S. Mao, Y. Levashov, M. Santana, J. Welch, and Z. Wolf, "Undulator radiation damage experience at LCLS," in *Proc. 36th International Free Electron Laser Conference (FEL'14)*, Basel, Switzerland, Aug. 2014, pp. 127–130.

[12] Z. Li, Y. Jia, R. Liu, Y. Xu, G. Wang, and X. Xia, "Investigation on demagnetization of nd2fe14b permanent magnets induced by irradiation," *Nuclear Instruments and Methods in Physics Research Section B Beam Interactions with Materials and Atoms*, vol. 413, pp. 68 – 74, Dec. 2017.

[13] C. Chen, J. Talnagi, J. Liu, P. Vora, A. Higgins, and S. Liu, "The effect of neutron irradiation on Nd-Fe-B and Sm2Co17-based high-temperature magnets," *IEEE Transactions on Magnetics*, vol. 41, no. 10, pp. 3832–3834, Oct. 2005.

[14] J. Alderman, P. Job, R. Martin, C. Simmons, and G. Owen, "Measurement of radiation-induced demagnetization of Nd-Fe-B permanent magnets," *Nuclear Instruments and Methods in Physics Research Section A Accelerators Spectrometers Detectors and Associated Equipment*, vol. 481, no. 1-3, pp. 9–28, Apr. 2002.

[15] K. Boockmann, M. Liehr, W. Rodewald, E. Salzborn, M. Schlapp, and B. Wall, "oioioi," *Journal of Magnetism and Magnetic Materials*, vol. 101, no. 1-3, pp. 345–346, Oct. 1991.

[16] R. Gao, L. Zhen, G. Li, C. Xu, and W. Shao, "Effect of γ-ray irradiation on the magnetic properties of NdFeB and Fe-Cr-Co permanent magnets," *Journal of Magnetism and Magnetic Materials*, vol. 302, no. 1, pp. 156–159, Jul. 2006.

[17] R. Gao, L. Zhen, W. Shao, X. Hao, X. Sun, L. Yang, and B. Wang, "Study of γ-ray irradiation effect on permanent magnets."

[18] S. Okuda, K. Ohashi, and N. Kobayashi, "Effects of electron-beam and γ-ray irradiation on the magnetic flux of Nd-Fe-B and Sm-Co permanent magnets," *Nuclear Instruments and Methods in Physics Research Section B Beam Interactions with Materials and Atoms*, vol. 94, no. 3, pp. 227–230, Nov. 1994.

[19] A. B. Temnykh, "Measurement of NdFeB permanent magnets demagnetization induced by high energy electron radiation," *Nuclear Instruments and Methods in Physics Research Section A Accelerators Spectrometers Detectors and Associated Equipment*, vol. 587, no. 1, pp. 13–19, Mar. 2008.

[20] M. Balaji, M. M. Raja, K. Asokan, D. Kanjilal, T. Rajasekaran, and D. Pathinettam Padiyan, "Effect of thermal spike energy created in CuFe2O4 by 150MeV Ni11+ swift heavy ion irradiation," *Nuclear Instruments and Methods in Physics Research Section B Beam Interactions with Materials and Atoms*, vol. 269, no. 10, pp. 1088–1093, May. 2011.

[21] H. B. Luna, X. K. Maruyama, N. J. Colella, J. S. Hobbs, R. S. Hornady, B. Kulke, and J. V. Palomar, "Bremsstrahlung radiation effects in rare earth permanent magnets," *Nuclear Instruments and Methods in Physics Research Section A Accelerators Spectrometers Detectors and Associated Equipment*, vol. 285, no. 1-2, pp. 349–354, Dec. 1989.

[22] O. P. Kahkonen, S. Makinen, M. Talvitie, and M. Manninen, "Radiation damage in Nd-Fe-B magnets: temperature and shape effects," *Journal of Physics Condensed Matter*, vol. 4, no. 4, pp. 1007–1014, Jan. 1992.

[23] T. Bizen, T. Tanaka, Y. Asano, D. Kim, J. Bak, H. Lee, and H. Kitamura, "Demagnetization of undulator magnets irradiated high energy electrons," *Nuclear Instruments*

and Methods in Physics Research Section A Accelerators Spectrometers Detectors and Associated Equipment, vol. 467-468, pp. 185–189, Jul. 2001.

[24] B. Yang, "High-resolution undulator measurements using angle-integrated spontaneous radiation," in *Proc. 2005 Particle Accelerator Conference (PAC'05)*, Knoxville, Tennessee, USA, May 2005, pp. 2342–2344.

[25] J. Welch, J. Arthur, P. Emma, J. Hastings, Z. Huang, H. Nuhn, P. Stefan, R. Bionta, R. Dejus, B. Yang *et al.*, "Precision measurement of the undulator K parameter using spontaneous radiation," in *Proc. 28th International Free Electron Laser Conference (FEL'06)*, Berlin, Germany, Aug. 2006, pp. 548–551.

[26] J. Welch, A. Brachmann, F. Decker, Y. Ding, P. Emma, A. Fisher, J. Frisch, Z. Huang, R. Iverson, H. Loos *et al.*, "Undulator K-parameter measurements at LCLS," in *Proc. 31st International Free Electron Laser Conference (FEL'09)*, Liverpool, UK, Aug. 2009, pp. 730–733.

[27] W. Freund, L. Fröhlich, S. Karabekyan, A. Koch, J. Liu, D. Nölle, J. Wilgen, and J. Grünert, "First measurements with the K-monochromator at the European XFEL," *Journal of Synchrotron Radiation*, vol. 26, no. 4, pp. 1037–1044, Jul. 2019.

[28] L. Bottura and K. N. Henrichsen, "Field measurements," in *Proc. CERN Accelerator School on Superconductivity and Cryogenics for Accelerators and Detectors*, Erice, Italy, May 2002, pp. 118 – 148.

[29] B. D. Brachmann, "LCLS-II - Status and upgrades," in *Proc. 39th International Free Electron Laser Conference 2019 (FEL'19)*, Hamburg, Germany, Sep. 2019.

[30] X. Wang, C. Feng, C.-Y. Tsai, L. Zeng, and Z. Zhao, "Obliquely incident laser and electron beam interaction in an undulator," *Phys. Rev. Accel. Beams*, vol. 22, p. 070701, Jul. 2019. [Online]. Available: https://link.aps.org/doi/10.1103/PhysRevAccelBeams.22.070701

[31] R. P. Walker, "Wigglers," in *Proc. CERN Accelerator School on 5th Advanced Accelerator Physics Course*, Rhode, Grece, Nov. 1995, pp. 807–836.

[32] K. Wille, "Introduction to insertion devices," in *Proc. CERN Accelerator School on Synchrotron Radiation and Free Electron Lasers*, Grenoble, France, Aug. 1998, pp. 61 – 76.

[33] A. Hofmann, "Characteristics of synchrotron radiation," in *Proc. CERN Accelerator School on Synchrotron Radiation and Free Electron Lasers*, Grenoble, France, Aug. 1998, pp. 1–44.

[34] Z. Wolf, "Introduction to LCLS undulator tuning," SLAC, Menlo Park, CA, USA, Tech. Rep. LCLS-TN-04-7, Jun. 2004.

[35] J. D. Jackson, *Classical electrodynamics; 3rd ed.* New York, NY: Wiley, 1998.

[36] R. J. Dejus, I. Vasserman, S. Sasaki, and E. Moog, "Undulator a magnetic properties and spectral performance," Argonne National Laboratory, Argonne, Illinois, Tech. Rep. ANL/APS/TB-45, May 2002.

[37] K. Halbach, "Permanent magnet undulators," *Le Journal de Physique Colloques*, vol. 44, no. C1, pp. C1–211–C1–216, Feb. 1983.

[38] ANL, "7-GeV advanced photon source: conceptual design report," Argonne National Laboratory, Chicago, Illinois, USA, Tech. Rep. ANL-87-15, Apr. 1987.

[39] P. Elleaume, J. Chavanne, and B. Faatz, "Design considerations for a 1Å SASE undulator," *Nuclear Instruments and Methods in Physics Research Section A: Accelerators, Spectrometers, Detectors and Associated Equipment*, vol. 455, no. 3, pp. 503 – 523, Dec. 2000.

[40] R. Dejus, M. Jaski, and S. Kim, "On-axis brilliance and power of in-vacuum undulators for the Advanced Photon Source," Argonne National Laboratory, Illinois, USA, Tech. Rep. MD-TN-2009-004, Nov. 2009.

[41] E. R. Moog, R. J. Dejus, and S. Sasaki, "Comparison of achievable magnetic fields with superconducting and cryogenic permanent magnet undulators - a comprehensive study of computed and measured values," no. ANL/APS/LS-348, Jan. 2017.

[42] J. Bahrdt and E. Gluskin, "Cryogenic permanent magnet and superconducting undulators," *Nuclear Instruments and Methods in Physics Research Section A: Accelerators, Spectrometers, Detectors and Associated Equipment*, vol. 907, pp. 149 – 168, Nov. 2018.

[43] P. Emma *et al.*, "First lasing and operation of an ångstrom-wavelength free-electron laser," *Nature Photon.*, vol. 4, no. 9, pp. 641–647, Sep. 2010.

[44] "LCLS Beam Based Undulator K Measurement Workshop," https://www-ssrl.slac.stanford.edu/lcls/undulator/meetings/2005-11-14{_}bbkm{_}workshop/, SLAC, Menlo Park, CA, USA, Nov. 2005, Accessed: 2019-04-11.

[45] I. Vasserman, R. Dejus, P. Den Hartog, E. Moog, S. Sasaki, E. Trakhtenberg, M. White *et al.*, "LCLS undulator design development," in *Proc. 26th International Free Electron Laser Conference (FEL'04)*, Trieste, Italy, Aug. 2004, pp. 367–370.

[46] H. Loos *et al.*, "LCLS beam diagnostics," Monterey, CA, USA, Apr. 2015.

[47] M. Altarelli *et al.*, "The European X-Ray Free-Electron Laser. Technical design report," European XFEL, Hamburg, Germany, Tech. Rep. DESY 2006-097, Jul. 2007.

[48] J. Galayda, "The LCLS-II: A high power upgrade to the LCLS," in *Proc. 9th International Particle Accelerator Conference (IPAC 2018)*, Vancouver, BC Canada, Apr. 2018, pp. 18–23.

[49] J. Stohr, "Linac Coherent Light Source II (LCLS-II) Conceptual Design Report," SLAC, Menlo Park, CA, USA, Tech. Rep. SLAC-R-978, Nov. 2011.

[50] "LCLS-II Final Design Report," SLAC, Menlo Park, CA, USA, Tech. Rep. LCLSII-1.1-DR-0251-R0, Nov. 2015.

[51] M. Leitner *et al.*, "Hard X-ray and soft X-ray undulator segments for the Linear Coherent Light Source upgrade (LCLS-II) project," in *Proc. 8th International Particle Accelerator Conference (IPAC 2017)*, Copenhagen, Denmark, May 2017, pp. 1605–1608.

[52] H.-D. Nuhn, "LCLS-II undulator system physics requirements," SLAC, Menlo Park, CA, USA, Tech. Rep. LCLSII-3.2-PR-0038-R3, Jun. 2017.

[53] J. E. Baader, S. D. Anderson, and Z. R. Wolf, "A novel in-situ radiation damage diagnostic system for undulators," *IEEE Transactions on Instrumentation and Measurement*, in press, doi: 10.1109/TIM.2019.2936715.

[54] D. J. Hamman and C. L. Hanks, "Radiation effects design handbook. Section 3 - Electrical insulating materials and capacitors," NASA, Washington, USA, Tech. Rep. NASA-CR-1787, Jul. 1971.

[55] L. McKeen, "6 - polyimides," in *The Effect of Sterilization on Plastics and Elastomers*, 3rd ed., ser. Plastics Design Library. Boston, MA, USA: William Andrew Publishing, 2012, pp. 169 – 182.

[56] K. Bertsche, J. . Ostiguy, and W. B. Foster, "Temperature considerations in the design of a permanent magnet storage ring," in *Proc. 1995 Particle Accelerator Conference (PAC'95)*, Dallas, TX, USA, May. 1995, pp. 1381–1383.

[57] S. H. Kim and C. Doose, "Temperature compensation of NdFeB permanent magnets," in *Proc. 1997 Particle Accelerator Conference (PAC'97)*, Vancouver, BC, Canada, May. 1997, pp. 3227–3229.

[58] Z. Wolf and R. Ruland, "Requirements for the construction of the LCLS magnetic measurements laboratory," SLAC, Menlo Park, CA, USA, Tech. Rep. LCLS-TN-04-1, Feb. 2004.

[59] "3M^{TM} Scotch-Weld^{TM} Epoxy Adhesive 1838 B/A Green Product Specifications," https://3m.citrination.com/pif/000153?locale=en-US, Accessed: 2019-11-13.

[60] K. Lauer, Y. Levashov, K. McCombs, H.-D. Nuhn, E. Wallén, S. Marks, B. McKee, C. Andrews, J.-Y. Jung, K. Ray *et al.*, "LCLS-II undulator motion control," in *Proc. 16th International Conference on Accelerator and Large Experimental Physics Control Systems*, Barcelona, Spain, Oct. 2017, pp. 1379–1383.

[61] M. Leitner, C. Andrews, D. Arbelaez, A. Band, D. Bianculli, A. Brown, D. Bruch, A. Callen, J. Corlett, A. DeMello *et al.*, "Hard X-Ray and Soft X-Ray Undulator Segments for the Linear Coherent Light Source Upgrade (LCLS-II) Project," in *Proc. 8th*

International Particle Accelerator Conference (IPAC'17), Copenhagen, Denmark, May. 2017, pp. 1605–1608.

[62] J. Jung, A. Black, and S. Marks, "Magnetic Tuner For HXU-32," LBNL, Berkeley, CA, USA, Tech. Rep. LC0100-10994, 2017.

[63] "Generating Pulses," http://zone.ni.com/reference/en-XX/help/370466AH-01/daqhelp/generating_pulses/, Accessed: 2020-02-10.

[64] *1ppm/°C, Low-Noise, +2.5V/+4.096V/+5V Voltage References*, MAX6350, Maxim Integrated, CA, USA, 2007, Rev 1. [Online]. Available: https://datasheets.maximintegrated.com/en/ds/MAX6325-MAX6350.pdf

[65] *Low-Voltage, Single-Supply Dual SPST/SPDT Analog Switches*, MAX4544, Maxim Integrated, CA, USA, 2007, Rev 4. [Online]. Available: https://datasheets.maximintegrated.com/en/ds/MAX4541-MAX4544.pdf

[66] *NI 660x Specifications*, PXI-6608, National Instruments, CA, USA, 2009, Doc. Numb. 372141B-01. [Online]. Available: http://www.ni.com/pdf/manuals/372141b.pdf

[67] *Metal Film Resistors, Axial, High Precision, High Stability*, PTF65, Vishay Dale, 2016, Doc. Numb. 31019. [Online]. Available: https://br.mouser.com/datasheet/2/427/ptf-239718.pdf

[68] J. Taylor, *Introduction to error analysis, the study of uncertainties in physical measurements*, 1997.

[69] D. W. Scott, "Scott's rule," *Wiley Interdisciplinary Reviews: Computational Statistics*, vol. 2, no. 4, pp. 497–502, 2010. [Online]. Available: https://onlinelibrary.wiley.com/doi/abs/10.1002/wics.103

[70] R. A. Johnson, G. K. Bhattacharyya, K.-W. Tsui, and P. I. Good, *Statistics: Principles and Methods, Student Solutions Manual*. John Wiley & Sons, 2001.

[71] C. M. Spencer, S. D. Anderson, D. R. Jensen, and Z. R. Wolf, "A rotating coil apparatus with sub-micrometer magnetic center measurement stability," *IEEE Transactions on Applied Superconductivity*, vol. 16, no. 2, pp. 1334–1337, Jun. 2006.

[72] Z. Wolf, "A vibrating wire system for quadrupole fiducialization," SLAC, Menlo Park, CA, USA, Tech. Rep. LCLS-TN-05-11, May 2005.

[73] S. Anderson, K. Caban, H.-D. Nuhn, E. Reese, and Z. Wolf, "Magnetic measurement results of the LCLS undulator quadrupoles," SLAC, Menlo Park, CA, USA, Tech. Rep. LCLS-TN-09-1, Jan. 2010.

[74] Z. Wolf and Y. Levashov, "Undulator long coil measurement system tests," SLAC, Menlo Park, CA, USA, Tech. Rep. LCLS-TN-07-03, Apr. 2007.

[75] Y. Levashov, V. Kaplunenko, A. Weidemann, and Z. Wolf, "Magnetic measurements, tuning and fiducialization of LCLS undulators at SLAC," in *Proc. 29th International Free Electron Laser Conference 2007 (FEL'07)*, Novosibirsk, Russia, Aug. 2007, pp. 314–317.

[76] J. E. Baader, "Development and commissioning of a flip coil system for measuring field integrals," in *Proc. 39th International Free Electron Laser Conference 2019 (FEL'19)*, Hamburg, Germany, Nov. 2019.

[77] "AUTODESK Fusion 360," https://www.autodesk.com/products/fusion-360/, accessed: 2019-06-03.

[78] "EM Electronics," http://www.emelectronics.co.uk/a22.html.

Appendix A

Permission to Reproduce Copyrighted Material from IEEE

In reference to IEEE copyrighted material which is used with permission in this thesis, the IEEE does not endorse any of University of Campinas's products or services. Internal or personal use of this material is permitted. If interested in reprinting/republishing IEEE copyrighted material for advertising or promotional purposes or for creating new collective works for resale or redistribution, please go to `http://www.ieee.org/publications_standards/publications/rights/rights_link.html` to learn how to obtain a License from RightsLink. If applicable, University Microfilms and/or ProQuest Library, or the Archives of Canada may supply single copies of the dissertation.

Appendix B

Flip Coil System for Measuring Field Integrals

Various methods are available for the measurement of the magnetic field. The choice of a method depends upon many requirements, such as precision, accuracy, speed, geometric constraints, field measurements range, etc. A complete magnetic measurement laboratory would have most of the main available techniques because each method offers distinct advantages and the ability to cross-check the results [28].

The available techniques for characterizing magnetic field at the SLAC Magnetic Measurement Facility (MMF) includes a rotating coil for measuring magnetic center in quadrupoles, a vibrating wire used to fiducialize the quadrupoles, a moving wire for measuring field integrals and Hall probes used to map magnetic fields [71–75].

This appendix describes the development and initial tests of a new flip coil moving wire system for measuring field integrals. The work was carried out at the SLAC MMF for the LCLS-II project. The theory of the technique, the design of the system, the set of tests performed, and the results will be presented and examined[1].

B.1 Field Integrals and Back Projection of the Exit Beam Position

As shown in Section 2.2, the equations that describe the overall effect of an undulator on the electron beam exit angle and position of the electron beam. For simplicity, we will limit

[1]This appendix is an amended version of the following manuscript: J. E. Baader, "Development and commissioning of a flip coil system for measuring field integrals," in *Proc. 39th International Free Electron Laser Conference (FEL'09)*, Hamburg, Germany, Aug. 2019.

the explanation that follows only for the vertical field component B_y. Let α be the horizontal exit angle and d be the horizontal exit position. From (2.26) and (2.28),

$$\alpha = -\frac{e}{\gamma m_e c} I_{1y} \tag{B.1}$$

and

$$d = -\frac{e}{\gamma m_e c} I_{2y}. \tag{B.2}$$

An alternative way to express the exit position is given by the distance ρ between the magnet axis and the back projection of the final beam position to the center of the undulator, as shown in Fig. B.1.

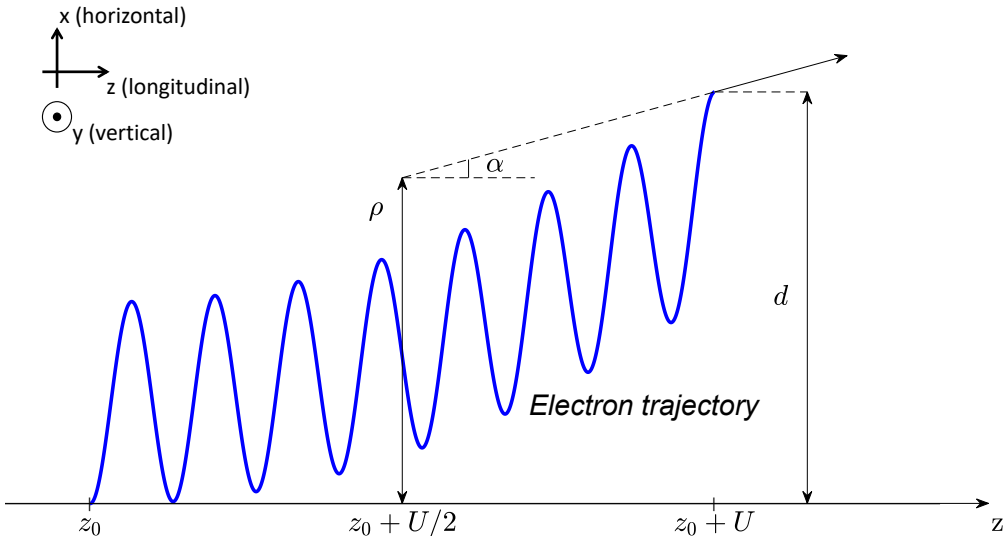

Figure B.1: Electron beam trajectory through an undulator and exit angle, exit position and back projection of the exit position to the center.

Using trigonometric relations and given that $\tan\alpha \approx \alpha$ for small angles,

$$\tan\alpha \approx \alpha = \frac{d-\rho}{U/2}. \tag{B.3}$$

Isolating ρ,

$$\rho = d - \frac{\alpha U}{2}. \tag{B.4}$$

Substituting (B.1) and (B.2) in (B.4),

$$\rho = \frac{e}{\gamma m_e c}\left(\frac{U}{2} I_{1y} - I_{2y}\right). \tag{B.5}$$

Consider now the definition of I_{1y} and I_{2y} obtained in Section 2.2 and rewritten here as (B.6) and (B.7) for convenience.

$$I_{1y} = \int_{-U/2}^{U/2} B_y(z)\,\mathrm{d}z. \tag{B.6}$$

$$I_{2y} = \int_{z_0}^{z_0+U}\int_{z_0}^{z_2} B_y(z_1)\,\mathrm{d}z_1\,\mathrm{d}z_2. \tag{B.7}$$

Let $u = \int_{z_0}^{z_2} B_y(z_1)\,\mathrm{d}z_1$ and $\mathrm{d}v = \mathrm{d}z_2$. Equation (B.7) becomes

$$\int_{z_0}^{z_0+U}\int_{z_0}^{z_2} B_y(z_1)\,\mathrm{d}z_1\,\mathrm{d}z_2 = \int_{z_0}^{z_0+U} u\,\mathrm{d}v = uv\Big|_{z_0}^{z_0+U} - \int_{z_0}^{z_0+U} v\,\mathrm{d}u, \tag{B.8}$$

which is a solution based on integrating by parts. From the definition of u and $\mathrm{d}v$, $\mathrm{d}u = B_y(z_2)\,\mathrm{d}v$ and $v = z_2$. Therefore,

$$\begin{aligned} I_{2y} &= z_2\int_{z_0}^{z_2} B_y(z_1)\,\mathrm{d}z_1\Big|_{z_0}^{z_0+U} - \int_{z_0}^{z_0+U} z_2 B_y(z_2)\,\mathrm{d}z_2 \\ &= (z_0+U)\int_{z_0}^{z_0+U} B_y(z_1)\,\mathrm{d}z_1 - \int_{z_0}^{z_0+U} z_2 B_y(z_2)\,\mathrm{d}z_2 \\ &= (z_0+U)I_{1y} - \int_{z_0}^{z_0+U} z_2 B_y(z_2)\,\mathrm{d}z_2. \end{aligned} \tag{B.9}$$

Replacing (B.9) in (B.5) and joining the similar terms,

$$\rho = \frac{e}{\gamma m_e c}\left[\int_{z_0}^{z_0+U} z_2 B_y(z_2)\,\mathrm{d}z_2 - \left(z_0 + \frac{U}{2}\right) I_{1y}\right]. \tag{B.10}$$

The parameter z_0 is arbitrary in (B.10); the back projection ρ is independent of z_0. This fact may be understood in Fig. B.1. Notice that for the same trajectory profile and length U, ρ would be the same, no matter the value that z_0 takes. Let $z_0 = -U/2$. Then,

$$\rho = \frac{e}{\gamma m_e c}\int_{-U/2}^{U/2} z B_y(z)\,\mathrm{d}z. \tag{B.11}$$

Comparing (B.11) and (B.5), we reach to

$$\int_{-U/2}^{U/2} zB_y(z)\,\mathrm{d}z = \frac{U}{2}I_{1y} - I_{2y}. \tag{B.12}$$

This relationship between field integrals will be meaningful later.

Equations (B.1), (B.2), and (B.5) are useful to analyze the requirement for no net effect on the electron beam position or angle, which is fundamental to ensure the undulators have the minimum possible effect on the electron beam. It is worthy to notice that the vertical field component B_y is used to calculate the horizontal exit angle and position. Similarly, the horizontal field component B_x determines the horizontal first and second field integral I_{1x} and I_{2x}, and are used to calculate the vertical exit angle and position. The next section presents the concepts of the flip coil technique for measuring field integrals.

B.2 Flip Coil Moving Wire Technique

In the flip coil technique, a long coil is rotated within the magnet by 180° during the measurement, and the induced voltage recorded, as illustrated in Fig. B.2.

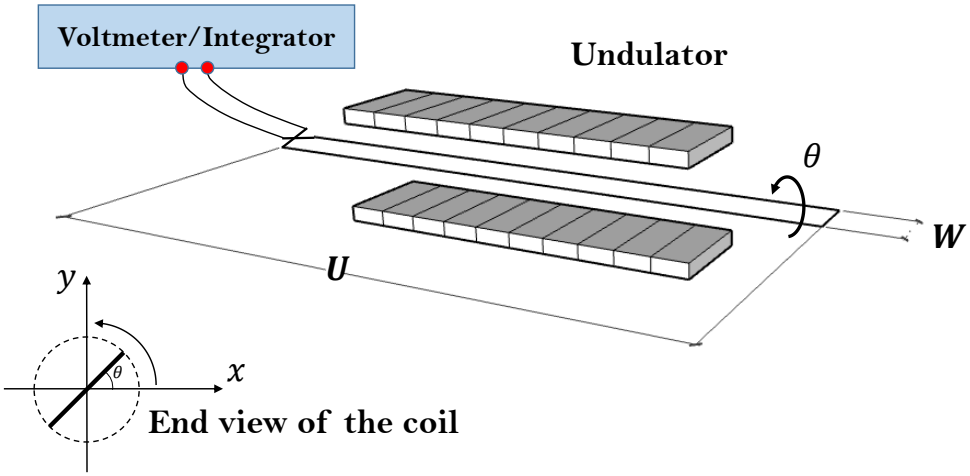

Figure B.2: Simplified sketch of a flip coil system.

The magnetic flux through a surface is defined by $\phi = \int_S \vec{B} \cdot \mathrm{d}\vec{S}$, where $\vec{B}$ is the magnetic field vector and $\mathrm{d}\vec{S}$ is the differential normal area. It is possible to calculate the integrated induced voltage ε in a rotating coil by $\int \varepsilon\,\mathrm{d}t = -N\Delta\phi$, where N is the number of turns of the coil and $\Delta\phi$ is the flux change.

Let ϕ_0 be the magnetic flux at the initial angular position $\theta = \theta_0$. The magnetic flux at the angular position $\theta_0 + \pi$ is $-\phi_0$. Hence, when the coil rotates by 180°,

$$\int \varepsilon \, \mathrm{d}t = -N[\phi_0 - (-\phi_0)] = -2N\phi_0. \tag{B.13}$$

Given the coordinate system and geometry shown in Fig. B.2,

$$\mathrm{d}\vec{S} = \mathrm{d}r \, \mathrm{d}z \, \vec{a}_\phi = \mathrm{d}r \, \mathrm{d}z(-\sin\theta_0 \, \vec{a}_x + \cos\theta_0 \, \vec{a}_y). \tag{B.14}$$

The radial differential $\mathrm{d}r$ can be replaced by $\mathrm{d}x$ when the coil is placed horizontally and by $\mathrm{d}y$ when the coil is placed vertically. Therefore, for these two scenarios,

$$\vec{B} \cdot \mathrm{d}\vec{S} = \begin{cases} B_y \, \mathrm{d}x \, \mathrm{d}z, & \text{if } \theta_0 = 0 \\ -B_x \, \mathrm{d}y \, \mathrm{d}z, & \text{if } \theta_0 = \pi/2, \end{cases} \tag{B.15}$$

where $\vec{B} = B_x \, \vec{a}_x + B_y \, \vec{a}_y + + B_z \, \vec{a}_z$. Notice that B_z is parallel to the wire, which does not change the flux through the wire loop when the wire rotates.

B.2.1 First Field Integral

Vertical First Field Integral (I_{1y})

If the coil rotates from 0° to 180° ($\theta_0 = 0$),

$$\phi_0 = \int_{-U/2}^{U/2} \int_{-W/2}^{W/2} B_y \, \mathrm{d}x \, \mathrm{d}z, \tag{B.16}$$

where U is the coil's length and W is the coil's width. Assuming that B_y does not depend upon x (i.e., B_y is constant over the coil's width) and the coil's length covers the whole magnet's length,

$$\phi_0 = W \int_{-U/2}^{U/2} B_y \, \mathrm{d}z = W I_{1y}. \tag{B.17}$$

Replacing (B.17) in (B.13) and isolating I_{1y},

$$I_{1y} = -\frac{\int \varepsilon \, \mathrm{d}t}{2NW}, \text{ if } \theta_0 = 0. \tag{B.18}$$

Horizontal First Field Integral (I_{1x})

If the coil rotates from 90° to 270° ($\theta_0 = \pi/2$),

$$\phi_0 = \int_{-U/2}^{U/2} \int_{-W/2}^{W/2} -B_x \, \mathrm{d}y \, \mathrm{d}z = -W I_{1x}. \tag{B.19}$$

Replacing (B.19) in (B.13) and isolating I_{1x},

$$I_{1x} = \frac{\int \varepsilon \, \mathrm{d}t}{2NW}, \text{ if } \theta_0 = \pi/2. \tag{B.20}$$

B.2.2 Second Field Integral

By setting the coil's width to zero at the downstream end of the coil, the system will measure the second field integral only, as will be presented in what follows.

The magnetic flux through the geometry shown in Fig. B.3 ($\theta_0 = 0$) is

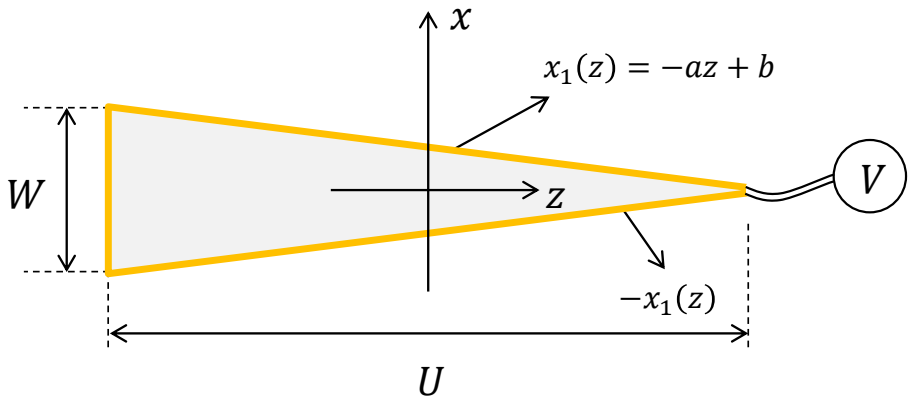

Figure B.3: Coil's geometry for measuring second field integrals [76].

$$\phi_0 = \int_{-U/2}^{U/2} \int_{-x_1(z)}^{x_1(z)} B_y \, \mathrm{d}x \, \mathrm{d}z, \tag{B.21}$$

where $x_1(z) = -az + b$ is the coil's limit upon x-axis, with a and b constant and given by $a = W/(2U)$ and $b = W/4$. Assuming that B_y does not depend upon x and solving (B.21),

$$\begin{aligned}
\phi_0 &= \int_{-U/2}^{U/2}\int_{az-b}^{-az+b} B_y \,\mathrm{d}x\,\mathrm{d}z \\
&= \int_{-U/2}^{U/2} B_y x\Big|_{az-b}^{-az+b} \mathrm{d}z \\
&= \int_{-U/2}^{U/2} 2B_y(-az+b)\,\mathrm{d}z \\
&= -2a\int_{-U/2}^{U/2} zB_y\,\mathrm{d}z + 2b\int_{-U/2}^{U/2} B_y\,\mathrm{d}z \\
&= -\frac{W}{U}\int_{-U/2}^{U/2} zB_y\,\mathrm{d}z + \frac{W}{2}\int_{-U/2}^{U/2} B_y\,\mathrm{d}z.
\end{aligned} \tag{B.22}$$

From (B.6) and (B.12),

$$\phi_0 = -\frac{W}{U}\left[\frac{U}{2}I_{1y} - I_{2y}\right] + \frac{W}{2}I_{1y} = \frac{W}{U}I_{2y}. \tag{B.23}$$

Replacing (B.23) in (B.13) and isolating II_y,

$$I_{2y} = -\frac{U\int \varepsilon\,\mathrm{d}t}{2NW}, \text{ if } \theta_0 = 0. \tag{B.24}$$

Similarly, as presented in the previous section,

$$I_{2x} = \frac{U\int \varepsilon\,\mathrm{d}t}{2NW}, \text{ if } \theta_0 = \pi/2. \tag{B.25}$$

B.3 System Development

B.3.1 Mechanical Design and Motion

The flip coil is mounted in two towers, each composed of two motorized Newport stages model MTMPP.1 with 250 mm of travel range attached at right angles for y (vertical) and x (horizontal) movements. Each tower has one motorized Newport rotation stage model RGV100BL that holds two manual Edmund linear stages with 13 mm of travel for fine adjustments in x-axis and y-axis.The Newport Motion Control XPS-Q8 controls all motorized stages. Each end also has one linear stage that moves towards z-axis and is used to stretch the coil. Figure B.4 shows the system. The mechanical parts of the system (plates, spools,

brackets, etc.) were designed in the Autodesk Fusion 360 [77], as illustrated in Fig. B.5. A zoomed picture of each end of the system (called End A and End B in Fig. B.4) is presented in Fig. B.6.

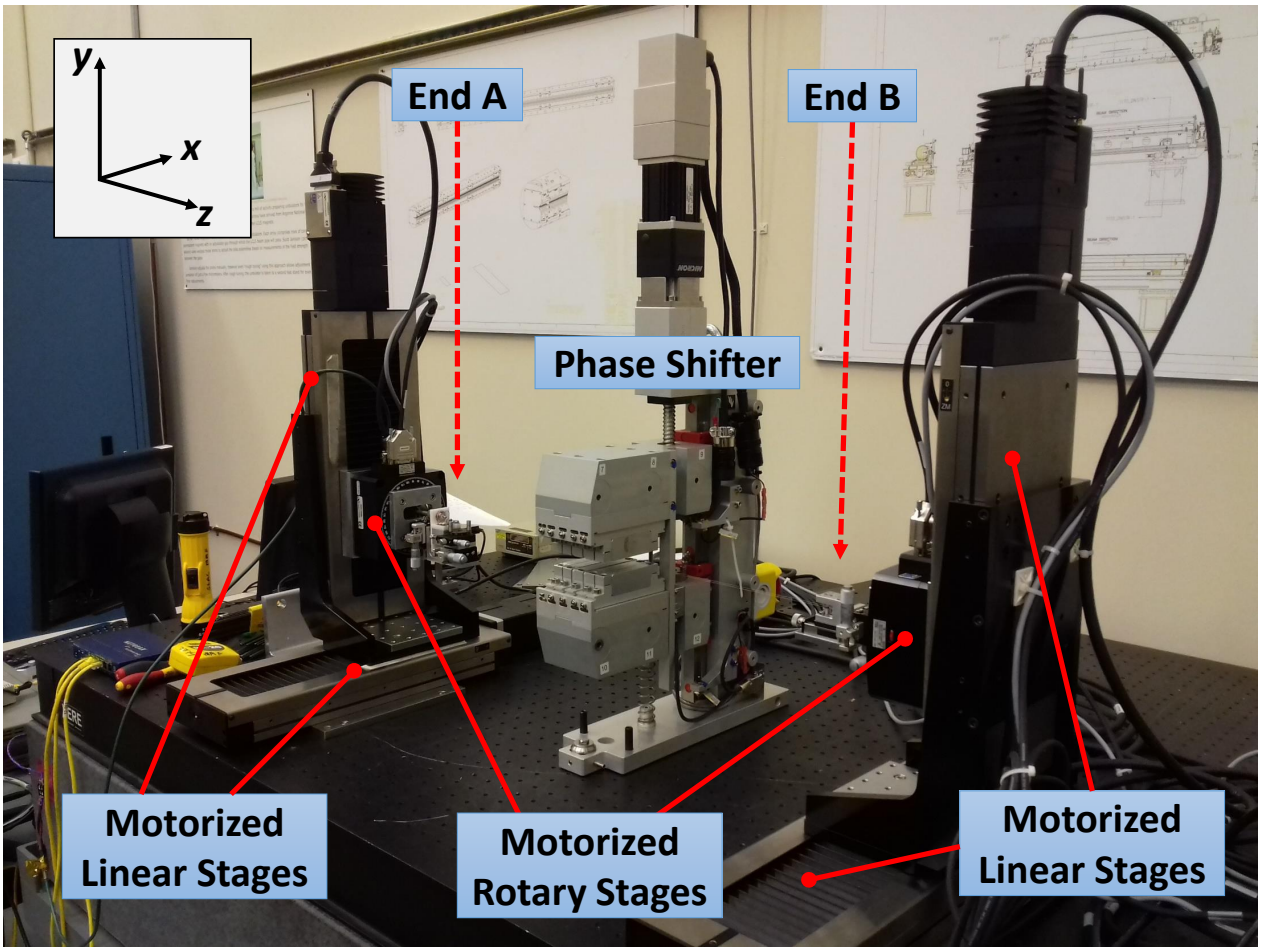

Figure B.4: Flip coil system measuring field integrals of a phase shifter [76].

The coil is a single turn of a 100 µm diameter insulated beryllium copper wire — a high-tensile conducting material — looped between two spools placed on each end, which forms one continuous loop of 5 mm of width (the minimum LCLS-II undulators' gap is 7.2 mm). The coil's length is approximately 60 cm. The End A has one manual Edmund rotary stage with 30 mm of diameter that allows changing the coil's width to measure second field integrals (see details 7 and 8 in Fig. B.6). A low noise amplifier module model EM DC A22 [78] operating as a low-pass filter with a cutoff frequency of 15 Hz is coupled to the wire. The terminals of the amplifier's output are connected to the voltmeter HP 3458 to record the voltage signal induced during the coil's rotation and determine the flux change. The angular

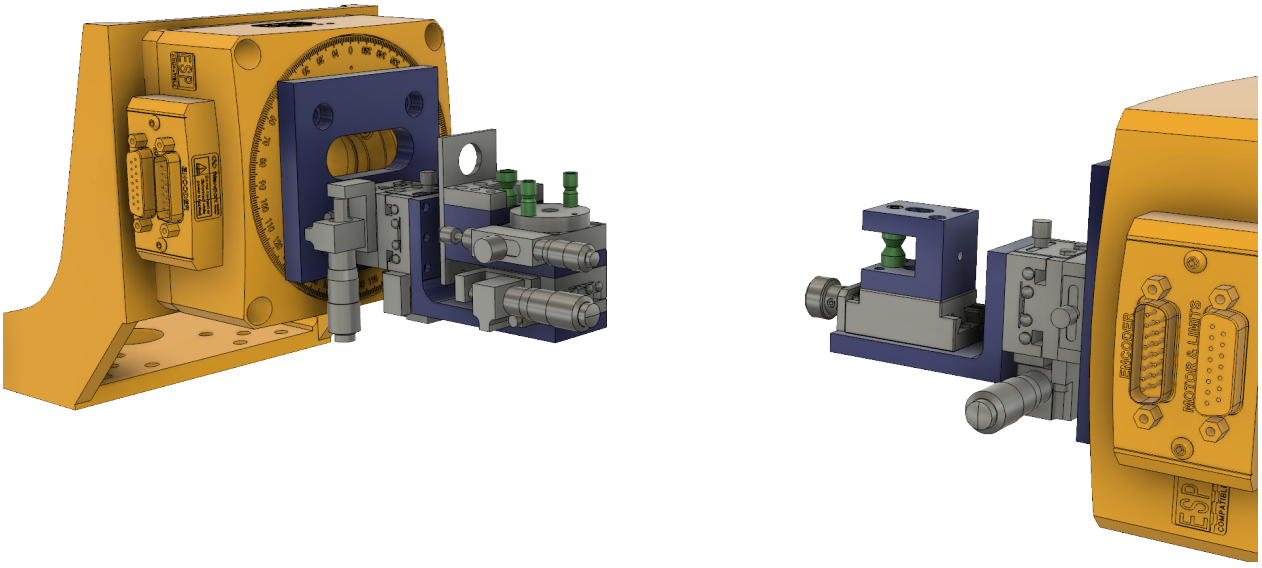

Figure B.5: Workspace in the Autodesk Fusion 360 showing the system's design.

speed and angular acceleration of the coil are 1.5 turns/s and 1.5 turns/s^2, respectively. The coil only performs half revolutions (i.e., an angular variation of 180°), starting either from the horizontal position in 0° (measures vertical field component) or from the vertical position in 90° (measures horizontal field component). Then, the coil reverses its direction to return to the starting position, during which data is also taken.

B.3.2 Software and Measurement Procedure

LabWindows/CVI-based system software was developed to coordinate the motorized stages and data acquisition. A graphical user interface shows the voltage and flux change samples, with the latter being calculated by numerically integrating the voltage samples by the trapezoidal rule, or

$$\Psi_i = \frac{1}{2f_s}(V_i + V_{i-1}) + \Psi_{i-1},\ i = 2, 3, ...n, \tag{B.26}$$

where $\Psi_1 = 0$, f_s is the sampling rate, V_i is the i-th corrected voltage sample, and n is the number of samples for a single flip. The voltage samples taken during the initial and final delay (before and after the angular movement) are used to perform offset corrections by using the technique described in Subsection 3.6.2. Figure B.7 shows an example of the voltage and flux change samples taken during the clockwise and counterclockwise movement for a test

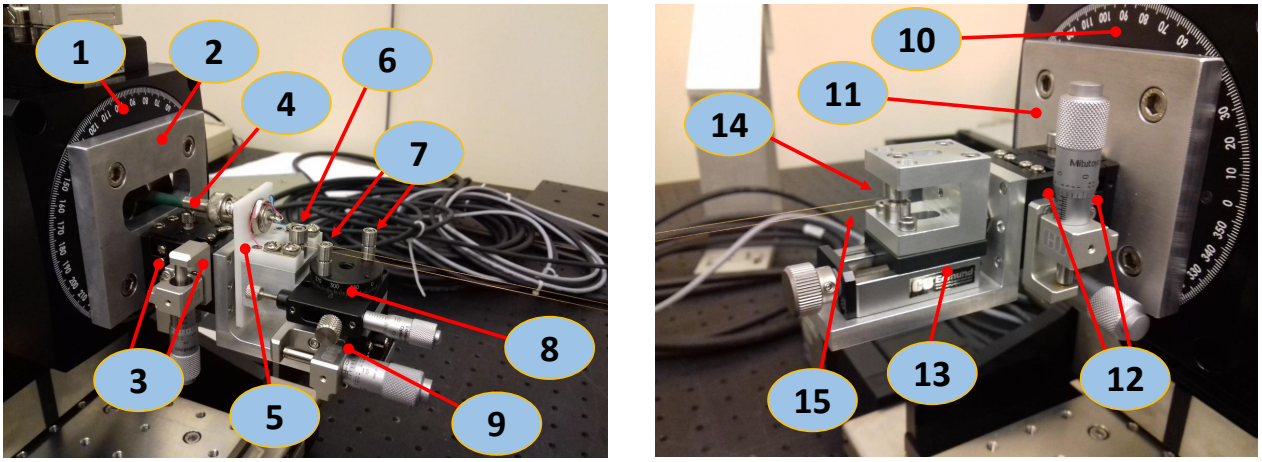

Figure B.6: Zoomed picture of the ends of the flip coil system. At the End A: (1) Motorized rotary stage; (2) Bracket; (3) Manual linear stages used for fine adjustments in the coil's transverse position; (4) BNC cable; (5) Delrin plates; (6) Spool for holding the wire; (7) Spools on the manual rotary stage for changing coil's width; (8) Manual rotary stage; (9) Manual linear stage for stretching the wire. At the End B: (10) Motorized rotary stage; (11) Bracket; (12) Manual linear stages used for fine adjustments in the coil's transverse position; (13) Manual linear stage for stretching the wire. (14) Spool for holding the wire; (15) Insulated beryllium copper wire [76].

with a dipole field.

Once the user selects either vertical or horizontal field measurements, the software defines the starting position of the coil as $\theta_0 = 0°$ or $\theta_0 = 90°$, respectively. An integration period of 3 power line cycles (sampling rate of 20 Hz) is used, which shows good performance since it suppresses 60 Hz noise. The system starts the voltage acquisition, waits 0.5 s, flips the coil from θ_0 to $\theta_0 + 180°$ (clockwise rotation), waits 1 s, and then stops the voltage acquisition. One flip takes approximately 3 s. Given the sampling rate and the delays, 10 samples are read before and 20 samples are read after the movement. The software reads all the voltage samples, applies the offset correction, and calculates the flux change samples using (B.26). The total flux change $-\Delta\phi$ (or $\int \varepsilon \, \mathrm{d}t$) associated with the flip is calculated by averaging the last eight samples of Ψ_i, which increases repeatability. The same procedure is repeated with the coil rotating back to the initial position (counterclockwise rotation). Since the integration is applied for both clockwise and counterclockwise rotations, these integrals have opposite polarity, being subtracted and divided by 2 to determine $\int \varepsilon \, \mathrm{d}t$. For instance, the example shown in Fig. B.7 gives

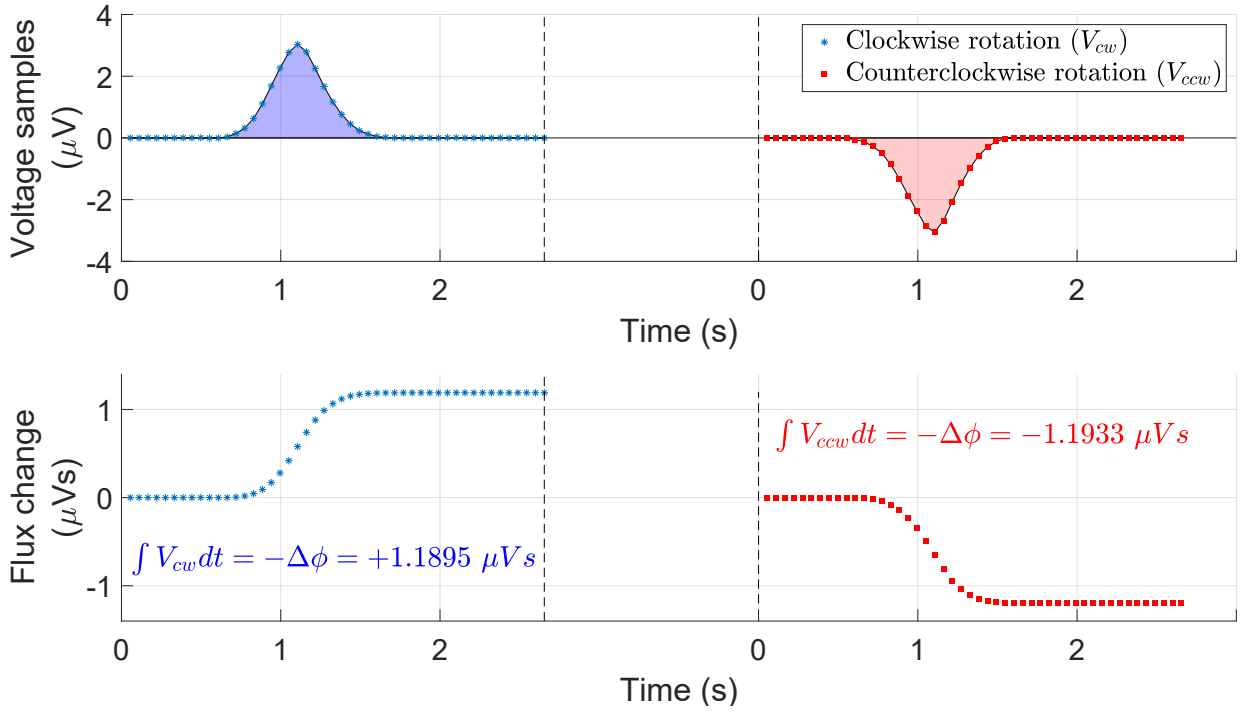

Figure B.7: Example of voltage samples, flux change samples (clockwise and counterclockwise rotations) and value of the total flux change for a measurement of a dipole field [76].

$$\int \varepsilon \, \mathrm{d}t = \frac{1.1895 - (-1.1933)}{2} = 1.1914 \, \mu\mathrm{Vs}. \tag{B.27}$$

In addition, due to the short time separation between each rotation, such a procedure contributes to cancel voltage offsets. After the coil rotates forth and back and $\int \varepsilon \, \mathrm{d}t$ is determined, the software calculates the field integral. A few seconds of delay between the flips are required to ensure the coil is static. To improve the repeatability, a set of 10 samples of $\int \varepsilon \, \mathrm{d}t$ is averaged[2], and the error is expressed as the standard deviation over these samples. The system takes less than three minutes to perform and measure this set of samples.

B.3.3 System Validation

The flip coil system was used to measure the first field integral of a small reference magnet (Fig. B.8) that had its strength estimated as 126 Gcm (Gauss-centimeter[3]) by an independent system. We tested both vertical and horizontal field integral measurements by changing the

[2] 10 samples of $\int \varepsilon \, \mathrm{d}t$ corresponds to 20 flips: 10 repetitions of clockwise and counterclockwise movements.
[3] 1 Gcm = 1 µTm.

reference magnet's field orientation.

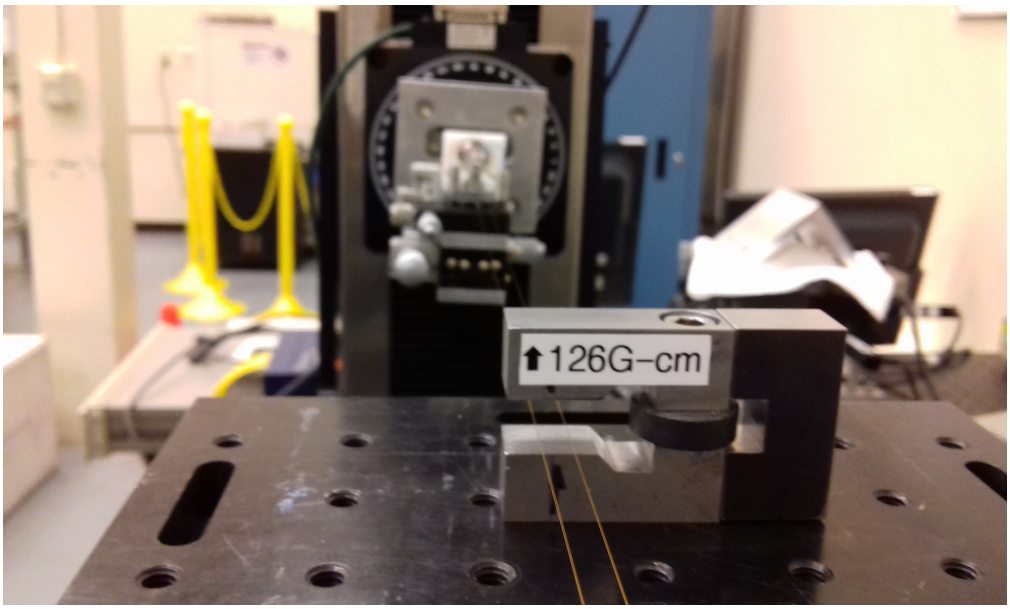

Figure B.8: Reference magnet used to verify the flip coil system.

For simplicity, we will suppress the index "1" to denote the first field integral in what follows. Let I_{yB} and I_{xB} be the first field integral of the background fields on y-axis and x-axis, respectively. Furthermore, let I_{y+} and I_{y-} be the first field integral measured with the flip coil system when a magnet is placed in such a way that its field points to the positive and negative y-axis, respectively. If the magnet's first field integral is I, then $I_{y+} = I + I_{yB}$ and $I_{y-} = -I + I_{yB}$. Therefore, $(I_{y+} - I_{y-})/2$ is, in theory, equal to I, and can be applied to test the system for vertical field integrals measurements. The same is valid for testing horizontal field integrals by setting the reference magnet's field to point to x-axis.

It is interesting to notice that adding I_{y+} to I_{y-} (or I_{x+} and I_{x-}) and dividing by 2, the reference magnet's field is canceled, and only I_{yB} (or I_{xB}) remains. In this case, I_{yB} and I_{xB} can be compared to the background field obtained directly with the flip coil system without any magnets nearby. The next section presents the measurements we performed with the reference magnet and background fields. We tested the system with and without the amplifier module. An additional set of measurements were taken with a phase shifter. Table B.1 summarizes the results of the measurements performed with the reference magnet (lines 1-8), the background fields (lines 9-10), and the phase shifter (lines 11-12).

Table B.1: First field integral measurements with a reference magnet, the background fields and a phase shifter [76].

#	Magnet / condition		Field component	With the low noise amp. EM DC A22	Without the low noise amp. EM DC A22
				Result[1] ± Error[2] (Gcm)	**Result[1] ± Error[2]** (Gcm)
1	Reference magnet's field pointing to	positive y-axis	I_{y+}	+120.75 ± 0.20	+120.90 ± 2.13
2		negative y-axis	I_{y-}	-134.48 ± 0.10[3]	-133.54 ± 0.84[3]
3		positive x-axis	I_{x+}	+142.28 ± 0.13	+140.99 ± 1.67
4		negative x-axis	I_{x-}	-116.73 ± 0.11	-119.09 ± 1.94
5	Reference magnet first field integral		$(I_{y+} - I_{y-})/2$	+127.62 ± 0.11	+127.22 ± 1.15
6			$(I_{x+} - I_{x-})/2$	+129.51 ± 0.08	+130.04 ± 1.28
7	Background first field integral		$(I_{y+} + I_{y-})/2$	-6.87 ± 0.11	-6.32 ± 1.15
8	(estimated from the ref. mag. results)		$(I_{x+} + I_{x-})/2$	+12.77 ± 0.08	+10.95 ± 1.28
9	Backgroud Fields		I_y	-7.36 ± 0.14	-7.03 ± 2.16
10			I_x	+11.37 ± 0.12	+12.09 ± 1.83
11	Phase Shifter		I_y	-10.93 ± 0.15	–
12	(see Fig. B.4)		I_x	+8.88 ± 0.12	–

[1] Calculated by averaging ten measurements.
[2] For $(I_{y+} \pm I_{y-})/2$ and $(I_{x+} \pm I_{x-})/2$ these values were estimated by propagating the error of the terms. For the other components, the errors correspond to the standard deviation over the results of ten measurements.
[3] A very similar result was obtained with the long coil and the fluxgate probe, as shown in the technical report [74].

B.4 Discussion

We designed, built, and commissioned a new flip coil moving wire system for measuring magnetic field integrals. The system is capable of measuring field with a precision of 0.2 Gcm for a 60-cm long coil, and takes less than three minutes to perform a complete measurement.

Coupling the EM DC A22 module to the coil reduced the error (standard deviation of the mean) in one order of magnitude — from 2 Gcm to 0.2 Gcm — which demonstrates the high stability of the results. Besides, the field strength obtained with and without the EM DC A22 module showed no significant difference. These facts support some of the main features expected from the amplifier module, including high gain stability and low drifts.

Comparing the reference value of 126 Gcm obtained by independent measurements and the values calculated in lines 5-6 shows that the measurements performed with the flip coil system agreed at the level of 3%. We believe that the error of the coil's width determination and small displacements of the reference magnet are the primary sources of errors that justify the slight disparity. Further studies are necessary to define the optimal coil's width.

We may assume that the most significant influence in the background fields comes from the Earth's magnetic field, which is supposed to induce a very weak signal to the coil. Even so, the background field measurements exhibited the same order of error observed for the other measurements, as shown in lines 9-10. It is essential to notice that lines 7-8 present an

estimate for background field based on the measurements with the reference magnet — considerable field strength in comparison with the Earth's field strength. The agreement among the results presented in lines 7-8 and 9-10 at the level of 1 Gcm confirms that the system detects small field integrals.

A mechanical adaptation was made as an attempt to measure second field integrals by changing the coil's width at one of the ends. The precision of 0.2 Gcm for the first field integrals suggests that the precision of second field integrals measurements would be about $0.1\,\mu Tm^2$ for a 60-cm long coil. Still, further tests have to be taken to evaluate the system performance for determining second field integrals. Although the coil's length is suitable for measuring small magnets (e.g., dipoles, quadrupoles, phase shifters, etc.), tests with a longer coil need to be performed with LCLS-II undulators in the future.

Appendix C

Slippage Equation

An electron travels in an undulator at speed v_z in the z-axis, while the emitted radiation travels at the speed of light c. Since v_z is slightly smaller than c, the radiation wavefront moves faster than the electron. Let S be the difference between the wavefront and the electron position — known as *slippage*. This appendix aims to deduce the slippage equations used in Section 2.4.

After $\mathrm{d}t$, the slippage changes by

$$\mathrm{d}S = (c - v_z)\,\mathrm{d}t. \tag{C.1}$$

Let z be a point on the radiation wave. In this case, $c = \mathrm{d}z/\mathrm{d}t$. Isolating $\mathrm{d}t$ and substituting in (C.1),

$$\mathrm{d}S = \left(1 - \frac{v_z}{c}\right)\,\mathrm{d}z. \tag{C.2}$$

Assuming that the electron trajectory occurs only in the xz plane, $v_y = 0$. Let $\beta = v/c$ be the electron velocity relative to the speed of light, where $v^2 = v_x^2 + v_z^2$. We also define the relative transverse and longitudinal velocity $\beta_x = v_x/c$ and $\beta_z = v_z/c$, respectively, which leads to $\beta_z^2 = \beta^2 - \beta_x^2$. Replacing in (C.2),

$$\mathrm{d}S = (1 - \sqrt{\beta^2 - \beta_x^2})\,\mathrm{d}z. \tag{C.3}$$

From the definition of β_x,

$$\beta_x = \frac{v_x}{c} = \frac{\mathrm{d}x}{\mathrm{d}t} \cdot \frac{\mathrm{d}t}{\mathrm{d}z} = \frac{\mathrm{d}x}{\mathrm{d}z} = \dot{x}(z). \tag{C.4}$$

Substituting (C.4) in (C.3),

$$\mathrm{d}S = \left(1 - \sqrt{\beta^2 - \dot{x}^2}\right) \mathrm{d}z. \tag{C.5}$$

Expanding the term $\sqrt{\beta^2 - \dot{x}^2}$ in Taylor series and keeping only first order terms for small values,

$$\sqrt{\beta^2 - \dot{x}^2} = \beta^2 - \frac{1}{2}\dot{x}^2. \tag{C.6}$$

Based on the definition of the Lorentz factor γ [see (2.3)],

$$\gamma = \frac{1}{\sqrt{1 - \beta^2}}. \tag{C.7}$$

Isolating β^2,

$$\beta^2 = 1 - \frac{1}{2\gamma^2}. \tag{C.8}$$

Thus, (C.6) becomes

$$\sqrt{\beta^2 - \dot{x}^2} = \beta^2 - \frac{1}{2}\dot{x}^2 = 1 - \frac{1}{2\gamma^2} - \frac{1}{2}\dot{x}^2. \tag{C.9}$$

Replacing (C.9) in (C.5),

$$\mathrm{d}S = \left(\frac{1}{2\gamma^2} + \frac{\dot{x}^2}{2}\right) \mathrm{d}z. \tag{C.10}$$

Integrating from z_0 to z with $\dot{x}(z_0) = 0$,

$$S(z) = \int_{z_0}^{z} \left(\frac{1}{2\gamma^2} + \frac{\dot{x}^2}{2}\right) \mathrm{d}z. \tag{C.11}$$

Now, consider a pure sinusoidal field with undulator parameter K. From (2.32) and the K definition,

$$\dot{x}(z) = \frac{K}{\gamma} \sin\left(\frac{2\pi z}{\lambda_u}\right). \tag{C.12}$$

where $\dot{x}(z_0) = 0$. Substituting (C.12) in (C.11),

$$S(z) = \int_{z_0}^{z} \left[\frac{1}{2\gamma^2} + \frac{K^2}{2\gamma^2} \sin^2\left(\frac{2\pi z}{\lambda_u}\right) \right] \mathrm{d}z. \tag{C.13}$$

Using the trigonometric identity

$$\sin^2\theta = \frac{1}{2} - \frac{\cos(2\theta)}{2}, \tag{C.14}$$

we reach to

$$\begin{aligned} S(z) &= \int_{z_0}^{z} \left\{ \frac{1}{2\gamma^2} + \frac{K^2}{2\gamma^2} \left[\frac{1}{2} - \frac{1}{2}\cos\left(\frac{4\pi z}{\lambda_u}\right) \right] \right\} \mathrm{d}z \\ &= \int_{z_0}^{z} \left[\frac{1}{2\gamma^2} + \frac{K^2}{4\gamma^2} - \frac{K^2}{4\gamma^2}\cos\left(\frac{4\pi z}{\lambda_u}\right) \right] \mathrm{d}z \\ &= \int_{z_0}^{z} \left[\frac{1}{2\gamma^2}\left(1 + \frac{K^2}{2}\right) - \frac{K^2}{4\gamma^2}\cos\left(\frac{4\pi z}{\lambda_u}\right) \right] \mathrm{d}z \\ &= \frac{1}{2\gamma^2}\left(1 + \frac{K^2}{2}\right)(z - z_0) - \frac{K^2}{4\gamma^2}\frac{\lambda_u}{4\pi}\left[\sin\left(\frac{4\pi z}{\lambda_u}\right) - \sin\left(\frac{4\pi z_0}{\lambda_u}\right) \right] \\ &= \frac{1}{2\gamma^2}\left(1 + \frac{K^2}{2}\right)(z - z_0) - \frac{\lambda_u K^2}{16\pi\gamma^2}\left[\sin\left(\frac{4\pi z}{\lambda_u}\right) - \sin\left(\frac{4\pi z_0}{\lambda_u}\right) \right]. \end{aligned} \tag{C.15}$$

Let S_p be the slippage between the points z_0 and z in the z-axis that are a whole number of λ_u apart from each other (i.e., $z = z_0 + n\lambda_u$). Under this condition, the second term of (C.15) is zero. Therefore,

$$S_p = \frac{1}{2\gamma^2}\left(1 + \frac{K^2}{2}\right)\Delta z_p, \tag{C.16}$$

where $\Delta z_p = z - z_0$.

Appendix D

Laplace's Equation Solution

The conditions $\nabla \cdot \vec{B}$ and $\nabla \times \vec{B} = 0$ leads to the well-known Laplace's Equation $\nabla^2 \Phi = 0$, where Φ is scalar potential and $\vec{B} = -\nabla \Phi$. Applying the separation of variables method,

$$\Phi = f(x)g(y)h(z). \tag{D.1}$$

For a rectangular coordination system, Laplace's equation becomes

$$\nabla^2 \Phi = \frac{\partial^2 \Phi}{dx^2} + \frac{\partial^2 \Phi}{dy^2} + \frac{\partial^2 \Phi}{dz^2} = gh\frac{\partial^2 f}{dx^2} + fh\frac{\partial^2 g}{dy^2} + fg\frac{\partial^2 h}{dz^2} = 0. \tag{D.2}$$

Diving (D.2) by fgh,

$$\frac{1}{f}\frac{\partial^2 f}{dx^2} + \frac{1}{g}\frac{\partial^2 g}{dy^2} + \frac{1}{h}\frac{\partial^2 h}{dz^2} = 0. \tag{D.3}$$

All the terms present in the sum are independent; hence, each one must be a constant, and the sum of these constants is zero. For convenience, we express

$$\frac{1}{f}\frac{\partial^2 f}{dx^2} = k_x^2 \tag{D.4}$$

$$\frac{1}{g}\frac{\partial^2 g}{dy^2} = k_y^2 \tag{D.5}$$

$$\frac{1}{h}\frac{\partial^2 h}{dz^2} = k_z^2 \tag{D.6}$$

$$k_x^2 + k_y^2 + k_z^2 = 0. \tag{D.7}$$

Regarding undulators, we are interested in all solutions that are periodic in z, which makes k_z a purely imaginary number. Consider the solution

$$h(z) = A_5(n)\cos(nk_u z) + A_6(n)\sin(nk_u z), \quad n \in \mathbb{N}^*, \tag{D.8}$$

where A_5 and A_6 are real constants. Replacing (D.8) in (D.6), $k_z = ink_u$, where $i = \sqrt{-1}$. For our analyzes, the first harmonic $n = 1$ is sufficient. Thus, we define the solution of $h(z)$ as

$$h(z) = A_5\cos(k_u z) + A_6\sin(k_u z). \tag{D.9}$$

The x- and y-dependent terms $f(x)$ and $g(y)$ do not have periodicity requirement, so

$$f(x) = A_1(k_x)\cosh(k_x x) + A_2(k_x)\sinh(k_x x) \tag{D.10}$$

and

$$g(y) = A_3(k_y)\cosh(k_y y) + A_4(k_y)\sinh(k_y y). \tag{D.11}$$

where A_1, A_2, A_3 and A_4 are real constants. Substituting (D.9), (D.10) and (D.11) in (D.1),

$$\begin{aligned}\Phi =&[A_1\cosh(k_x x) + A_2\sinh(k_x x)] \times [A_3\cosh(k_y y) + A_4\sinh(k_y y)]\times \\ &[A_5\cos(k_u z) + A_6\sin(k_u z)].\end{aligned} \tag{D.12}$$

Since $k_z = ik_u$, (D.7) becomes

$$k_x^2 + k_y^2 = k_u^2. \tag{D.13}$$

Even though simple, Fig. 2.1 represents the structure of a planar undulator properly enough, being suitable to define the boundary conditions. In relation to the plane yz ($x = 0$), the device is symmetric, which helps see the existence of a left-right symmetry for the magnetic field along the x-axis. As a result, $A_2 = 0$. The field in y points always towards the

same orientation for a fixed x and z values (i.e., the vertical component keeps the same signal independently of y for a given x and z). Since $B_y = -d\Phi/dy$, $A_3 = 0$. At $z = 0$, the field is maximum, so $A_6 = 0$. With those conditions, (D.12) is simplified to

$$\Phi = \Phi_0 \cosh(k_x x) \sinh(k_y y) \cos(k_u z), \tag{D.14}$$

where $\Phi_0 = A_1 A_4 A_5$. The vertical field component towards the z-axis (where x and y are zero) is given by

$$B_y(z) = -\frac{\mathrm{d}\Phi}{\mathrm{d}y}\bigg|_{x=0,y=0} = -k_y \Phi_0 \cos(k_u z). \tag{D.15}$$

Comparing with (2.30), rewritten here for convenience as $B_y(z) = \hat{B}\ cos(k_u z)$,

$$\Phi_0 = -\hat{B}/k_y. \tag{D.16}$$

Therefore,

$$\Phi = -\frac{\hat{B}}{k_y} \cosh(k_x x) \sinh(k_y y) \cos(k_u z). \tag{D.17}$$

Appendix E

List of Publications

- J. E. Baader, S. D. Anderson, and Z. R. Wolf, "A novel in-situ radiation damage diagnostic system for undulators," *IEEE Transactions on Instrumentation and Measurement*, in press, doi: 10.1109/TIM.2019.2936715.
- J. E. Baader, S. D. Anderson, and Z. R. Wolf, "High-precision reference pulse generator for testing radiation damage in undulators," *IEEE Transactions on Instrumentation and Measurement*, under review.
- J. E. Baader, "Development and commissioning of a flip coil system for measuring field integrals," in *Proc. 39th International Free Electron Laser Conference (FEL'09)*, Hamburg, Germany, Aug. 2019.
- C. M. S. Lobo, G. Tosin, J. E. Baader, L. A. Colnago, "Complementary analyses of hollow cylindrical unioriented permanent magnet (HCM) with high permeability external layer," *Journal of Magnetic Resonance*, vol. 283, pp. 79-88, Oct. 2017, doi: 10.1016/j.jmr.2017.08.013.